Optics and Magnetism:
From Itinerant
to
Localized Electrons

Fausto Patricio Mena

ISBN 90-367-2128-8

The work presented in this thesis was performed at the Optical Solid State Physics Laboratory of the University of Groningen. The project was supported by the Dutch Foundation for Fundamental Research on Matter (FOM) with financial support from the Dutch Organization for the Advancement of Pure Research (NWO).

Front cover: Color map surface showing the difference $\sigma_1(\omega, T) - \sigma_1(\omega, 280K)$ obtained from $(La_{0.5}Pr_{0.5})_{0.7}Ca_{0.3}Mn^{16}O_3$ thin films.
Back cover: Gold funerary mask from *La Tolita* culture (Ecuador, 500 BC - 200 AD).

Author email: `patricio_mena@hotmail.com`

Rijksuniversiteit Groningen

Optics and Magnetism: From Itinerant to Localized Electrons

PROEFSCHRIFT

ter verkrijging van het doctoraat in de
Wiskunde en Natuurwetenschappen
aan de Rijksuniversiteit Groningen
op gezag van de
Rector Magnificus, dr. F. Zwarts,
in het openbaar te verdedigen op
vrijdag 17 september 2004
om 13.15 uur

door

Fausto Patricio Mena

geboren op 5 juni 1970
te Quito, Ecuador

Promotores: Prof. Dr. D. van der Marel
Prof. Dr. Ir. P. H. M. van Loosdrecht

Beoordelingscommissie: Prof. Dr. M. Dressel
Prof. Dr. D. Khomskii
Prof. Dr. M. Sigrist

Contents

Chapter 1

Introduction

Optical spectroscopy is one of the oldest techniques used to determine the properties of materials [1]. Nowadays it is used in an ample variety of fields (e.g. biology, physics, chemistry, astrophysics, materials science, paint restoration, forensics) and materials (e.g. polymers, ferromagnets, organics) in different forms (e.g. solids, liquids, gases). In the work presented in this thesis, optical spectroscopy has been used in different materials of current interest in solid state physics. This introductory chapter describes why optical spectroscopy is important and what can be learnt from it. Furthermore, a brief review of the materials studied in this thesis will be presented. Finally the scope of the present work will be outlined.

1.1 Optical Spectroscopy: Why?

In a dictionary-like definition, it can be said that optical spectroscopy is the use of light to investigate the properties of a material. For the purposes of this work, it has been used to determine the optical conductivity, $\sigma(\omega)$, of the material under study and from there investigate its electronic structure or electronic properties. The question is then, why is optical spectroscopy a good tool to such investigation? To answer this question, I would like to follow A. J. Millis [2] and A. Chattopadhyay et al. [3] who have stated the answer in a simple way. In the first place let us consider the (complex) optical conductivity which simply describes the response of a material to an electric field (for more details see Chapter 2):

$$\boldsymbol{J}(\omega) = \sigma(\omega)\boldsymbol{E}(\omega) \tag{1.1}$$

In other words, the optical conductivity describes how the electrons move in response to an electrical field and, therefore, it can give information about the mechanism associated with this motion. In strongly correlated systems, at low frequencies, the dominant process is the motion from one site to other. This

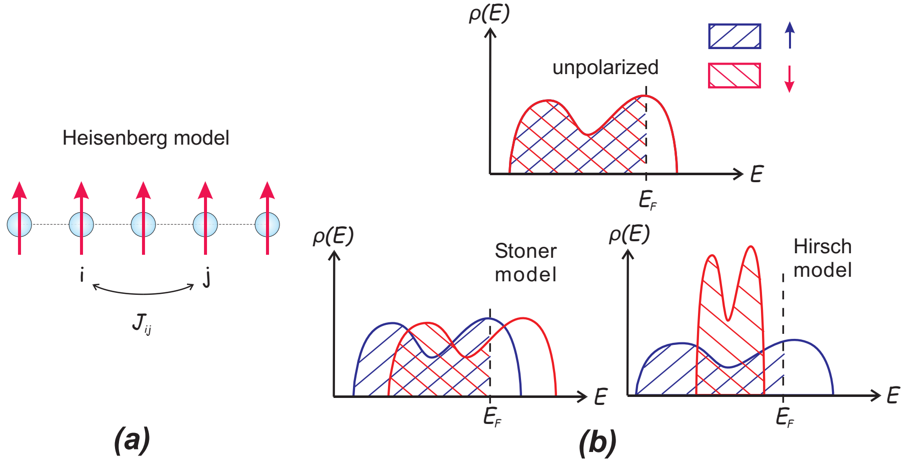

Figure 1.1: *(a) Localized moments: Heisenberg model. (b) Itinerant magnetism: Stoner and Hirsch models (adapted from References [4] and [5]).*

motion is the result of the interplay between repulsive electron-electron interactions (localizing effect) and wave function hybridization (delocalizing effect). This interplay is the essence of strong correlations.

1.2 Magnetism and Strong Correlations

1.2.1 Localized vs. Itinerant Magnetism

The ultimate origin of magnetism in solids is the magnetic moment of their individual atoms (and which originates from the spin and angular momenta of the electron). However, the main question is how this *microscopic* magnetism gives rise to the *macroscopic* magnetism of solids appearing in some materials below a transition temperature, called Curie temperature, T_C. There are two main and opposite streams: localized and itinerant models. The former models start with the electronic states localized in real space, while the latter start with those states localized in reciprocal space [4]. Both situations are schematically represented in Fig. 1.1.

The idea of localized moments is the most intuitive one. It was introduced by Weiss, he argued that the individual magnetic moments interact between them and therefore can align. He represented this interaction by a mean molecular field. Heisenberg attributed this field to the quantum mechanical exchange interaction between neighboring atoms. If $\boldsymbol{S}_i$ is the atomic spin operator at a given site, the

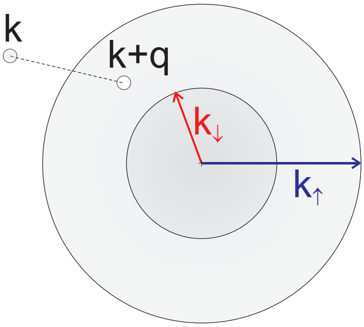

Figure 1.2: *Thermal excitation in a itinerant polarized system (after Ref. [4]). It consists of a spin flip excitation of an electron across the Fermi level. This excitations produce a spin density density fluctuation.*

Heisenberg model for magnetism is:

$$H = \sum_{i,j} J_{ij} \boldsymbol{S}_i \cdot \boldsymbol{S}_j \tag{1.2}$$

where J_{ij} is the interatomic exchange interaction constant. Within this model, the Curie-Weiss law (i.e. $\chi^{-1} \propto T - T_C$, where χ is the magnetic susceptibility) is naturally explained. Moreover, materials considered as having localized moments are expected to have a saturation magnetization, μ_S, which is an integer multiple of the Bohr magneton, μ_B.

On the other hand, magnetism in metals is usually explained from an itinerant picture. One of the main reasons to invoke a different mechanism is that the saturation magnetization, μ_S, is not an integer multiple of μ_B*. In the Stoner model, magnetism in metals arise from a splitting between the up- and down-spin bands and it is favored when the density of states is high at the Fermi level. However, in this form, the Stoner model fails to reproduce the measured T_C and the observed Curie-Weiss law above it. Improvements to this theory have been made that take into account the effect of spin fluctuations (see Fig. 1.2) in a self consistent renormalized (SCR) manner [4]. It is claimed [4] that one of the achievements of SCR theory is the description of several properties of weak itinerant ferromagnets. Several features define this kind of ferromagnets:

a. Low Curie temperature. Usually, less than 50 K.

b. They follow a Curie-Weiss law quite precisely in the temperature interval $T_C < T < 10\,T_C$.

---

*Other mechanisms involving localized moments can also predict non integer values of μ_S. For example the combination of of spin-orbit interaction and crystal field. Other example is given in Ref. [6] where a Kondo-like mechanism is described and which is responsible for the screening of part of the magnetic moment.

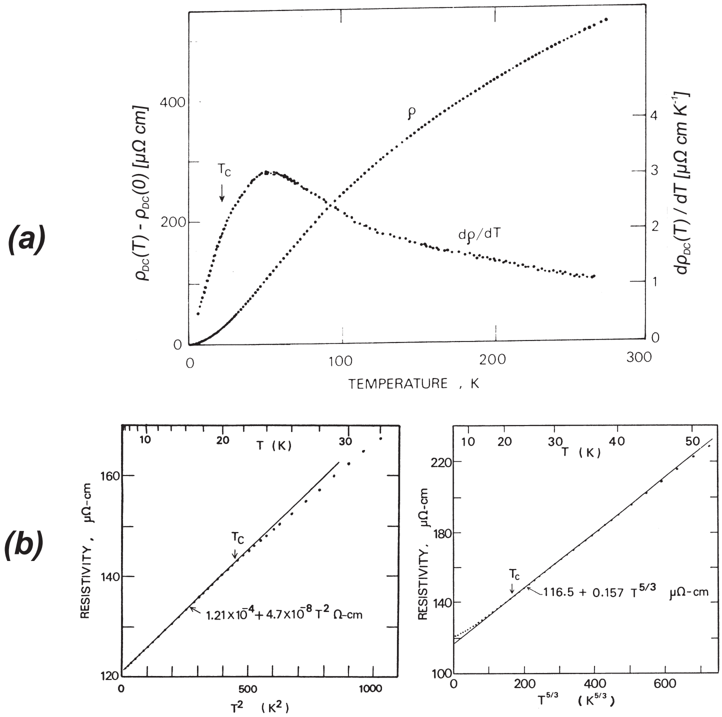

Figure 1.3: *Temperature dependence of ρ_{DC} in $ZrZn_2$. (a) Data from Ref. [8] (b) Analysis by Moriya [4] showing the expected temperature dependencies for spin fluctuations below and above T_C, respectively.*

c. The magnetization inferred from the Curie-Weiss law is several times the saturation magnetization.

It usually appears in materials whose components are not magnetic in elemental form like $ZrZn_2$ and $ScIn_3$. One of the materials studied in this thesis, MnSi, is considered to be well described by the SCR theory. It indeed describes several of its properties like the negative magnetoresistance and the temperature behaviour of the DC resistivity, ρ_{DC}, below T_C (see Fig. 1.3 for the predictions of the SCR theory regarding ρ_{DC}). However, as it will be seen in Chapter 3, the description is not complete. Moreover, other silicides showing itinerant ferromagnetism (Chapter 4) do not follow completely its predictions, namely they show a positive magnetoresistance [7].

More recently, another mechanism for magnetism in itinerant systems has been proposed [5]. This process is sketched in Fig. 1.1. It has been found that magnetism can arise without exchange splitting but with a change in the width of the bands upon spin polarization (although both effects can be combined). The

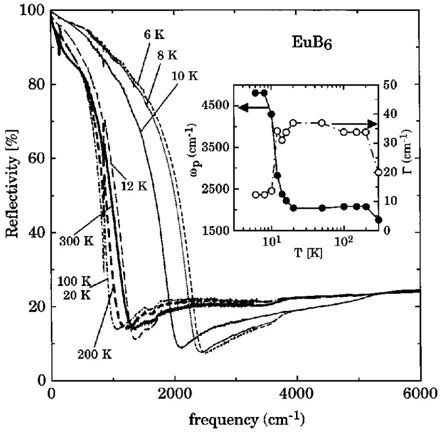

Figure 1.4: *Reflectivity of EuB$_6$ at several temperatures. The inset shows the temperature dependence of the plasma frequency and width of the Drude peak (from Ref. [11]).*

difference is that ferromagnetism from exchange splitting arises from a gain in potential energy, while in this new model it arises from gain in kinetic energy [5]. This implies that this effect can be seen in optics (see § 1.3). The reduction in kinetic energy produces a transfer of the spectral weight contained in the optical conductivity from high to low frequencies as the system enters to the magnetic state (and vice versa above T_C). Hirsch has argued that this effect could be the driving mechanism in all the different manifestations of metallic ferromagnetism [9]. In fact, optical experiments in manganites (see Chapter 6), manganese doped GaAs [10], and rare earth hexaborides [11] seem to corroborate this point of view. As an example, the optical properties of EuB$_6$ [11] are shown in Fig. 1.4 where the increase of the spectral weight at low frequencies is manifested by the increase of the plasma frequency of the Drude peak. In contraposition to this trend, it will be seen in Chapters 3 and 4 that the spectral weight at low frequencies decreases when entering the magnetic ordered state in various transition metal silicides.

1.2.2 Heavy Fermion Systems

There are systems where we can find both *kind* of electrons. On one side, there are electrons which are localized and are responsible for the magnetic properties. On the other side, electrons which are delocalized and are responsible for the transport properties. If they interact it gives rise to a multitude of interesting phenomena. One of such systems are the so-called heavy fermion systems. Heavy fermion systems are compounds which usually have an atom (e.g. Ce or U) containing well localized 4*f* or 5*f* electrons.[†] Below a characteristic temperature T^* heavy

---

[†] Recently some compounds have appeared which only contain *d* electrons (e.g. LiV$_2$O$_4$ [12]) that have similar properties as the heavy fermion compounds. Whether they are also governed

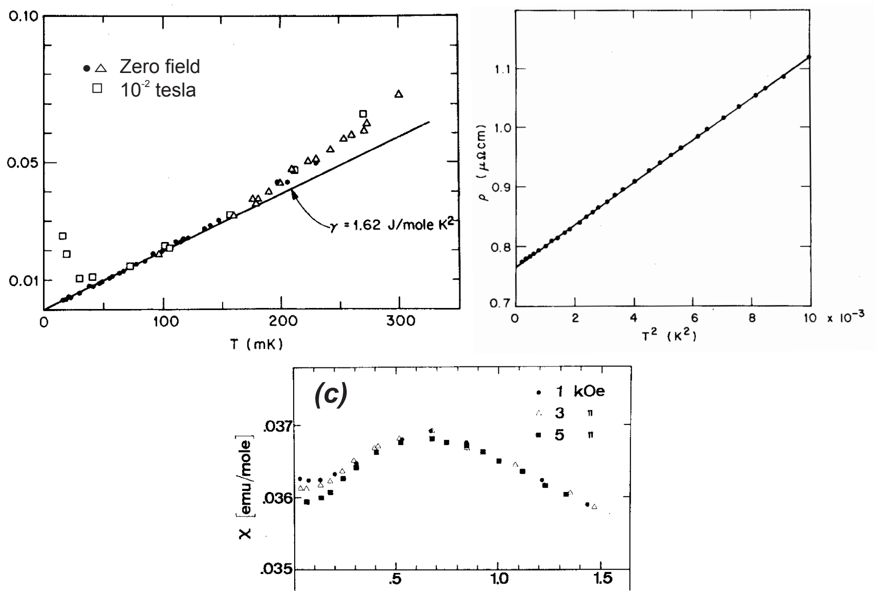

Figure 1.5: *(a) Specific heat, (b) resistivity, and magnetic susceptibility in the first heavy fermion metal discovered, CeAl₃ [15].*

fermion systems show a Fermi-liquid behaviour with large effective masses, m^*, of the quasiparticles. In fact, the physical quantities describing the system have the same temperature dependencies as the normal metals but with much larger proportional constants and at lower temperatures. [13, 14]

Three conditions are usually taken as defining a heavy fermion system at low temperatures[‡]:

a. The specific heat is linear with temperature, $C = \gamma T$;

b. The magnetic susceptibility, χ, is constant (Pauli like);

c. The Wilson's ratio, $R_W = \frac{\pi^2 k_B^2 \chi}{3\mu_{eff}^2 \gamma}$, is of order unity ($\mu_{eff}$ is the effective moment of the quasiparticles).

Since γ and χ are proportional to $N(0)$ which, in turn, is proportional to the effective mass of the fermionic excitations, m^*, their large values can be interpreted

---

by the same physical process is an ongoing debate.

[‡] Remember that for a Fermi gas the specific heat and the susceptibility at low temperatures are given, respectively, by [16]: $C = \frac{1}{3}\pi^2 N(0) k_B^2 T$, and $\chi = N(0)\mu^2$, where $N(0)$ is the density of states at the Fermi level and μ is the magnetic moment of the electron

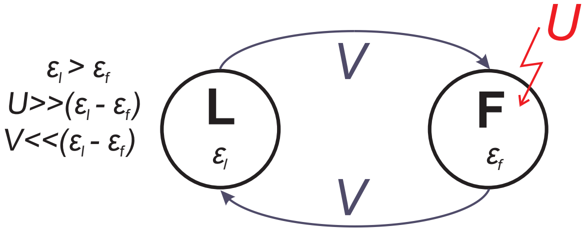

Figure 1.6: *Simplest example of a strongly correlated system (after Ref. [13]). The system contains two orbitals denoted L and F with energies ε_L and ε_F, respectively. Between them, there is an hybridization V. Putting two electrons in the orbital F costs an energy U. Electron interactions in the orbital L and between the two orbitals are neglected.*

as an enhancement of the mass of the quasiparticles. If conditions a.-c. are met, it is possible to say that there is a one-to-one correspondence between the quasiparticle excitations in this system and those in a Fermi gas. Other quantities behave also as in normal metals, e.g. the DC resistivity which is proportional to T^2. As an example consider Fig. 1.5 where C, χ and ρ_{DC} of CeAl$_3$ are plotted [15]. If $R \neq 1$ the interaction between quasiparticles is also important. When $T > T^*$, the excitations lose their heavy fermion character: the specific heat levels off and the susceptibility changes from Pauli- to Curie-like. In the remainder of this subsection, the mechanism originating this behaviour is sketched.

A Strongly Correlated Molecule

Following Fulde [13], let us first consider the system depicted in Fig. 1.6 which contains the main ingredients necessary to understand the heavy fermion systems. The Hamiltonian describing it is:

$$H = \varepsilon_l \sum_\sigma l_\sigma^\dagger l_\sigma + \varepsilon_f \sum_\sigma f_\sigma^\dagger f_\sigma + V \sum_\sigma \left(l_\sigma^\dagger f_\sigma + f_\sigma^\dagger l_\sigma \right) + U n_\uparrow^f n_\downarrow^f \tag{1.3}$$

each term describes, respectively, kinetic energy in orbital L, kinetic energy in orbital F, hybridization between the two orbitals, and electron interaction in orbital F. For $V = 0$ and $V \neq 0$ the accessible states and their are sketched in Fig. 1.7. In the former case, the ground state is 4-fold degenerate (one electron in L and the other in F, therefore forming a singlet and a triplet states) and there is one excited level[§] (two electrons in L). If the hybridization is turned on, the degeneracy of the ground state is partially lifted since now the singlet and the excited states are coupled. The singlet lowers its energy by $2V^2/\Delta\varepsilon$ while the excited state increases its energy by the same amount. The occupancy of F, in this case, is $n_f = 1 - 2(V^2/\Delta\varepsilon)^2 < 1$.

[§] There is another excited state (2 electrons in F) not considered due to the large value of U

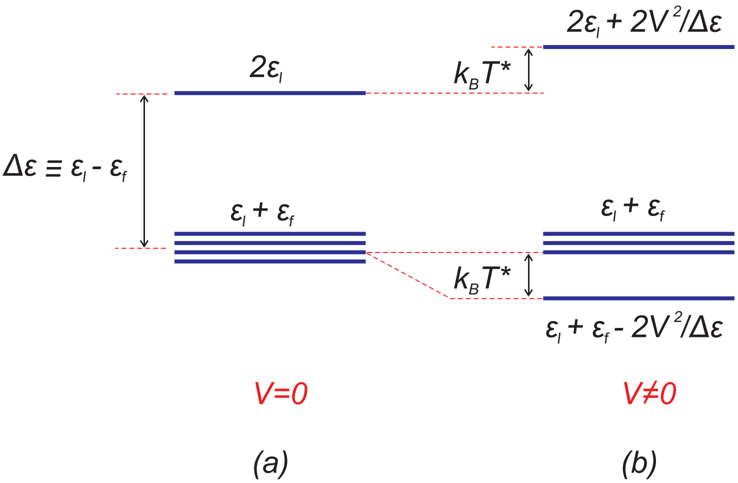

Figure 1.7: *Accessible states and energies in the system considered in Fig. 1.6 for (a)* $V = 0$ *and (b)* $V \neq 0$.

The system, thus, has a characteristic temperature $T^* \equiv 2V^2/\Delta\varepsilon$. At $T \ll T^*$ we can distinguish two different kind of excitations:

a. low-lying spin excitations (between the singlet and triplet states), with an energy $k_B T$;

b. excitations involving charge degrees of freedom (promotion of an f electron into the ligand orbital), with an excitation energy $\Delta\varepsilon$.

The basic ingredients of this system are the following. At $T = 0$, the ground state is a singlet and the moment of the partially filled F state is zero. When the temperature increases, with $T \ll T^*$, the triplet state starts to be populated. Since the triplet has a moment, the magnetic moment of the f electron starts to appear. For $T \gg T^*$, the magnetic moment is fully present and the singlet character of the ground state is not noticeable.

Kondo Problem: A Single Magnetic Impurity

Now, let us consider the case of a magnetic impurity, e.g. Ce, embedded in a metal. This impurity has a total moment $\boldsymbol{j}$ whose z component is described by the quantum number m. Then the Hamiltonian describing the system is:

$$\begin{aligned} H &= \sum_{\mathbf{k}\sigma} \varepsilon(\mathbf{k}) c^\dagger_{\mathbf{k}\sigma} c_{\mathbf{k}\sigma} + \varepsilon_f \sum_m f^\dagger_m f_m \\ &+ \sum_{\mathbf{k}m\sigma} \left[V^*_{m\sigma}(\mathbf{k}) c^\dagger_{\mathbf{k}\sigma} f_m + V_{m\sigma}(\mathbf{k}) f^\dagger_m c_{\mathbf{k}\sigma} \right] + \frac{U}{2} \sum_{m \neq m'} n^f_m n^f_{m'} \end{aligned} \tag{1.4}$$

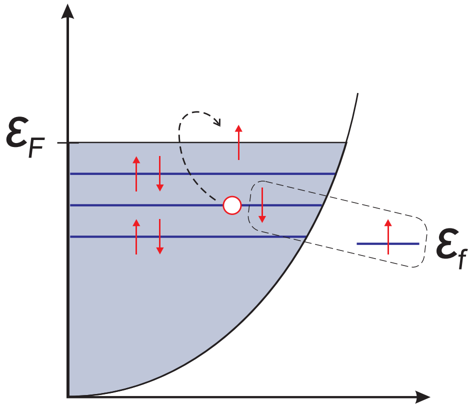

Figure 1.8: *Single magnetic impurity embedded in a metal. After one of the conduction electrons is moved to the Fermi level, the resulting system is similar to the one depicted in Fig. 1.6. The f impurity can form a singlet with the conduction electron which lost its companying electron.*

where, similarly as before, the terms represent the kinetic energy of the conduction electrons (which now form a band), the kinetic energy of the f-electrons (now the f orbital is ν_f-fold degenerate), the hybridization between conduction electrons and the f-electrons, and the electron repulsion between f-electrons, respectively. The situation for $\nu_f = 2$ is represented in Fig. 1.8. If one of the conduction electrons is promoted to the Fermi level, the situation is similar to the one described above for the $L-F$ system. The remaining conduction electron can form a singlet with the f-electron. The difference with the $L-F$ system is that the singlet formation can occur with different conduction-electron states. Those which are closer to ε_F are more important since for them it is easier to promote an electron to the Fermi level. It results that, in the $U \to \infty$ limit and in the presence of weak hybridization, the energy of the singlet state is always lower that the energy of the multiplets, just as in the case presented above. The lowering of the energy due to hybridization is (for details of the calculation see [13]):

$$\varepsilon = -D\,\mathrm{e}^{-|\varepsilon_f|/(\nu_f N(0) V^2)}$$

where a constant density of states is assumed with height $N(0)$ and a lower cutoff D. To this energy it is customary to associate a characteristic temperature T_K (Kondo temperature), $k_B T_K = -\varepsilon$. At $T \ll T_K$ we find again the two kind of excitations characteristic of strongly correlated systems.

The Kondo Lattice

Finally, let us consider an array of magnetic atoms (which is the case of heavy fermion systems). The respective Hamiltonian can be obtained by generalizing

Eq. 1.4:

$$\begin{aligned} H \;=\; & \sum_{\mathbf{k}n\sigma} \varepsilon_n(\mathbf{k}) a^\dagger_{\mathbf{k}n\sigma} a_{\mathbf{k}n\sigma} + \sum_{mi} \varepsilon_{fm} f^\dagger_m(i) f_m(i) \\ & + \frac{1}{\sqrt{N_o}} \sum_{im\mathbf{k}n\sigma} V_{m\sigma}(\mathbf{k},n) \left[a^\dagger_{\mathbf{k}n\sigma} f_m(i) \mathrm{e}^{-\mathbf{i}\mathbf{k}\cdot\mathbf{R_i}} + f^\dagger_m(i) a_{\mathbf{k}n\sigma} \mathrm{e}^{\mathbf{i}\mathbf{k}\cdot\mathbf{R_i}} \right] \\ & + \frac{U}{2} \sum_{i,m\neq m'} n^f_m(i) n^f_{m'}(i) \end{aligned} \tag{1.5}$$

where i labels the N_o f-sites at positions $\mathbf{R_i}$, and n is a band index. In the limit $U \rightarrow \infty$, the previous Hamiltonian can be solved using a mean field approximation [13, 17] where it is assumed that the strong repulsion between the f electrons can be taken into account by a renormalization of the hybridization matrix element $V_{m\sigma}(\mathbf{k},n) \rightarrow rV_{m\sigma}(\mathbf{k},n) = \tilde{V}_{m\sigma}(\mathbf{k},n)$. With this method, we can map the many-body problem (Eq. 1.5) into a one-particle problem:

$$H_{MF} = \sum_{\mathbf{k}l\tau} E_l(\mathbf{k}) c^\dagger_{l\tau}(\mathbf{k}) c_{l\tau}(\mathbf{k}) + \Lambda N_o (r^2 - 1)$$

where $c^\dagger_{l\tau}(\mathbf{k})$ denotes the creation operators of quasiparticles in branch l with pseudospin τ, and Λ is a Lagrange parameter. For the case of one conduction electron band and an f orbital degeneracy $\nu_f = 2$ (so the index m is not necessary), at $T = 0$, two quasiparticle bands are found:

$$E_l(\mathbf{k}) = \frac{1}{2} \left\{ [\varepsilon(\mathbf{k}) + \tilde{\varepsilon}_f] \mp W(\varepsilon(\mathbf{k})) \right\} \tag{1.6}$$

where $W(\varepsilon(\mathbf{k})) = \sqrt{[\varepsilon(\mathbf{k}) + \tilde{\varepsilon}_f]^2 + 4\tilde{V}^2}$, and $\tilde{\varepsilon}_f = \mu + \frac{\tilde{V}^2}{\varepsilon(k_F) - \mu}$ if the condition $E_l(k_F) = \mu$ is applied (μ is the chemical potential). This situation is depicted in Fig. 1.9.

The unknowns r and Λ can be expressed in terms of the system parameters. In particular, it is found that $\Lambda = \nu_f N(0) V^2 \ln\left(\frac{[\varepsilon(k_F)-\mu]\mu}{\tilde{V}^2}\right)$ which permits defining a characteristic temperature:

$$k_B T^* \equiv \mu\, \mathrm{e}^{-\frac{\Lambda}{\nu_f N(0) V^2}} \tag{1.7}$$

With this definition, we obtain $\tilde{\varepsilon}_f = \mu + k_B T^*$. The characteristic temperature T^* is related to the energy gain of the system due to hybridization. In fact it can be shown that the difference between the hybridized system, E, and the energy without hybridization, $E^{(0)}$, is

$$E - E^{(0)} = -k_B T^*$$

The temperature T^* plays the role of a Kondo temperature for the lattice (they are not the same and usually $T^* < T_K$). Calculations at finite temperatures show that there exists a critical temperature of the order of T^* below which there exist

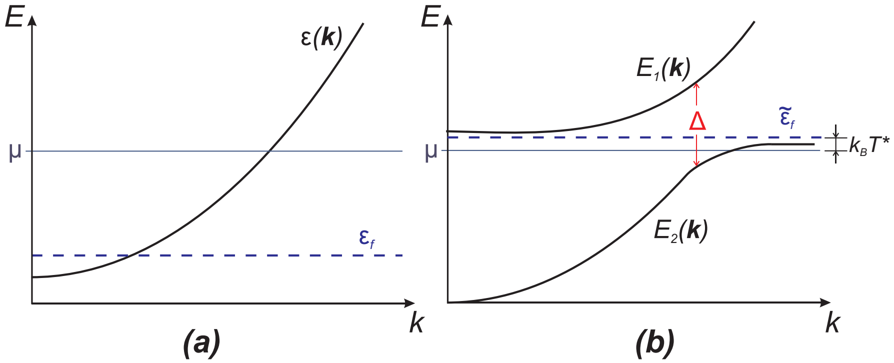

Figure 1.9: *Schematic representation of the hybridization gap (adapted from References [13] and [17]) (a) At high temperatures ($T \gg T^*$), in the Kondo lattice, the conduction electrons and the magnetic moments are independent. (b) At low temperatures ($T \ll T^*$), both set of electrons hybridize, and the system can be represented as renormalized quasiparticles which occupy two bands. If the Fermi energy lies within the lower band, the system is a heavy fermion metal.*

solutions to the problem with $r \neq 0$. Above this critical temperature, it is found that $r = 0$ and the conduction electrons are completely decoupled from the f electrons.

As we have seen, the origin of the heavy fermion behaviour in a Kondo lattice is the weak hybridization between the f electrons with the electrons of neighboring atoms. As in the case of the single impurity problem, there are two different kind of excitations:

a. Low-energy singlet-triplet excitations associated with each f site. A direct evidence of this is the large quasiparticle density of states inferred from the large specific heat (i.e. the f electrons are seemingly located right at the Fermi energy).

b. High-energy excitations involving charge degrees of freedom. This is evinced in photoemission experiments where it takes 2 eV to promote an f electron into an unoccupied conduction electron state above the Fermi energy, in apparent contradiction to the f electrons seemingly located right at ε_F.

As we will see in Chapter 5, with optical spectroscopy it is possible to see both kind of excitations. In particular, the low-energy optical response is a direct consequence of the band structure renormalization depicted in Fig. 1.9.

Because the f sites form a lattice, the excitations are coupled to each other. Below certain temperature T_{coh} (such that $T_{coh} < T^*$), they form coherent quasiparticle states with large effective masses (which are seen in the specific heat, for example). T_{coh} can be approximately determined by measuring the temperature

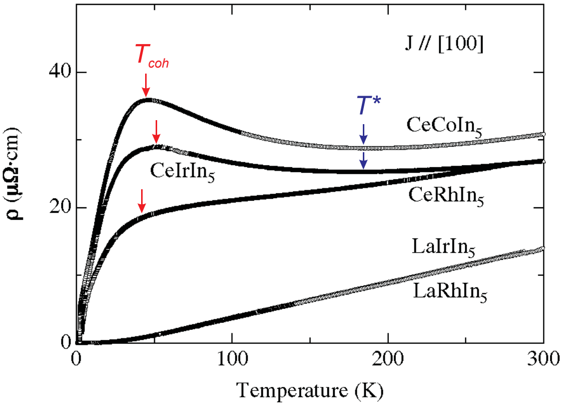

Figure 1.10: *DC resistivity of the heavy fermion compounds studied in Chapter 5 (from [18]). The arrows indicate* T_{coh} *and* T^**, respectively. In these compounds, however, below* T_{coh} *the resistivity is linear with temperature indicating a non-conventional formation of the coherent state. Moreover,* $CeRhIn_5$ *does not show the typical behavior of a heavy fermion system. One reason of the reasons is that this compound orders antiferromagnetically below 4 K. The figure also shows the resistivity of two of the relative compounds not containing f electrons.*

dependence of the DC resistivity (see Fig. 1.10). Starting from high temperatures (usually room temperature), ρ_{DC} decreases with decreasing temperature until it reaches a minimum associated with T^*, from there ρ_{DC} increases (this behavior is similar to the one found in the single impurity system). However, in contrast to the the single impurity problem, ρ_{DC} in the lattice reaches a maximum (labeled as T_{coh}). Below T_{coh}, the resistivity decreases due to the formation of coherent Bloch-like states, and $\rho_{DC} = AT^2$ is observed, typical of electron-electron correlations.

For $T > T_{coh}$, the mean-free path of the excitations of the f electron system becomes so short that the coherence starts to be destroyed and the heavy quasiparticles start to disappear. For $T_{coh} \ll T^*$, the specific heat contains contributions of both the coherent and incoherent part of the f electron excitations. Finally, when $T \gg T^*$, the f electrons can be treated as localized and interacting weakly with the conduction electrons.

1.2.3 Manganites

The phase diagram of the perovskite manganites of the general composition $Re_{1-x}A_xMnO_3$ (Re = rare earth, A = divalent alkali) is extremely rich. For example, see Fig. 1.11 where the phase diagram of one of the best studied manganite system compounds, $La_{1-x}Ca_xMnO_3$, is shown [19]. The origin of this

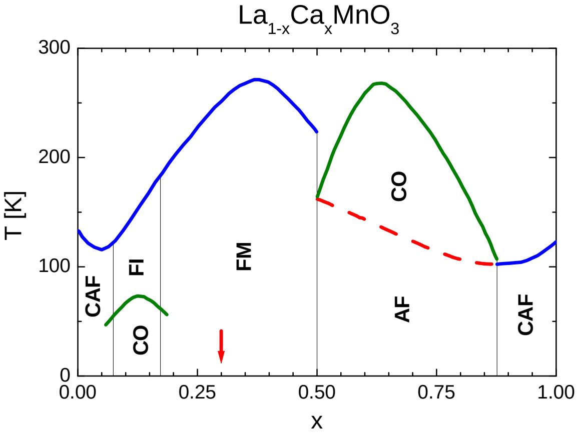

Figure 1.11: *Phase diagram of* $La_{1-x}Ca_xMnO_3$ *(from Ref. [19]). The richness of this phase diagram is evident, it comprise the following states: canted antiferromagnet (CAF), charge order (CO), ferromagnetic insulator (FI), ferromagnet(FM), and antiferromagnet (AF). The arrow indicates the parent compound of the manganites studied in Chapter 6.*

behaviour is also the interrelation between localized and itinerant electrons as we will see below. The difference is that in this case, both electrons pertain to the same class of atoms.

The basic crystal structure of the manganites is shown in Fig. 1.12. The main point here is that the Mn ion is surrounded by O atoms forming an octahedron. In a perfect octahedron, the crystal field leaves partially the degeneracy of the d levels forming a triple degenerate, t_{2g}, and a double degenerate, e_g, states. The distortions usually present in the octahedron alters this splitting depending on whether the e_g level is occupied or not (see Fig. 1.12). When it is occupied, the e_g level is further split (Jahn-Teller splitting), otherwise this level decreases its energy if it is occupied in a short time scale (like in optical transitions) compared to the response of the lattice. Let us consider the two extremes of the phase diagram of Fig. 1.11. $CaMnO_3$ has the ionic composition $Ca^{+2}Mn^{+4}O_2^{-2}$ [20]. Therefore, the manganese atom has three electrons occupying the t_{2g} level that, due to the strong Hund's coupling, J_H, form a large (classical) spin, $\boldsymbol{S}$. These classical spins tend to align antiferromagnetically between them. On the other hand, in $LaMnO_3$ manganese is present as Mn^{+3} and, therefore, has an itinerant electron occupying the e_g level that tends to align with the spin of the t_{2g} core due to J_H. Between these two extremes, both Mn ions are present in the ratio $Mn^{+3}/Mn^{+4} = x$. The situation described is known as the *double exchange* mechanism and was already proposed by Zener [20] in the fifties just after the discovery of the interesting

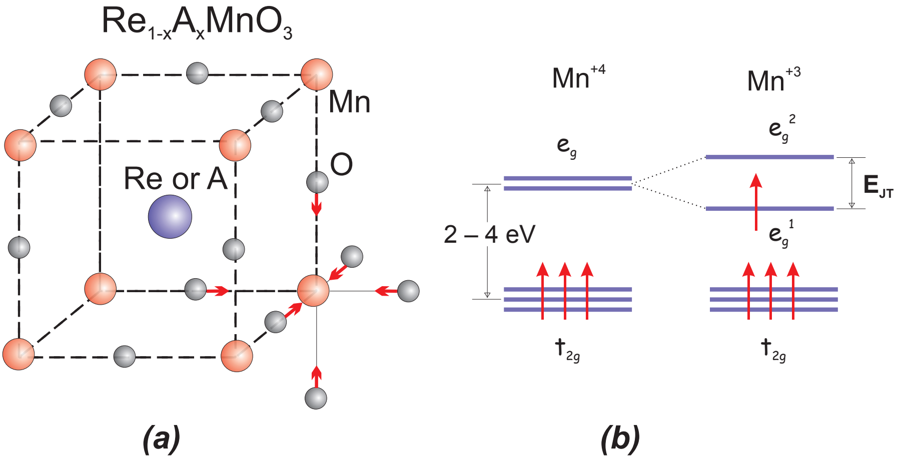

Figure 1.12: *(a) Basic crystal structure of the manganites. One of the main important points to notice is the octahedral surrounding of the Mn atoms. (b) In a perfect environment, its degenerate d levels are split in the triple degenerate t_{2g} and double degenerate e_g. A distortion of the octahedron, like the one indicated by arrows, alters this situation depending on whether the e_g level is occupied or not. If e_g is occupied, it is further split. If not, the e_g level can lower its energy if it is occupied in a short time scale [19].*

properties of the manganites [21]. The double exchange (DE) Hamiltonian is:

$$H = -t \sum_{\langle ij \rangle} c^{\dagger}_{i\sigma} c_{j\sigma} + J \sum_{\langle ij \rangle} \boldsymbol{S}_i \boldsymbol{S}_j - J_H \sum \boldsymbol{S}_i c^{\dagger}_{i\sigma} \boldsymbol{\sigma} c_{i\sigma} \tag{1.8}$$

There are no doubts that the DE Hamiltonian contains the most important physics describing the manganites, especially in describing, at least qualitatively, the ferromagnetic state. However, another mechanism and ideas have to be added for a complete description, although to what extent is still matter of discussion [22]. The most notorious are electron-lattice coupling [19] and phase segregation [23]. Besides the electron-lattice coupling described above (lattice distortions producing modifications in the electron configuration), there is another type called *tolerance factor* [19]. It originates from the fact that the atoms Re and A, in $\mathrm{Re}_{1-x}\mathrm{A}_x\mathrm{MnO}_3$, have different radiuses producing different stresses in the Mn-O-Mn bonds. This, in turn, produces buckling of the MnO_6 octahedron, which changes the Mn-Mn electron hoping [24]. Electron-phonon coupling makes the carriers have a tendency to *self trapping*: the presence of an electron in a given Mn orbital disturbs the lattice which in turn produce a potential minimum that tend to keep the electron in that orbital [19]. If the coupling is strong enough a self trapped state, called *polaron*, can be formed. Polaron states, indeed, have been seen in the optical spectra of manganites. Other indication given by optics regarding the importance of lattice distortions is the different spectra obtained in cleaved and polished samples. These two points will be discussed in Chapter 6. There, we will also discuss the large isotope effect in some manganites that also point to the importance to electron-phonon coupling.

The other idea that has to be included in describing the manganites is phase separation. The traditional treatment of Eq. 1.8 for $J_H \gg t > J$ concludes that hole doping (increasing x) of the AF state produces a canting of the spins until a certain crital concentration is reached where the material becomes FM [25]. However, from the same treatment it is found that the compressibility $\partial^2 E/\partial^2 x < 0$, where E is the electron energy [26]. This means that the canted phase is unstable and tends to phase separate. The same conclusion has been found by numerical calculations [27, 28] and more elaborate treatments of the DE Hamiltonian [28, 29]. In particular, in Ref. [28] it was found a phase diagram similar to the one found in the traditional treatment [25] with the difference that the canted phase was replaced by a region with phase separation. The phase separated phases, however, will not be large as Coulomb repulsion tends to homogenize the system [26, 23]. In Chapter 6 we will see that the optical data in $(\mathrm{La}_{0.5}\mathrm{Pr}_{0.5})_{0.7}\mathrm{Ca}_{0.3}\mathrm{MnO}_3$ thin films can also be interpreted in terms of phase separation.

1.3 Spectral Weight and Strong Correlations

One quantity that we will study in this thesis is the spectral weight contained in the optical conductivity. As we will see in this section, it contains information about strong correlations present in a a given material. Starting from the Kubo formula, it has been demonstrated [30, 31] that the real part of the optical conductivity complies with:

$$\int_0^\infty \sigma_1(\omega)\mathrm{d}\omega = -\frac{1}{2\hbar}\pi \mathrm{i} V\langle[\mathcal{P},\mathcal{J}]\rangle \tag{1.9}$$

where V is the total volume and $\mathcal{P}$ and $\mathcal{J}$ are the polarization and current density operators, respectively. The important point is that if *all electrons and all bands* are included [32] the current and polarization operators are given by:

$$\begin{aligned} \mathcal{J} &= \frac{e}{Vm}\sum_i p_i\,\delta(r-r_i) \\ \mathcal{P} &= \frac{e}{V}\sum_i r_i\,\delta(r-r_i) \end{aligned}$$

With these relations, Eq. 1.9 can be written as:

$$\int_0^\infty \sigma_1(\omega)\mathrm{d}\omega = \frac{\pi n e^2}{2m} \tag{1.10}$$

where $n \equiv N/V$. This expression is, evidently, temperature independent.

Now, in strongly correlated systems the electronic states of interest seem to be located in narrow bands well separated from other bands [2]. Therefore, tight binding models considering only few bands, such as the Hubbard and Anderson hamiltonians, are used to describe these systems. Within these models, if only nearest neighbor hopping is considered and the system has orthorombic symmetry, the current and polarization operators in a given direction are (for simplicity, summations in the spin degree of freedom are omitted)[31]:

$$\begin{aligned} \mathcal{J} &= \mathrm{i}\frac{eat}{\hbar V}\sum_i \left(c_{i+1}^\dagger c_i - c_i^\dagger c_{i+1}\right) \\ \mathcal{P} &= \frac{ea}{V}\sum_i i c_i^\dagger c_i \end{aligned}$$

where a is the distance between neighboring sites in the considered direction and t is the hopping parameter. Then, Eq. 1.9 can be written as [31]:

$$\int_0^\infty \sigma_1(\omega)\mathrm{d}\omega = -\frac{\pi n e^2 a^2}{2\hbar^2}\langle K\rangle \tag{1.11}$$

where $K = -t\sum_i(c_i^\dagger c_{i+1} + c_{i+1}^\dagger c_i)$ is the kinetic energy of the conduction electrons. The kinetic energy depends on temperature and interaction strength. Therefore, the integrated optical conductivity contain information about the interactions [2]. Moreover, it will have a strong temperature dependence. Equation 1.11 also implies that there should be a transfer of spectral weight to high frequencies, i.e. to energies corresponding to the bands that were not included in the model [32].

In the following chapters we will see that in strongly correlated systems there is, indeed, a large transfer of spectral weight between low to high energies. The range were this transfer occurs depends on the bands involved. In the systems containing d electrons (silicides and manganites), this range is much larger than those involving f electrons (heavy fermion systems).

1.4 Scope of This Thesis

This thesis will start with a short review of the basic concepts of optical spectroscopy, as well as of the experimental techniques used (Chapter 2). The following two Chapters deal with the optical properties of several transition-metal monosilicides. In Chapter 3 one of them, MnSi, is studied thoroughly. Although it is considered as a typical example of a weak ferromagnet described by the SCR theory, it will be seen that is not the case. Particular emphasis will be given to the low frequency properties studied by means of a not so often used optical technique, grazing incidence reflectivity. Chapter 4 studies FeSi, CoSi, and some solid solutions between them. FeSi is a system that has been studied for a relatively long time. It is not clear if the insulating non-magnetic ground state should be described by an itinerant or a Kondo-like picture. By studying the transferred spectral weight it will be argued that the latter is more appropriate. Although CoSi, as FeSi, is not magnetic, solid solutions between them present, surprisingly, magnetism. Their optical properties are different from other well studied magnetic materials. After studying these itinerant systems, a family of heavy fermion systems (CeMIn$_5$) will be studied in Chapter 5. In this material it is clear that there exist itinerant and localized electrons. The interaction between them gives rise to the heavy fermion behaviour at low temperatures. The formation of this *condensate* is characterized by a hybridization gap which is pretty clear in the optical response. As in the silicides, there is a transfer of spectral weight but the region where it occurs is much smaller. Finally, another system containing localized and itinerant electrons will be studied. Chapter 6 present the optical properties of (La$_{1-y}$Pr$_y$)$_{0.7}$Ca$_{0.3}$MnO$_3$ (y = 0.5) thin films. Phase separation and transfer of spectral weight will be analyzed. Moreover, a comparison between films containing different oxygen isotopes will be made.

Chapter 2

Optical Spectroscopy: Fundamental Relations & Experimental Techniques

The purpose of performing optical spectroscopy in a given material is to determine its complex dielectric function (or, equivalently, the optical conductivity) in the largest possible photon energy range. The dielectric function will, then, give information of the electronic structure of the material, of other excitations occurring in the material, and possibly the mechanism driving transitions to states such as superconductivity or magnetism. For that purpose, we have made an extensive use of different well known optical tools. Although they are already well described in the literature, the aim of the present chapter is to present in a concise way the fundamental concepts of optical spectroscopy and the correspondent experimental tools. For a more complete analysis of the fundamental concepts we refer to the classic textbook of Wooten[33] or the more recent one by M. Dressel and G. Grüner[34].

2.1 Dielectric function and optical conductivity

The interaction of light with matter is fully described by Maxwell's equations. The specific properties of the material can be taken into account relating the induction with the magnetic field strength ($\boldsymbol{B} = \mu_1 \boldsymbol{H}$), and the external electric field, i.e. the one that polarizes the medium, with the total electric field ($\boldsymbol{E}_{ext} = \epsilon_1 \boldsymbol{E}$). Moreover, if we separate the different contributions to the charge density and the current density (see Table 2.1 for a summary of such decomposition) and assume a linear response between the electric field and the motion of the conduction electrons it produces ($\boldsymbol{J}_{cond} = \sigma_1 \boldsymbol{E}$), Maxwell's equations can be rewritten as:

Table 2.1: *Relationships showing the decomposition of different electric quantities.*

Electric field	$\boldsymbol{E} = \left\{ \begin{array}{ll} \boldsymbol{E}_{ext} & = \epsilon_1 \boldsymbol{E} \\ + & \\ \boldsymbol{E}_{ind} & = -4\pi \boldsymbol{P} \end{array} \right.$
Current density	$\boldsymbol{J} = \left\{ \begin{array}{l} \left. \begin{array}{ll} \boldsymbol{J}_{pol} & = \frac{\partial \boldsymbol{P}}{\partial t} \\ + & \\ \boldsymbol{J}_{mag} & = c \nabla \times \boldsymbol{M} \\ + & \\ \boldsymbol{J}_{cond} & = \sigma_1 \boldsymbol{E} \end{array} \right\} \boldsymbol{J}_{ind} \\ + \\ \boldsymbol{J}_{ext} \end{array} \right.$
Charge density	$\rho = \left\{ \begin{array}{l} \rho_{pol} \\ + \\ \rho_{ext} \end{array} \right.$

$$\begin{aligned}
\nabla \cdot \boldsymbol{E}_{ext} &= 4\pi \rho_{ext} \\
\nabla \times \boldsymbol{E} &= -\frac{1}{c}\frac{\partial \boldsymbol{B}}{\partial t} \\
\nabla \cdot \boldsymbol{B} &= 0 \\
\nabla \times \boldsymbol{B} &= \frac{\mu_1 \epsilon_1}{c}\frac{\partial \boldsymbol{E}}{\partial t} + \frac{4\pi\sigma_1\mu_1}{c}\boldsymbol{E} + \frac{4\pi\mu_1}{c}\boldsymbol{J}_{ext}
\end{aligned}$$

Now, let us assume that the electric fields can be decomposed into a complete set of plane waves $[\boldsymbol{E}(\boldsymbol{r},t) = \int\int d\boldsymbol{q}\, d\omega \boldsymbol{E}(\boldsymbol{q},\omega)\exp(i\boldsymbol{q}\cdot\boldsymbol{r} - i\omega t)]$. If we make a Fourier analysis of the previous equations and decompose the fields in longitudinal (parallel to $\boldsymbol{q}$) and transverse (perpendicular to $\boldsymbol{q}$), it can be shown that for isotropic materials:

$$\boldsymbol{J}^{L,T}_{ind}(\boldsymbol{q},\omega) = \frac{i\omega}{4\pi}\left[1 - \epsilon^{L,T}(\boldsymbol{q},\omega)\right]\boldsymbol{E}^{L,T}(\boldsymbol{q},\omega) \tag{2.1}$$

where the transverse and longitudinal dielectric functions are defined as

$$\begin{aligned}
\epsilon^L &\equiv \epsilon_1 + i\frac{4\pi\sigma_1}{\omega} \\
\frac{\omega^2}{c^2}\left(\epsilon^T - \epsilon^L\right) &\equiv q^2\left(1 - \frac{1}{\mu_1}\right)
\end{aligned}$$

As we can see, in the long-wavelength limit ($\boldsymbol{q} \to 0$), the transverse and longitudinal dielectric function are equal (i.e. the medium cannot distinguish between fields parallel or perpendicular to $\boldsymbol{q}$). In principle, a longitudinal (transverse) field can produce transverse (longitudinal) currents. In fact, it is possible to obtain the following relation

$$\boldsymbol{J}_{ind}(\boldsymbol{q}, \omega) = \frac{i\omega}{4\pi} \left[\mathbf{1} - \boldsymbol{\epsilon}(\boldsymbol{q}, \omega) \right] \boldsymbol{E}(\boldsymbol{q}, \omega) \tag{2.2}$$

where $\boldsymbol{\epsilon}$ is the *dielectric function tensor* and from which Equations 2.1 can be obtained. Eq. 2.2 also defines the *optical conductivity tensor*:

$$\boldsymbol{\sigma}(\boldsymbol{q}, \omega) = \frac{i\omega}{4\pi} \left[\mathbf{1} - \boldsymbol{\epsilon}(\boldsymbol{q}, \omega) \right] \tag{2.3}$$

In a crystal with a symmetry at least as high as orthorhombic, both tensors can be diagonalized by choosing the appropriate axes which coincide with the crystallografic axes. Since those elements can be studied independently, in the rest of this book we will omit the tensorial character of the dielectric function. Furthermore, for optical radiation we will only consider the long-wavelength limit.

2.2 Properties of the Optical Conductivity

Here we want to summarize the properties of the optical conductivity. The first properties we want to discuss are consequence of recognizing the optical conductivity as a response function. To see that, let us consider any local (independent of $\boldsymbol{r}$) response function, $G(t, t')$, that describes the response of a system, $X(t)$, at a particular time t to a given stimuli, $f(t')$, acting at all times t':

$$X(t) = \int_{-\infty}^{\infty} G(t, t') f(t) \, \mathrm{d}t'$$

The response function should be function of the time interval $t - t'$ since this is the time during which the stimuli acts. Furthermore, we consider *causality* that is the response function is larger than zero only for time intervals larger than zero. With these considerations the previous equation can be written as $X(\omega) = G(\omega) f(\omega)$ after it is Fourier transformed. In this form we can recognize that the optical conductivity is a response function describing the induced density current as a result of an applied electric field (see Equations 2.2 and 2.3). In particular, the Fourier transform of the response funtion is given by

$$G(\omega) = \int G(t - t') \mathrm{e}^{i\omega(t-t')} \mathrm{d}t$$

from which, the first property is evident:

$$\mathbf{1.}\ \sigma(-\omega) = \sigma^{\star}(\omega) \tag{2.4}$$

Let us consider imaginary frequencies in the expressions for the response functions. The causality principle restricts the response function to the upper plane of the complex plane, i.e. $G(\omega)$ has no poles in this plane. Then, applying Cauchy's theorem, relations between the real and imaginary part of the response function can be obtained. These relations, after further simplification using Eq. 2.4, can be written as:

$$\textbf{2.}\ \sigma_1(\omega) = \frac{2}{\pi}\mathcal{P}\int_0^\infty \frac{\omega'\sigma_2(\omega')}{\omega'^2-\omega^2}\,\mathrm{d}\omega' \tag{2.5}$$

$$\sigma_2(\omega) = -\frac{2\omega}{\pi}\mathcal{P}\int_0^\infty \frac{\sigma_1(\omega')}{\omega'^2-\omega^2}\,\mathrm{d}\omega' \tag{2.6}$$

They are the well known Kramers-Kronig (KK) relations. These relations can, evidently, be applied also to the dielectric function. It is just necessary to recognize that the appropriate response function in that case is $\epsilon(\omega) - 1$.

The combination of the KK relations with physical arguments about the behavior of the response function conducts to useful expressions known as sum-rules. Although the sum-rules expressions are general, to demonstrate them it is easy to consider a particular model, e.g. the Drude model (§2.4). The most widely used sum-rule is that one involving the real part of the optical conductivity:

$$\textbf{3.}\ \int_0^\infty \sigma_1(\omega)\,\mathrm{d}\omega = \frac{\pi N e^2}{2m} \equiv \frac{\omega_p^2}{8} \tag{2.7}$$

where N is the total number of electrons per unit volume, e and m are the electron charge and mass, respectively, and ω_p is known as plasma frequency. This integral gives a quantity independent of temperature and hence the name of sum-rule. A point of interest in this book will be the actual frequency range where the sum-rule applies. Equation 2.7 suggest the following definition for the study of the spectral weight in the optical conductivity:

$$N_{eff}(\omega) = \frac{2mV}{\pi e^2}\int_0^\omega \sigma(\omega')d\omega' \tag{2.8}$$

where V is the volume of one unit. Evidently, when $\omega \to \infty$ this quantity is equal to the total number of electrons contained in the considered unit.

Finally we have two properties that can be identified from the definition of the real part of the optical conductivity ($\boldsymbol{J}_{cond} = \sigma_1\boldsymbol{E}$):

$$\textbf{4.}\ \sigma_1(\omega) > 0 \tag{2.9}$$

$$\textbf{5.}\ \lim_{\omega\to 0}\sigma_1(\omega) = \sigma_{DC} \tag{2.10}$$

2.3 Fresnel Equations for Reflection and Transmission at a Single Interface

Let us consider an electromagnetic wave interacting with a medium as depicted in Fig. 2.1. By applying the appropriate boundary conditions (continuity of the tangential components of both the electric and magnetic vectors) to the solutions to the Maxwell equations, it is possible to relate the incident electromagnetic wave with the reflected and transmitted waves. In the case of non magnetic materials (or magnetic materials at optical frequencies) the relations, known as Fresnel equations, are:

$$r_s(\omega) = \frac{E_{rs}}{E_{is}} = \frac{n_{(0)}\cos\theta_{(0)} - n_{(1)}\cos\theta_{(1)}}{n_{(0)}\cos\theta_{(0)} + n_{(1)}\cos\theta_{(1)}} \tag{2.11}$$

$$t_s(\omega) = \frac{E_{rs}}{E_{ts}} = \frac{2n_{(0)}\cos\theta_{(0)}}{n_{(0)}\cos\theta_{(0)} + n_{(1)}\cos\theta_{(1)}} \tag{2.12}$$

$$r_p(\omega) = \frac{E_{ps}}{E_{ip}} = \frac{n_{(0)}\cos\theta_{(1)} - n_{(1)}\cos\theta_{(0)}}{n_{(0)}\cos\theta_{(1)} + n_{(1)}\cos\theta_{(0)}} \tag{2.13}$$

$$t_p(\omega) = \frac{E_{rp}}{E_{tp}} = \frac{2n_{(0)}\cos\theta_{(0)}}{n_{(0)}\cos\theta_{(1)} + n_{(1)}\cos\theta_{(0)}} \tag{2.14}$$

where $n_{(i)} \equiv \sqrt{\epsilon_{(i)}}$. The transmission angle can be eliminated from the previous equations using Snell's law:

$$\frac{\sin\theta_{(0)}}{\sin\theta_{(1)}} = \frac{n_{(1)}}{n_{(0)}} \tag{2.15}$$

2.3.1 Reflection at low frequencies in bulk materials

Experimentally, for bulk materials, r_s and r_p can be obtained directly via ellipsometry (§2.5) or using the KK relations via reflectivity (§2.6). In a reflectivity experiment the quantities that can be measured are the reflectivities R_s and R_p. They correspond to the square of the absolute values of the reflection coefficients r_s and r_p, respectively. At low enough frequencies of the incident light, useful relations can be obtained if we start from the Fresnel equations. For simplicity let us take $\epsilon_{(0)} = 1$, $\epsilon_{(1)} = \epsilon(\omega)$, and $\theta_{(0)} = \theta$. If $\epsilon_2(\omega) \gg 1$,[*] which is usually

---

[*] Be aware of the notation we are using. For a given complex quantity X, X_1 and X_2 represent its real and imaginary part, respectively. When this numbers are between parenthesis, they represent the optical properties of different layers. This will be important in §2.7

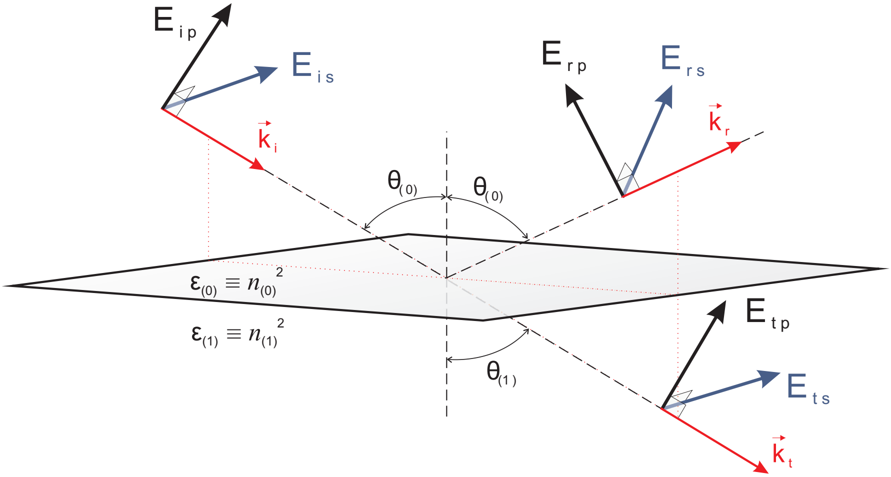

Figure 2.1: *Reflection and transmission in a single interface.*

the case for metals at low frequencies, from Eq. 2.13 it is possible to obtain the following expression for the reflectivity in the p-polarization:

$$R_p(\omega) = 1 - \frac{2\omega^{1/2}}{\cos\theta}\mathrm{Re}\left[\frac{1}{\sqrt{i\pi\sigma(\omega)}}\right] \tag{2.16}$$

If $\sigma_1(\omega) \gg \sigma_2(\omega)$ and $\sigma_1(\omega) \approx \sigma_{DC}$, the previous equation can be further simplified to:

$$R_p(\omega) = 1 - \frac{2\omega^{1/2}}{\cos\theta\sqrt{2\pi\sigma_{DC}}} \tag{2.17}$$

This means that, under the previous assumptions, the p-polarized reflectivity is solely proportional to $\omega^{1/2}$. This behavior is known as the Hagen-Rubens limit which is a characteristic of most metals.

2.4 Modeling the optical conductivity

In order to study the experimental results, we will rely on known models to distinguish the different contributions to the optical conductivity. Those models have to comply with the relations presented in the previous section. However, some of the generally used models do not satisfy with all the properties of a physical optical conductivity but can still be applicable in a limited frequency range.

2.4.1 The Drude-Lorentz model

The simplest microscopical model to describe the response of the medium to an electromagnetic field ($\boldsymbol{E}$) is the Lorentz model. In that model we consider an electron (of mass m and charge e) bound to the nucleus in a similar way a small mass can be bounded to a large one:

$$m\ddot{\boldsymbol{r}} + m\Gamma\dot{\boldsymbol{r}} + m\omega_o\boldsymbol{r} = -e\boldsymbol{E}$$

where we have also considered viscous damping. From here it is easy to show that in such a case the dielectric function is given by:

$$\epsilon(\omega) = 1 + \frac{\omega_p^2}{(\omega_o^2 - \omega^2) - i\Gamma\omega} \tag{2.18}$$

where ω_p^2 is defined as in §2.2. Using Eq. 2.3 the optical conductivity in this model is found to be:

$$\sigma(\omega) = \frac{\omega_p^2}{4\pi}\frac{\omega}{i(\omega_o^2 - \omega^2) + \Gamma\omega}$$

Free electrons are not bound and the correspondent optical conductivity is obtained by setting $\omega_o = 0$ but keeping the damping term (free electrons cannot absorb photons at a finite frequency). This gives rise to the well known Drude model often used to describe the low frequency response of metals.

To analyze experimental data, one usually takes a model dielectric function which is the combination of one Drude peak and various Lorentz oscillators:

$$\epsilon(\omega) = \epsilon_\infty - \frac{\omega_p^2}{\omega(\omega + i\Gamma)} + \sum_j \frac{\omega_{p,j}^2}{(\omega_{o,j}^2 - \omega^2) - i\omega\Gamma_j} \tag{2.19}$$

where we have introduced the additional parameter ϵ_∞ which is the value of the dielectric function when $\omega \to \infty$. It is easy to see that in Eq. 2.18, $\epsilon_\infty = 1$. One has to be careful when calculating the optical conductivity if $\epsilon_\infty \neq 1$. This is specially true when one wants to extract the response of the free carriers from the far infrared conductivity. In this region, the effect of the high frequency bound oscillators is subsumed in an $\epsilon_\infty > 1$.

To illustrate the different contributions to the optical properties in the Drude-Lorentz model, let us consider Eq. 2.19 with the parameters given in Table 2.2. The corresponding $\sigma_1(\omega)$, $\epsilon_1(\omega)$, and normal incidence reflectivity ($\theta = 0$) are plotted in Fig. 2.2. In the real part of the optical conductivity, Fig. 2.2(a), we can easily recognize at low frequencies the Drude contribution and at high frequencies the Lorentz oscillator whose maximum coincides with its position as indicated by the arrow. The inset of Fig. 2.2(a) shows the phase of the optical conductivity (plus a constant). Its meaning will be clear in the following subsection.

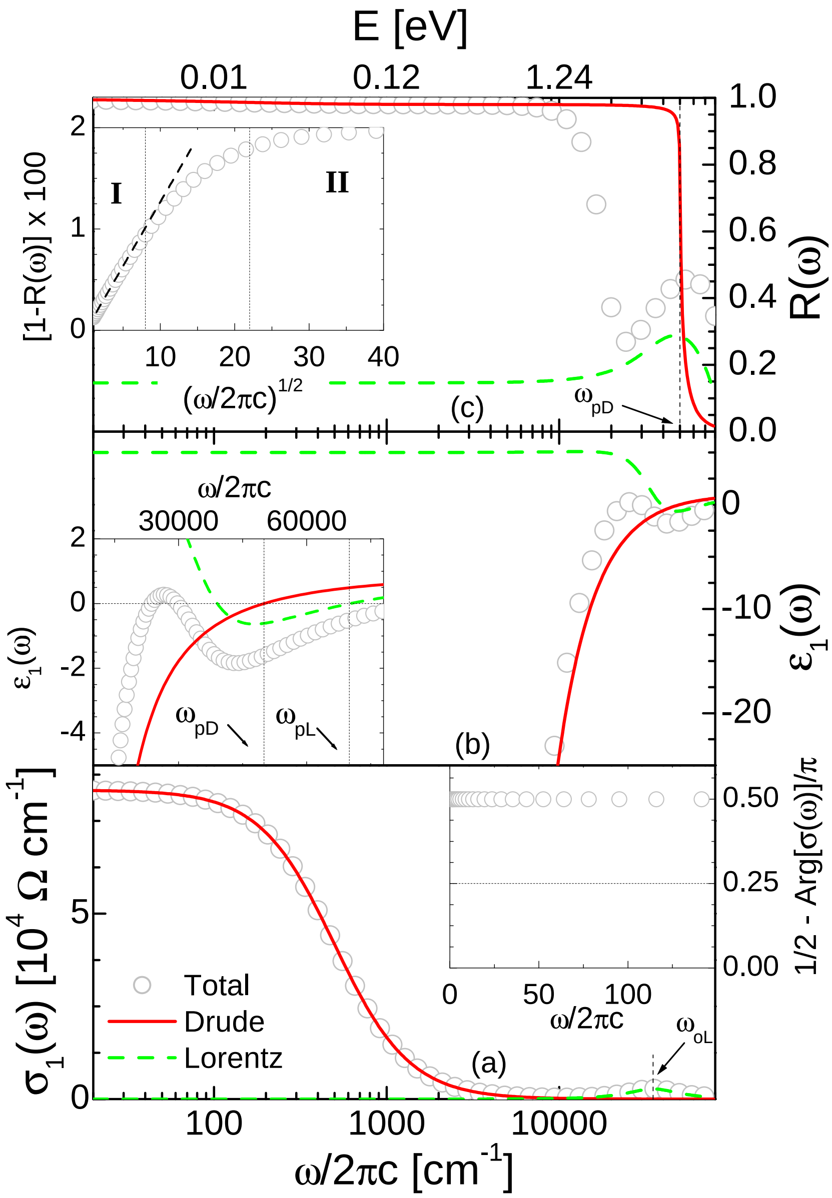

Figure 2.2: *Real parts of the optical conductivity and the dielectric function, and normal incidence reflectivity of a model containing one Drude and one Lorentz oscillator. The parameters are given in Table 2.2. The insets show expanded views in selected frequency ranges.*

Table 2.2: *Parameters, in cm^{-1}, corresponding to the Drude, NFL and Lorentz oscillators used to plot Figures 2.2 and 2.3. For both plots, the parameter ϵ_∞ has taken to be equal to 1.*

Oscillator	ω_o	ω_p	Γ	γ	η
Drude	0	50000	500	–	–
NFL	0	50000	500	1	0.25
Lorentz	35000	70000	30000	–	–

The real part of the dielectric function is shown in Fig. 2.2(b). For comparison purposes in both the Drude and Lorentz contributions we have added ϵ_∞. As indicated in the inset of Fig. 2.2(b), the zero crossing of the Drude oscillator and the second crossing of the Lorentz are close to their respective plasma frequencies. As a result of combining both contributions, the total $\epsilon_1(\omega)$ shows a maximum that, depending on the relative strengths of the contributions, can produce two extra zero crossings.

Finally, in Fig. 2.2(c) we have plotted the resulting normal incidence reflectivity, $R(\omega)$. As in the previous case, for comparison, we have added ϵ_∞ to both contributions to calculate their corresponding reflectivities. The reflectivity associated to the Drude peak shows a sharp decrease that corresponds to its plasma frequency. At low frequencies [inset of Fig. 2.2(c)], we recognize two different frequency ranges corresponding to:

I: $\omega \ll \Gamma$. From Eq. 2.18 and its corresponding optical conductivity it is easy to show that for the Drude contribution in this energy range:

$$\begin{aligned} \sigma_1(\omega) &\approx \sigma_{DC} = \frac{\omega_p^2}{4\pi\Gamma} \\ \epsilon_1(\omega) &\rightarrow -\infty \end{aligned}$$

These are the necessary conditions for entering to the Hagen-Rubens limit, Eq. 2.17, which in this case reduces to:

$$R(\omega) \approx 1 - \frac{2^{3/2}\Gamma^{1/2}}{\omega_p \cos\theta}\omega^{1/2}$$

This limit is shown in the dashed line of the inset of Fig. 2.2(c)

II: $\Gamma \ll \omega \ll \omega_p$. In this region, the Drude optical conductivity can be approximated to $\sigma(\omega) \approx \frac{\omega_p^2 i}{4\pi\omega}\left(1 - \frac{i\Gamma}{\omega}\right)$. Therefore:

$$\begin{aligned} \sigma_1(\omega) &\approx \frac{\omega_p^2\Gamma}{4\pi\omega^2} \\ \epsilon_1(\omega) &\approx -\frac{\omega_p^2}{\omega^2} \end{aligned}$$

In this case we are not any more in the Hagen-Rubens limit. However, Eq. 2.16 is still valid, and the normal incidence reflectivity can be written as

$$R(\omega) \approx 1 - \frac{2\Gamma}{\omega_p \cos\theta}$$

In this range the reflectivity is frequency independent.

This limiting behaviours are often used to recognize deviations from the Drude model in metals. This deviation has indeed seen in various compounds. The most well known case is in the optical response of the high-T_C superconductors where other frequency dependencies are seen [35].

2.4.2 Beyond the Drude model

Various metallic compounds have shown deviations from the Drude formulation. Recently, a simple analytical extension to this formulation has been proposed [36]:

$$\sigma(\omega) = \frac{\omega_p^2}{4\pi} \frac{i}{(\omega + i\gamma)^{1-2\eta}(\omega + i\Gamma)^{2\eta}} \tag{2.20}$$

This expression reduces to the the Drude formulation for $\eta = 0$ and 0.5, and $\gamma = \Gamma$. Moreover, it complies with all the properties discussed in §2.2.

In the spirit of the previous subsection, we plot $\sigma_1(\omega)$, $\epsilon_1(\omega)$, and $R(\omega)$ in Fig. 2.3 for a model containing one oscillator given by Eq. 2.20 (in the following we will refer to this expression as a NFL oscillator) and one Lorentz oscillator. The respective parameters are given in Table 2.2. Notice that we have chosen $\gamma \ll \Gamma$ with the latter parameter equal to the scattering rate of the Drude model to facilitate a comparison. The behaviour at high frequencies is similar to the previous case. At low frequencies, however, the situation is different. We identify various frequency ranges:

I: $\omega \ll \gamma$. In this case we arrive to the Hagen-Rubens limit:

$$R(\omega) \quad \approx \quad 1 - \frac{2^{3/2}\gamma^{1/2-\eta}\Gamma^{\eta}}{\omega_p \cos\theta}\omega^{1/2}$$

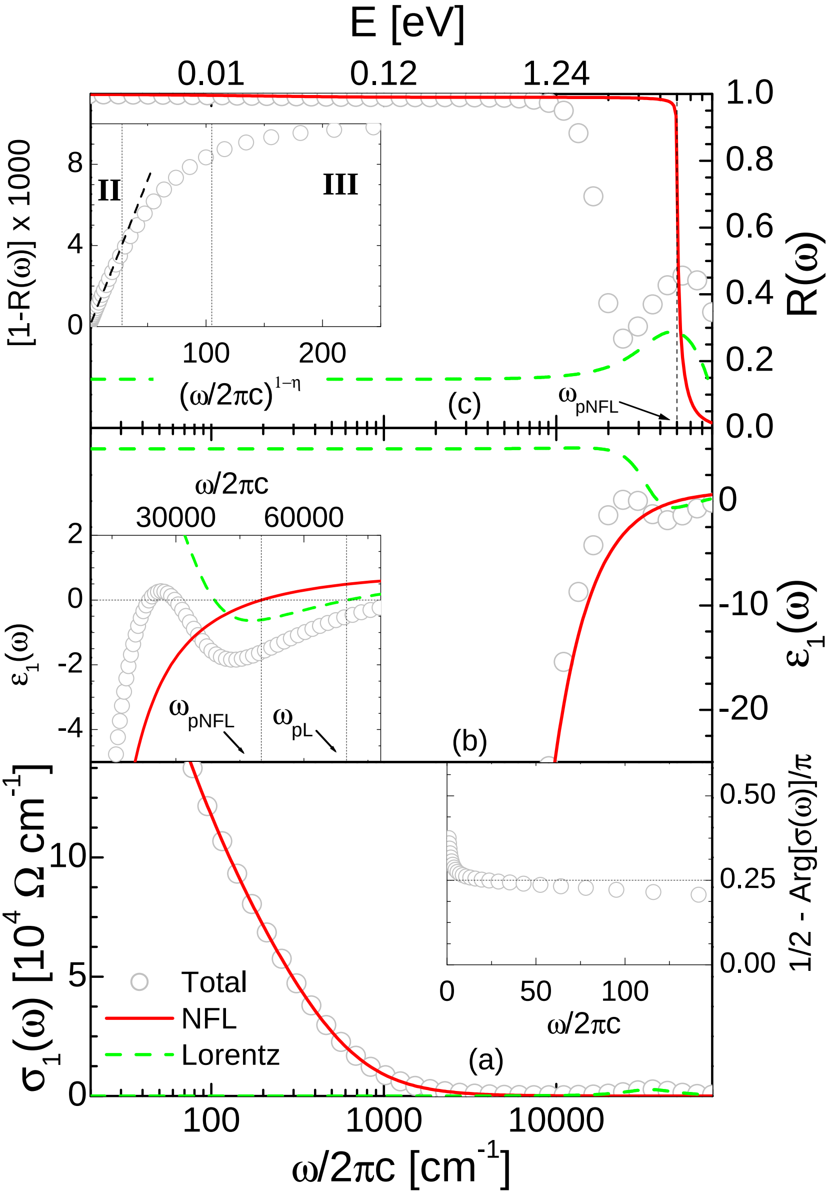

Figure 2.3: *Real parts of the optical conductivity and the dielectric function, and normal incidence reflectivity of a model containing one NFL and one Lorentz oscillator. The parameters are given in Table 2.2. The insets show expanded views in selected frequency ranges.*

II: $\gamma \ll \omega \ll \Gamma$. For this region Eq. 2.20 reduces to[†]:

$$\sigma(\omega) \approx \frac{\omega_p^2}{4\pi\omega\Gamma^{2\eta}} (-i\omega)^{2\eta-1} \tag{2.21}$$

We have an optical conductivity which follows a power law. In this particular case it coincides with the expression suggested by P. W. Anderson to describe the optical conductivity of the cuprate high T$_c$ superconductors [35]. Moreover, it has been shown that close to a quantum critical point (QCP), scale invariance forces optical conductivity to follow a power law dependence [37]. From Eq. 2.21 we can see that in this case the phase of the optical conductivity is constant and it is easily shown that

$$\eta \approx 1/2 - \arg[\sigma(\omega)]/\pi \tag{2.22}$$

We have plotted this quantity in the insets of Figures 2.2(a) and 2.3(a). As expected $1/2 - \arg[\sigma(\omega)]/\pi$ gives 0.5 and 0.25 for the Drude and NFL cases, respectively. The effect of having the exponent $\eta \neq 0.5$ can also be seen in the reflectivity. Indeed, using Eq. 2.16, it can be shown that it also has a power law dependence:

$$R_p(\omega) = 1 - \frac{4\Gamma^\eta \sin(\eta\pi/2)}{\omega_p \cos\theta} \omega^{1-\eta} \tag{2.23}$$

which reduces to the Hagen-Rubens limit for $\eta = 0.5$. The dashed line of the inset of Fig. 2.3(c) shows this dependency.

III: $\Gamma \ll \omega \ll \omega_p$. In this region, the optical conductivity reduces to:

$$\sigma(\omega) \approx \frac{\omega^2 i}{4\pi\omega} \left[1 - (1-2\eta)\frac{i\gamma}{\omega}\right] \left[1 - 2\eta\frac{i\Gamma}{\omega}\right]$$

from where we obtain again a constant reflectivity:

$$R_p(\omega) = 1 - \frac{4}{\omega_p \cos\theta} [(1/2 - \eta)\gamma + \eta\Gamma]$$

[†] The first correction to the power law, obviously, contains terms of order γ/ω:

$$\begin{aligned} \sigma(\omega) &\approx \frac{\omega_p^2}{4\pi\omega\Gamma^{2\eta}} \frac{i^{1-2\eta}}{\omega^{1-2\eta}} \left[1 - (1-2\eta)\frac{i\gamma}{\omega}\right] \\ R_p(\omega) &\approx 1 - \frac{4\Gamma^\eta \omega^{1-\eta}}{\cos\theta\omega_p} \left[\sin\left(\frac{\eta\pi}{2}\right) + \left(\frac{1}{2} - \eta\right)\frac{\gamma}{\omega}\cos\left(\frac{\eta\pi}{2}\right)\right] \end{aligned}$$

2.4.3 The One component approach: Extended Drude Formulation

The Drude formula can be obtained from the Boltzman's transport equation with the assumption that the function that describes the departure from the equilibrium has, at zero field, an exponential decay characterized by a scattering rate $\Gamma = 1/\tau$. This is the case of metals at low temperatures and frequencies (compared to E_F) where elastic scattering from impurities and weak quasielastic scattering from phonons dominate[38]. If the non-equilibrium term in Boltzman equation is supposed to have a more general form [39], an optical conductivity characterized by a complex and frequency dependent damping term, $M(\omega)$, is obtained. Rewriting the Drude optical conductivity with $1/\tau \to M(\omega) = 1/\tau(\omega) - i\lambda(\omega)$ we obtain:

$$\sigma(\omega) = \frac{\omega_p^2}{4\pi} \frac{1}{1/\tau(\omega) - i\,\omega\, m^\star(\omega)/m} \tag{2.24}$$

where we have defined $m^\star(\omega)/m \equiv 1 + \lambda(\omega)$. Although we have referred to the Boltzman equation to obtain the previous result, it is, in fact, more general. Indeed, the same result has been obtained for the infrared conductivity in metals with strong electron-phonon coupling[40, 38]. In this context, we can identify $1/\tau(\omega)$ and $m^\star(\omega)/m$ as the frequency dependent scattering rate and the mass enhancement of electronic excitations due to many-body interactions. It is also generally believed that the resulting theory is valid in the case of the coupling of a Fermi liquid to any bosonic energy spectrum [41].

When analyzing experimental data in the extended Drude formulation, one has to be careful that the optical conductivity arises from a single component. That is, if there are two or more charge-carrier systems contributing to $\sigma_1(\omega)$, the interpretation of $1/\tau(\omega)$ and $m^\star(\omega)/m$ as the frequency dependent scattering rate and the mass enhancement of electronic excitations loses its meaning. Since this formulation corresponds to a single component, the plasma frequency, ω_p, appearing in Eq. 2.24 can be calculated from the optical conductivity using the sum rule (Eq. 2.7).

To illustrate the analysis using the extended Drude formulation, we have applied Eq. 2.24 to the optical conductivities corresponding to the models discussed in the previous subsections and given in Table 2.2. Additionally we have schematically modeled the optical response found in heavy fermion (HF) systems using Eq. 2.19 with the parameters given in Table 2.3. Notice that for comparison we have taken the spectral weight contained by the first two oscillators equal to the zero-mode of the other examples. In Fig. 2.4 we plot $1/\tau(\omega)$ and $m^\star(\omega)/m$ corresponding to these three cases. As expected, for the Drude formula, these quantities are frequency independent. The other two models produce mass enhancement at low frequencies and a frequency dependent scattering rate.

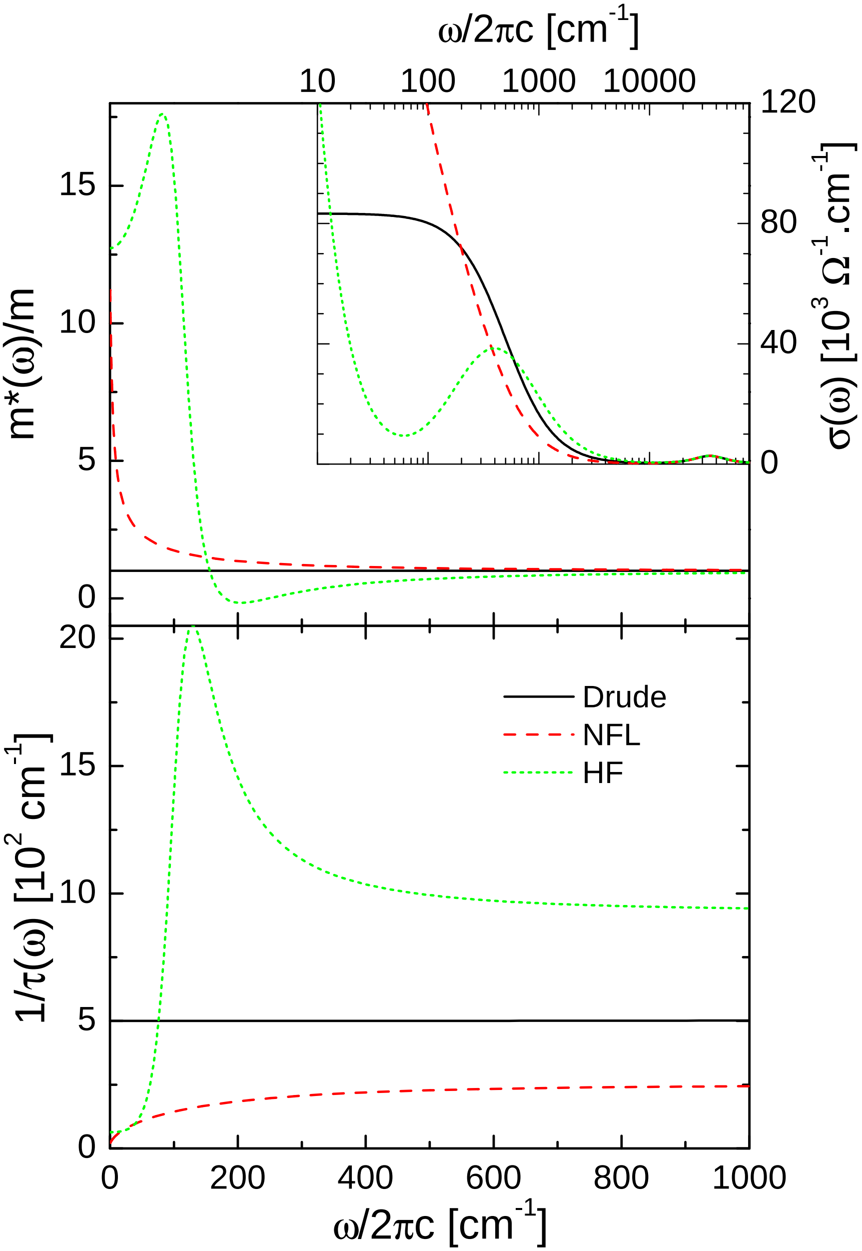

Figure 2.4: *$1/\tau(\omega)$ and $m^\star(\omega)/m$ obtained applying Eq. 2.24 to the optical conductivities corresponding to the models given in Tables 2.2 and 2.3. Upper inset: Optical conductivity for the three models.*

Table 2.3: *Parameters, in cm*$^{-1}$*, used to model the optical response of HF systems. Notice that* $\omega_{p,Drude}^2 + \omega_{p,MIR}^2 = \omega_p^2$*, where* ω_p *is the plasma frequency for the zero-mode used in Table 2.2.*

Oscillator	ω_o	ω_p	Γ
Drude	0	14000	5
MIR lorentzian	400	48000	1000
UV lorentzian	35000	70000	30000

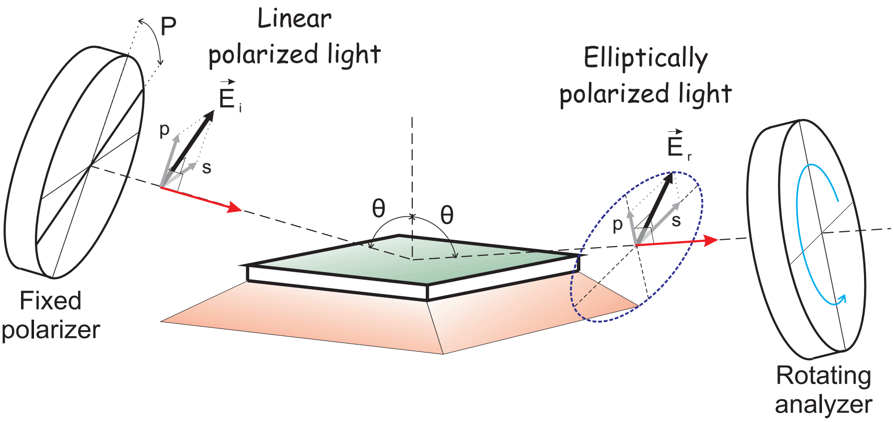

Figure 2.5: *Schematic representation of the method used for the ellipsometric measurements.*

2.5 Measuring Directly the Dielectric Function: Ellipsometry in Bulk Samples

Ellipsometry allows us to determine the ratio between the p- an s-polarized reflection coefficients, $\rho \equiv \frac{r_p}{r_s} \equiv \tan(\Psi)e^{i\Delta}$. This ratio can then be related directly with the dielectric function at least in the case of isotropic samples. From Equations 2.11 and 2.13 it can be shown that:

$$\epsilon = \sin^2\theta \left[1 + \tan^2\theta \left(\frac{1-\rho}{1+\rho}\right)\right]$$

where θ is the angle of incidence. In the case of anisotropic samples, this quantity is known as the *pseudo-dielectric function*. The determination of the dielectric function of anisotropic materials requires extra measurements, usually ellipsometry in different crystallographic planes or at different angles of incidence.

There are various ellipsometric configurations. The one we have chosen is depicted in Fig. 2.5. The principal components are a fixed polarizer displaced an angle P relative to the incidence plane and a second polarizer (called analyzer) that rotates at a frequency w. A beam of intensity I_o is directed through the polarizer. This beam is usually chopped at a frequency much less than w to facilitate its detection. After reflection, the polarization of the light changes, in general being elliptical. The rotating analyzer modulates the intensity of the beam, $I = I_o + a\cos(2wt) + b\sin(2wt)$, which can be easily measured using lock-in techniques. The ratios $\alpha = a/I_o$ and $\beta = b/I_o$ are then easily measured. It can be shown that they obey the following relations [42]:

$$\begin{aligned} \alpha &= \frac{\tan^2\Psi - \tan^2 P}{\tan^2\Psi + \tan^2 P} \\ \beta &= \frac{2\tan\Psi\cos\Delta\tan P}{\tan^2\Psi + \tan^2 P} \end{aligned}$$

Their inversion allows to determine the angles Ψ and Δ that define ρ.

In the work presented in this thesis, the ellipsometry technique was performed in the interval [6000-36000] cm^{-1}. The temperature dependences were determined using a home-made ultra-high-vacuum cryostat. Therefore, we have to take into account the change of polarization caused by the windows in the cryostat. This correction is temperature independent and can be easily determined at room temperature by performing an ellipsometric measurement with and without windows at the same angle of incidence [43]. In fact, it can be easily shown that in the presence of windows:

$$\rho_{sample+wind} = \rho_{wind} \times \rho_{sample}$$

At room temperature, ρ_{wind} is determined and, then, this value can be used at all temperatures to determine ρ_{sample}.

2.6 Reflectivity in Bulk Samples

In principle, measuring reflectivity is rather straightforward (Fig. 2.6). With a polarizer s or p polarizations are selected and, then, reflectivity corresponds to the ratio between the intensity of the reflected beam and the intensity of the incident beam. In practice, these intensities are difficult to measure and, as a common practice, a reference measurement is used. Selecting an appropriate reference is also non-trivial as small changes in replacing the sample by the reference can lead to big errors in the measured reflectivity. For the present work we have selected the following approach:

a. The intensity reflected by the sample is measured at all temperatures.

b. Gold is evaporated in-situ on the sample, at room-temperature, without translating or rotating the sample-holder.

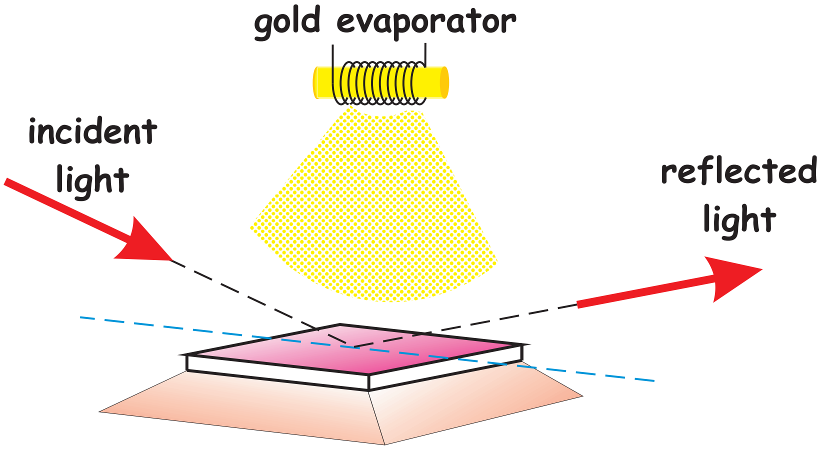

Figure 2.6: *Schematic diagram of the experimental set-up used to measure reflectivity.*

c. The intensity reflected by the gold film is measured again at all temperatures.

The sample is mounted in a home-built cryostat, the special construction of which guarantees the stable and temperature independent optical alignment of the sample. This cryostat allows to measure reflectivity in two configurations: near normal ($\theta = 11^\circ$) and grazing incidence ($\theta = 80^\circ$) reflectivity. Grazing incidence has been used to resolve the high reflectivity of metallic samples [44, 45, 46] since then it is lowered by $\cos\theta$ respect to normal incidence reflectivity (see Eq. 2.16).

2.6.1 From Reflectivity to Optical Conductivity

Let us assume for a moment that we have measured $R_p = |r_p|^2$ in the whole frequency range. To invert Eq. 2.13 and determine the dielectric function, we still need to determine the phase of the reflection coefficient, ϕ_{rp}. This could be achieved using KK relations for the logarithm of the reflection coefficient, $\ln r_p = \ln|r_p| + i\phi_{rp}$. As pointed out in §2.2, this is possible only if $\ln r_p$ has no poles in the upper half of the complex plane. The logarithm of r_p has poles for $r_p = 0$ which, from Eq. 2.13, only occurs when $\epsilon(\omega) = \tan\theta$ [47]. Using the Drude model for the dielectric function we can find that the poles are limited to the lower complex plane if

$$\tan^2\theta < \epsilon_\infty \tag{2.25}$$

This restricts the application of KK relations to a limited set of angles of incidence. Because $\epsilon_\infty = 1$, KK relations for reflectivity exist only for angles of incidence lower than $\theta_{max} = 45^\circ$.

Near normal incidence

The reflection experiments that will be discussed in the following chapters have been performed in the frequency range of [20-6000] cm^{-1}. Given the restrictions in our experimental setup, for the near normal incidence configuration we have selected $\theta = 11°$. In this case, Eq. 2.25 warrants that KK relations exist for $\ln r_p$. The problem now is to extend our measured reflectivity to a larger frequency range to be able to use KK relations and then obtain the phase of the reflection coefficient. The usual method is to obtain reasonable extrapolations outside the measured frequency range. We have used the following procedure that combines reflectivity and ellipsometry (§2.5) measurements in the same studied material [48]:

a. We fit at the same time:

   i DC conductivity (when available),

   ii reflectivity (via the Fresnel equations), and

   iii the dielectric function obtained by ellipsometry

   using a model dielectric function which is the combination of one Drude and various Lorentz oscillators (Eq. 2.19). The Drude oscillator can be replaced with Eq. 2.20.

b. From the fit, we obtain extrapolations below and above the measured range (i.e. for $\omega/2\pi c < 20$ cm^{-1}and $\omega/2\pi c > 36000$ cm^{-1}).

c. This allows to perform a Kramers-Kronig transformation using the measured reflectivity, the reflectivity obtained from ellipsometry and the extrapolations.

This procedure has the advantage that the resulting dielectric function is *locked* to the measured one.

Grazing incidence

In near normal incidence it is difficult to resolve the high reflectivity of metallic samples. One possible solution is to perform a reflection experiment at a larger angle which will reduce the reflectivity by $\cos\theta$. For example, we have chosen an angle of incidence of 80°. After obtaining extrapolations as described above, the problem we face is that there are no KK relations for grazing incidence reflectivity. An equivalent approach is to use a large number of oscillators that will fit every detail of the measured reflectivity and will still reproduce the measured dielectric function [45, 47, 50]. This is the method we have used.

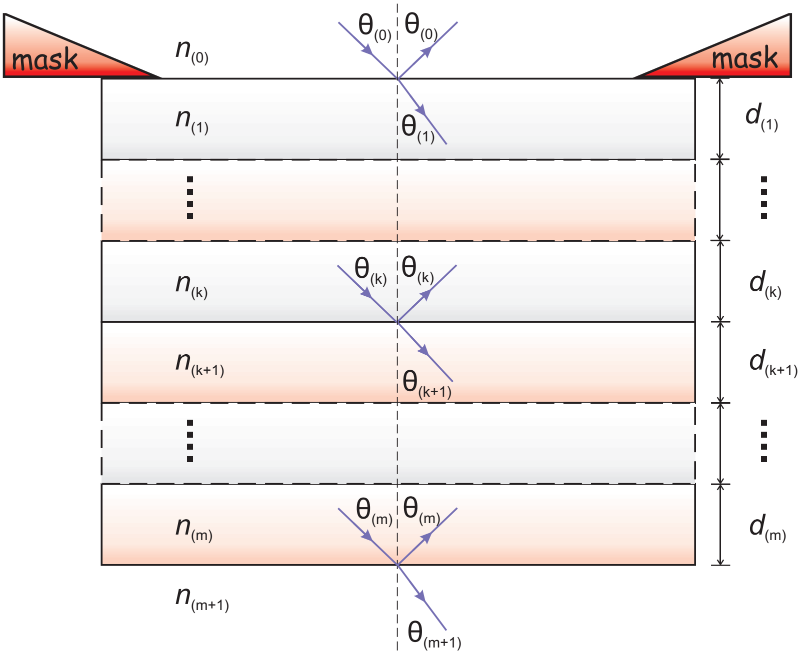

Figure 2.7: *Schematic diagram of a system composed of m different layers.*

2.7 Layered Systems

Let us considered a stack of m layers thin enough to be transparent (Fig. 2.7). Each layer is characterized by its thickness, $d_{(k)}$, and complex dielectric function, $\epsilon_{(k)} = {n_{(k)}}^2$. In this case, to determine the the reflectivity and transmission of the system (i.e. the ratios of the incident beam to the reflected and transmitted beams), we have to take into account the different contributions coming from multiple reflections (and their transmissions) in the different interfaces.

The easiest way to mathematically describe the reflection and transmission of such a system [49] is to define the following matrix:

$$M_{(k)} = \begin{pmatrix} \mathrm{e}^{-i\delta_{(k-1)}} & r_{(k)}\mathrm{e}^{-i\delta_{(k-1)}} \\ r_{(k)}\mathrm{e}^{i\delta_{(k-1)}} & \mathrm{e}^{i\delta_{(k-1)}} \end{pmatrix} \tag{2.26}$$

where $r_{(k)}$ represents the complex reflection coefficient between the $(k-1)$-th and k-th layers, and $\delta_{(k)} \equiv 2\pi\overline{\nu}n_{(k)}d_{(k)}\cos\theta_{(k)}$ is the phase change of the beam when traveling through the k-th layer. The coefficients $r_{(k)}$ are given by the Fresnel relations (Equations 2.11 or 2.13). We have omitted the index s and p in Eq. 2.26 because these results are valid for both polarizations. Further, we define the matrix M as the multiplication of all matrices $M_{(k)}$, i.e. $M = \prod_{k=1}^{m+1} M_{(k)}$. With these definitions, the *total* reflection and transmission coefficients in a layered system are given by:

$$r = \frac{M_{21}}{M_{11}} \tag{2.27}$$

$$t = \frac{\prod_{k=1}^{m+1} t_{(k)}}{M_{11}} \tag{2.28}$$

with $t_{(k)}$ the transmission coefficient between the $(k-1)$-th and k-th layers, and M_{pq} the matrix element situated at row p and column q.

2.7.1 Reflection and Transmission

The absolute values of reflectivity and transmission for a multilayer system were determined at (near) normal incidence in the range [1000-6000] cm^{-1}. The following procedure was used at room temperature:

a. The sample is placed behind a mask (see Fig. 2.7). This limits the reflected and transmitted light that reaches the detector to only the one that comes from the sample.

b. The sample is replaced by the reference. In the case of reflection it is a golden mirror while in transmission it is the bare mask.

c. The corresponding ratios give $R = rr^{\star}$ and $T = tt^{\star}$.

We measured only the temperature dependence of the intensity reflected and transmitted by the sample.

One-layer system: substrate

For a one-layer system, it is enough to know its reflectivity and transmission to determine its optical properties by inverting the square of the absolute values of Equations 2.27 and 2.28. The inversion can be done numerically. An equivalent approach is similar to the one we used to determine the dielectric function from grazing incidence reflectivity (§2.6.1). First, we fit the experimental data using a limited number of Drude-Lorentz oscillators. After a reasonable fit, on the top of it, a large number of oscillators is added in such a way that it reproduces all the details of the measured spectra.

As an example of the described procedure, we show the results for a SrTiO$_3$ substrate ($d_{(1)} = 525\mu$m) in Fig. 2.8. The data does not show interference as a result of the substrate being slightly wedged after the polishing of the back side. The wedging of the substrate has also been modeled assuming a disperssion in the thickness of the sample [50]. In the same Figure, we also present the reflectivity obtained before polishing of the back side and the reflectivity obtained from the dielectric function assuming a bulk sample.

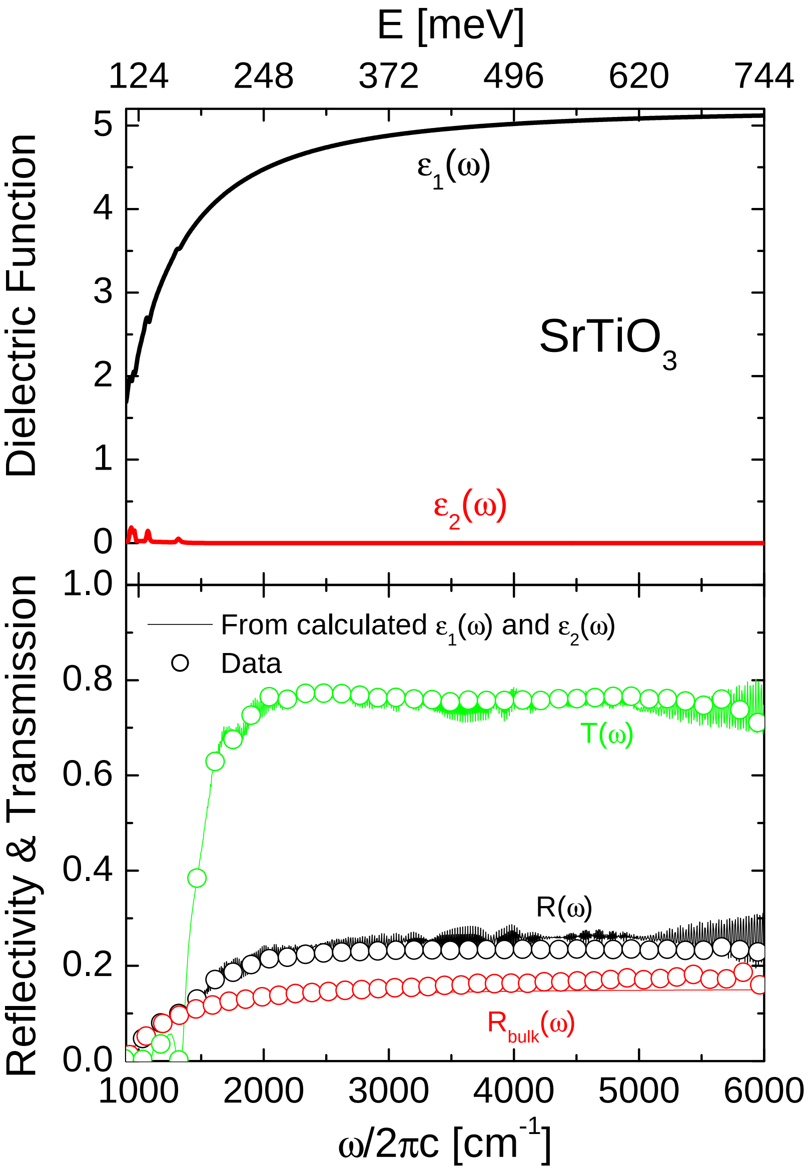

Figure 2.8: *Results for a $SrTiO_3$ substrate. Upper panel: Dielectric function obtained from inverting Equations 2.27 and 2.28 using reflectivity and transmission. Lower panel: Reflectivity and transmission data (circles), $R(\omega)$ and $T(\omega)$ obtained from the calculated dielectric function (lines). We also show the measured and calculated reflectivity of the same substrate before the back side was polished [$R_{bulk}(\omega)$].*

Two layers system: film+substrate

Determining the optical properties of a film deposited in a substrate requires the knowledge of the properties of the substrate. With that information, if reflectivity and transmission of the system is measured, we can invert the corresponding Equations 2.27 and 2.28. If only one of the two is known, an analysis *à la* Kramers-Kronig can be made if the dielectric function in another frequency range has been previously determined. This information can be obtained by ellipsometry.

2.7.2 Ellipsometry

To determine the dielectric function from ellipsometric measurements we can follow a similar approach as described in the previous subsection. We only have to remember that from ellipsometry we can obtain the complex ratio between the reflection coefficients, $\frac{r_s}{r_p}$. Then, for a one-layer system, a single ellipsometric measurement will be necessary to invert the ratio of the reflection coefficients (Equations 2.27). The same is valid for a two-layer system if the optical properties of the substrate are known.

Chapter 3

Silicides I: Non-Drude Optical Conductivity in MnSi

The optical properties of the weakly helimagnetic metal MnSi have been determined in the photon energy range from 2 meV to 4.5 eV using the combination of grazing incidence reflectance at 80° (2 meV to 0.8 eV) and ellipsometry (0.8 to 4.5 eV). As the sample is cooled below 100 K the effective mass develops a strong frequency dependence at low frequencies, while the scattering rate develops a sub linear frequency dependence. The complex optical conductivity can be described by the phenomenological relation $\sigma(\omega, T) \propto (\gamma(T) + i\omega)^{-0.5}$.

3.1 Introduction

The weakly helimagnetic metal MnSi ($T_C = 29.5$ K) has been the subject of intensive studies during the last 40 years. In the helimagnetic phase the resistivity has a T^2 dependence, which has been explained as resulting from a coupling of the charge carriers to spin fluctuations[4]. Recently, interest has shifted to the quantum phase transition [51] at a critical pressure of 14.6 kbar where the Curie temperature becomes zero. The temperature dependence of the resistivity outside the magnetically ordered region, at high pressures, has been found to be proportional to $T^{3/2}$ in temperature range far larger than that predicted by the so-called nearly ferromagnetic Fermi-liquid theory, an extension of the Fermi-liquid picture[51] (see Fig. 3.1). This fact has suggested the non-Fermi liquid nature of MnSi in the normal state [51]. Despite these efforts in understanding the physics behind MnSi, few attempts have been made to determine and understand its optical properties. Measurements below T_C of the far infrared normal incidence

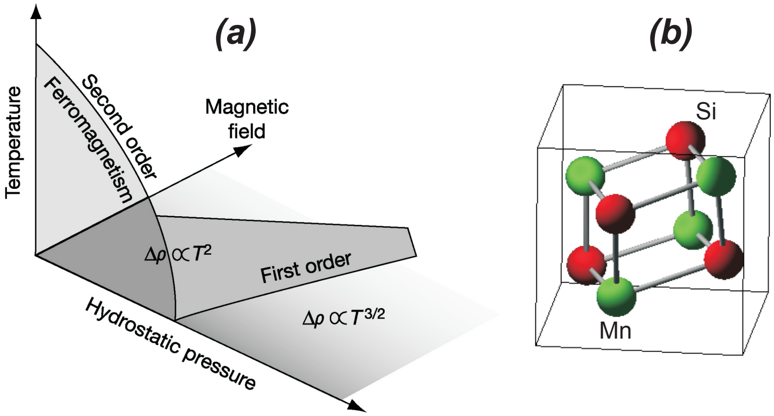

Figure 3.1: *(a)Schematic phase diagram of MnSi under pressure, magnetic field and temperature (from Ref. [53]). (b) Crystal structure.*

reflectivity indicated a remarkable departure from the Hagen-Rubens law, usually observed in metals[52]. However, the high value of the reflection coefficient (close to the 100 % line) prevented a detailed analysis of the frequency dependent optical conductivity in this range. In this work we overcome this hurdle by using p-polarized light at a grazing angle of incidence of 80°, for which the reflection coefficient drops well below the 100 % line. We show that the frequency dependent scattering rate and the effective mass deviate from the the behavior expected for Fermi liquids which can be understood from the fact that the optical conductivity is best described with an expression that departs from the usual Drude model.

3.2 DC Resistivity

Single crystals of MnSi were grown using the traveling floating zone technique[52, 54]. The temperature dependence of the resistivity of one of the crystals is shown in Fig. 3.2. Fitting the resistivity to

$$\rho(T) = \rho(0) + AT^{\mu}$$

in the temperature interval 4K to 23K, we obtain $\rho(0) = 1.85\ \mu\Omega$ cm, $A = 0.021\ \mu\Omega$ cm K^{-2}, and $\mu = 2.1$ (upper inset of Fig. 3.2). The resistivity increases more rapidly in the region between 23 K and the phase transition. For $T > 30$K the resistivity fits to

$$\frac{1}{\rho_p(T)} = \frac{1}{\rho_\infty} + \frac{1}{\rho' T}$$

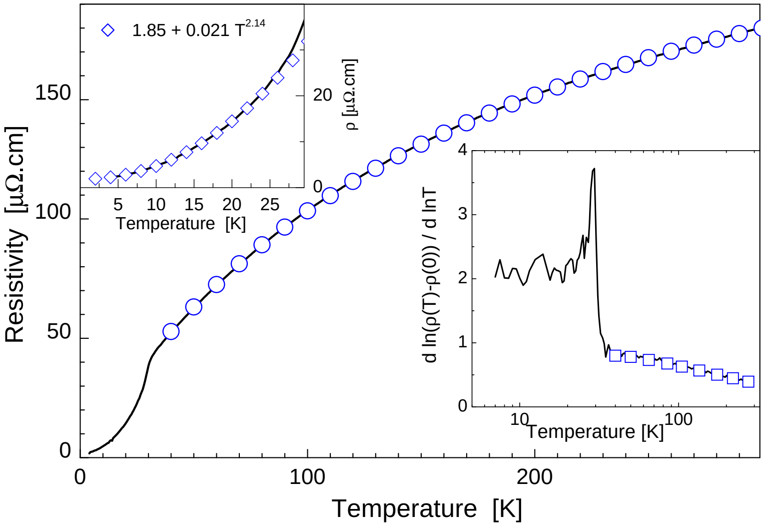

Figure 3.2: *DC resistivity as a function of temperature (solid curve). The open circles represent* $\rho_p(T) = (1/\rho_\infty + 1/(AT))^{-1}$ *with* $\rho_\infty = 286\ \mu\Omega$ *cm and* $A = 1.62\ \mu\Omega$ *cm* K^{-1}*. Top left inset: DC resistivity (solid curve) below 30 K and fit to* $\rho_F(T) = \rho(0) + AT^\mu$ *(open diamonds). Lower right inset: Temperature dependence,* $\mu(T)$*, of the exponent in* $\rho(T) = \rho(0) + AT^\mu$ *(solid curve). The open squares represent* $d\ln\rho_p/d\ln T$*.*

with $\rho_\infty = 286\ \mu\Omega$ cm and $\rho' = 1.62\ \mu\Omega$ cm K^{-1}. The remarkable accuracy of this parallel resistor formula [55] is further confirmed by the logarithmic derivative shown in the inset of Fig. 3.2. The tendency of the resistivity toward saturation at a value ρ_∞ for $T \to \infty$ is in agreement with Calandra and Gunnarsson's result[56] that the resistivity saturates when the mean free path $l = 0.5n^{1/3}d$ (roughly the Ioffe-Regel limit), where n is the density of the electrons and d is lattice parameter. Also this indicates that, if the temperature saturation would be absent, the resistivity would be proportional to T with a very high accuracy. These observations stand in stark contrast to the $T^{5/3}$ temperature dependence predicted from the model of spin-fluctuations in itinerant electron magnetism[4].

3.3 Optical Spectroscopy

3.3.1 Experiment and Results

Grazing incidence reflectivity was measured in the range 20 to 6000 cm^{-1} using a Bruker 113v FT-IR spectrometer (Fig. 3.3a and 3.3b). The temperature dependence was measured using a home-built cryostat, the special construction of

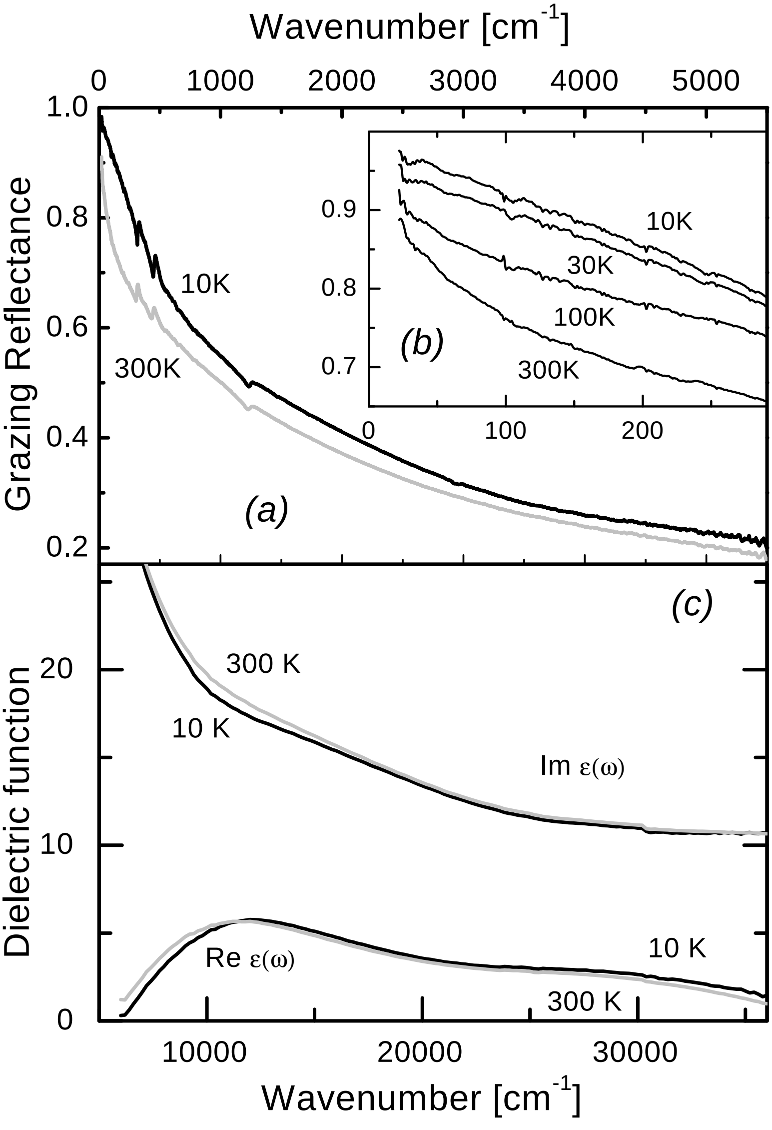

Figure 3.3: *a) Grazing reflectivity at 10 and 300 K. b) Expanded view of the reflectivity below 300 cm^{-1}. c) Real and imaginary part of the dielectric function in the visible part of the spectrum measured with spectroscopic ellipsometry.*

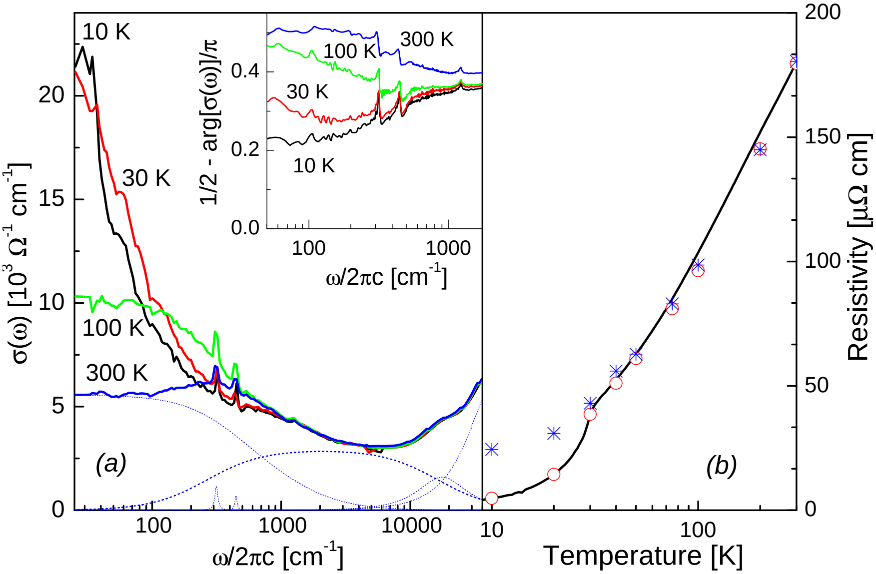

Figure 3.4: *a) Optical conductivity at four different temperatures. b) Measured DC resistivity, and DC resistivity obtained by extrapolating the experimental* $\sigma(\omega)$ *using a Drude-Lorentz fit (stars) and using Eq. 2.20 (open circles). Inset: Phase of the complex optical conductivity.*

which guarantees the stable and temperature independent optical alignment of the sample. The intensities were calibrated against a gold reference film evaporated *in situ* without repositioning or rotating the sample-holder. In the range 20 to 100 cm^{-1} we measured the temperature dependence of the grazing reflectivity with 0.5 K intervals below 50 K and 2 K intervals above 50 K. The complex dielectric function in the range 6000 to 36000 cm^{-1} was measured with a commercial (Woollam VASE32) ellipsometric spectrometer for the same set of temperatures as the grazing reflectivities using an ultra high vacuum cryostat (Fig. 3.3c). The complex dielectric function $\epsilon(\omega) = \epsilon'(\omega) + i(4\pi/\omega)\sigma_1(\omega)$ was calculated from the complete data set (grazing infrared reflectance and visible ellipsometry) using the *à la* Kramers-Kronig procedure described in §2.6. Below 20 cm^{-1} the reflectivity data were extrapolated to fit the experimentally measured DC conductivities. The optical conductivity is shown for some temperatures in Fig. 3.4.

3.3.2 Extended Drude Analysis

The first remarkable feature in the spectra is the similarity of the optical conductivity to the response of heavy fermion systems[57]. In those materials, $\sigma_1(\omega)$

has almost no temperature dependence down to a frequency of $\sim$10 cm^{-1} and, below this frequency, a narrow mode centered at zero frequency is formed [57]. Similar behavior has also been noticed for α-cerium[45] in the mid-infrared frequency range. Following a common procedure in the study of the electrodynamic response of heavy fermion systems, we have calculated $1/\tau(\omega)$ and $m^\star(\omega)/m$ from the optical conductivity using the extended Drude-model [39] (Eq. 2.24) adopting the value 18700 cm^{-1} for the plasma frequency, motivated by the least square fits which we will discuss below. Fig. 3.5a indicates a significant mass renormalization at low frequencies which, at the lowest measured temperatures, shows no indication of reaching a frequency independent value. Previous de Haas-van Alphen experiments (at $T = 0.35$ K) [58] provided an *average* enhancement of 4.5 times the cyclotron mass, although values as high as 14 were observed for some of the orbits. This average value was found to be compatible with the enhancement of the linear coefficient of the heat capacity, γ/γ_o =5.2, calculated from specific heat data of Ref. [59]. In comparison, our data show at 10 K and at the lowest measured frequency an enhancement of 4, and an enhancement of 17 when we extrapolate the data to $\omega = 0$.

The second remarkable feature is the behavior of $1/\tau(\omega)$ (Fig. 3.5b). At high temperatures this quantity becomes frequency independent, as expected for a Drude peak. Already at 100 K, $1/\tau(\omega)$ is no longer a constant. Approaching the phase transition $1/\tau(\omega)$ becomes strongly frequency dependent between 30 and 300 cm^{-1} and it follows approximately a linear frequency dependence in this frequency range. In contrast, other correlated systems, such as heavy fermions [57, 45] and perovskite titanates [60], show a frequency-dependent scattering rate with an ω^2 dependence at low frequencies. Indeed the theory of Fermi liquids [61] predicts

$$1/\tau(\omega, T) = 1/\tau_o + a(\hbar\omega)^2 + b(k_B T)^2 \tag{3.1}$$

with $b/a = \pi^2$. The same expression was obtained by Millis and Lee considering the Anderson lattice model [17], and qualitatively similar behavior has been calculated by Riseborough in the context of spin-fluctuations (with $b/a = 4\pi^2$)[62]. The frequency dependences of $1/\tau(\omega)$ corresponding to these theories are plotted in the inset of the lower panel of Fig. 3.5 for 10 K. There is a mismatch with the experimental $1/\tau(\omega)$, both in absolute value and the observed trend, which is outside the experimental error bars. However it can not be excluded, that at an even lower frequency the experimental $1/\tau(\omega)$ would cross over to a ω^2-dependence.

3.3.3 Deviation from the Drude formulation

Above, we have pointed out various striking results in the optical response of MnSi. In order to understand their nature, let us take a closer look at the low frequency data. From 300 to 75 K, $1 - R_p(\omega)$ follows a $\omega^{1/2}$ behavior (see Fig.

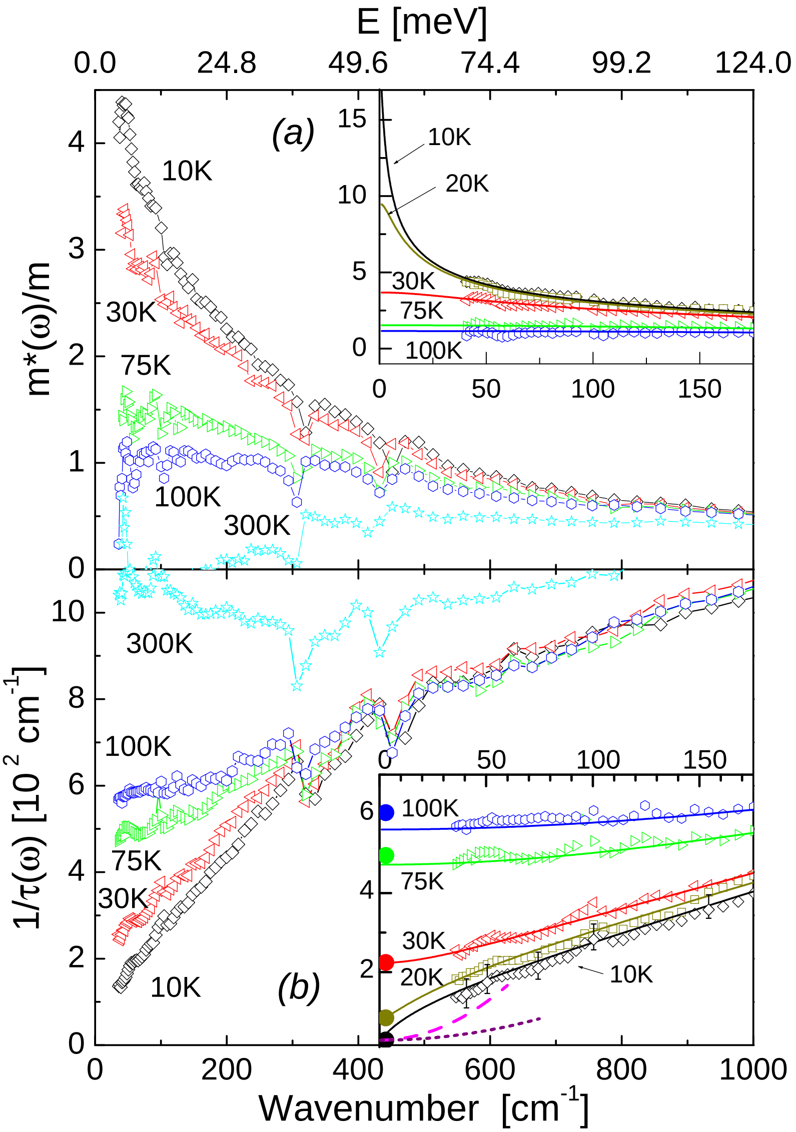

Figure 3.5: *a) Effective mass and (b) frequency-dependent-scattering rate in MnSi as obtained from $\sigma_1(\omega)$ at different temperatures. Insets: Same quantities below 200 cm^{-1}. Symbols represent the experimental data and thick lines the calculation from the non-Drude fit described in the text. The solid points at the left show $\rho_{DC}\omega_p^2/(4\pi)$. The inset of the lower panel shows also the expected frequency dependence for the Fermi liquid theory (dashed line) and spin fluctuations (dotted line) calculated from Eq. 3.1.*

3.6a). As discussed in §2.4, this can be easily understood from Eq. 2.16 and which is reproduced here:

$$R_p = 1 - \frac{2\omega^{1/2}}{\cos\theta}\mathrm{R}e\left[\frac{1}{\sqrt{i\pi\sigma(\omega)}}\right]$$

In the case that σ_1 is constant and σ_2 goes to zero, this expression reduces to the well known Hagen-Rubens law. In the Drude picture this corresponds to the frequency range where the scattering rate is larger than ω. In contrast, below 75 K our measured R_p does not follow a $\omega^{1/2}$ behavior. Combining the Drude model with the Fresnel equations for reflectivity, a plateau in the reflectivity is expected for *intermediate* frequencies (frequencies larger than the scattering rate but much lower than the plasma frequency). To check this more closely we measured $R_p(\omega)$ below 100 cm^{-1} in a finer temperature mesh. Our results show no sign of a plateau, instead $1 - R_p(\omega)$ evolves gradually to a linear frequency dependence when T is lowered. We can also see this in Fig. 3.6 where we present the result of fitting the grazing reflectivity to a general expression of the form:

$$R_p = 1 - \frac{C}{\cos\theta}\omega^{1-\beta} \tag{3.2}$$

At high temperatures we obtain $\beta \approx 0.5$ which corresponds to the HR limit. As the temperature is lowered, after a small increase, this exponent decreases and reaches the value of $\beta \approx 0.28$ at the lowest temperature. This effect is not an artifact of the grazing incidence technique since a fitting to reflectivity at near normal incidence give the same results. Although it is tempting to attribute the sudden drop of C and β for $T < 40$ K to the magnetic phase transition, we will see below that this is not the case. This drop is only an artifact due to fitting the reflectivity to a power law formula in a region which is not adequate.

Given the behaviour just described, we can then conclude that either the peak centered at zero frequency departs from the Drude picture or other modes appear at low temperatures and at low frequencies. To distinguish between these alternatives we have fitted, simultaneously, the measured reflectivity, ellipsometry and resistivity with two models. First we modelled the data with a Drude peak and a set of oscillators. In this case, the fit fails to reproduce the measured DC resistivities at low temperatures (stars in Fig. 3.4b). On the other hand, if we give more fitting weight to ρ_{DC}, the result is a poor fit of R_p at low frequencies[*]. Indeed, the infrared properties together with the DC resistivity can be summarized in an economical way (*i.e.* requiring a minimal set of adjustable parameters) when we replace the Drude formula with Eq. 2.20 [36]:

$$\sigma(\omega) = \frac{\omega_p^2}{4\pi}\frac{i}{(\omega + i\gamma)^{1-2\eta}(\omega + i\Gamma)^{2\eta}}$$

---

[*] It is evident that in this case, the fit can be improved if more low frequency oscillators are added, but using Eq. 2.20 requires less number of parameters

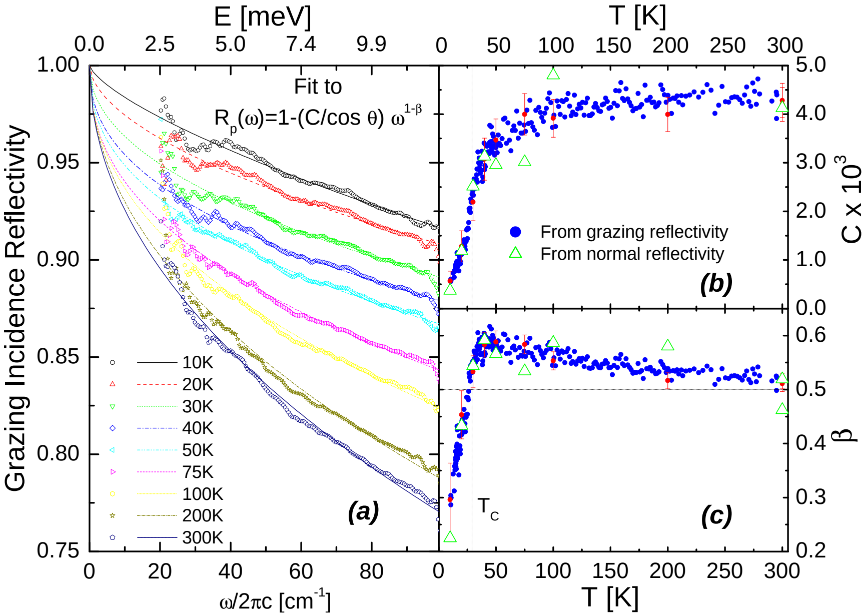

Figure 3.6: *a) Low frequency grazing incidence reflectivity (symbols) and fit to Eq. 3.2 (lines). b) and c) Temperature dependence of the fitting parameters obtained from grazing incidence and near normal incidence experiments. The depicted error bars were obtained by displacing (up and down)* $R_p(\omega)$ *by 0.5%.*

As discussed in §2.4, this formulation, for $\gamma \ll \omega \ll \Gamma$, corresponds to the expression derived by P. W. Anderson in the context of the optical conductivity of the cuprate high T_c superconductors, $\sigma(\omega) \propto (i\omega)^{2\eta-1}$ [36, 35]. Moreover, this formula, in the case $\Gamma \gg \omega$, has been shown to describe the optical conductivity of $SrRuO_3$, below 40 K, in the range [6-2400] cm^{-1} with $\eta = 0.3$ [63].[†] For $SrRuO_3$ this behavior has been justified as arising from the coupling of electrons to orbital degrees of freedom[64], and in the context of the discrete filamentary model of charge transport[65].

Our new fit, non-Drude plus Lorentz oscillators (whose individual components at 300 K are displayed in Fig. 3.4a), gives the same overall result at high temperatures (T >75 K) as the Drude fit. However, at low temperatures, the non-Drude equation gives a better fit at low frequencies and, what is more important, reproduces ρ_{DC} at all temperatures (open symbols in Fig. 3.4b). Therefore, we conclude that the low frequency optical response of MnSi is best described by Eq. 2.20. From the fit we can extrapolate the optical properties to lower frequencies (insets of Fig. 3.5). The extrapolation shows that at 10 K, for $\omega \rightarrow 0$,

---

[†] The exponent η in this thesis is related to the exponent α of Dodge *et al.* by $\alpha = 1 - 2\eta$.

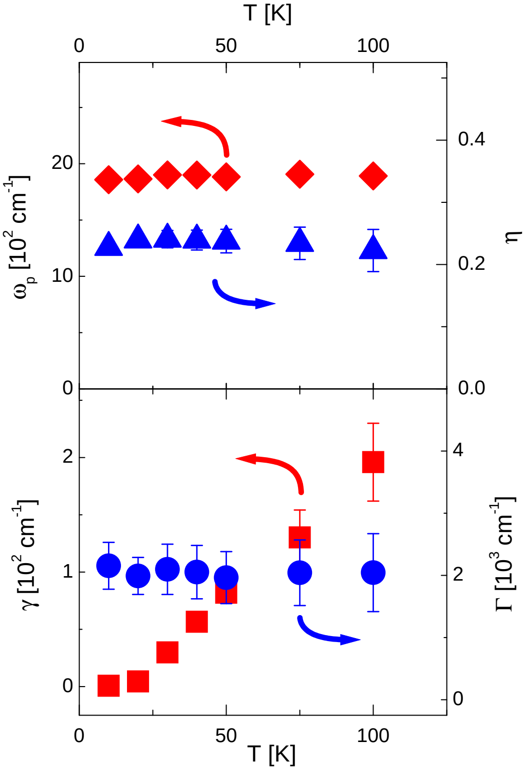

Figure 3.7: *Temperature dependence of the parameters obtained from the fit of Eq. 2.20 to the experimental data.*

$m^\star(\omega)/m = 17$, with a gradual decay as a function of increasing frequency. Similarly, $1/\tau(\omega)$ is approximately proportional to ω in the frequency range below 300 cm^{-1}. Above T_C, it has a weak ω^2 frequency dependence.

Now let us analyze the parameters of the fit to Eq. 2.20 which are summarized in Fig. 3.7 (the error bars represent the interval of confidence calculated for a variation of 1% of χ^2). Within the error bars, the parameters ω_p, Γ and η are temperature independent, which contrasts with the strong decrease of γ with decreasing temperature. This temperature dependence allows us to make two independent checks of the validity of using Eq. 2.20 to describe the optical properties of MnSi. According to this fit, at high temperatures, the parameters γ and Γ are of the same order. Therefore, at low frequencies the condition $\omega \ll \gamma < \Gamma$ holds, which corresponds to the region **I** described in §2.4.2 and where the Hagens-Rubens limit is reached. Accordingly, at high temperatures the fit of the low frequency reflectivity, Fig. 3.6, gives the expected square root dependence.

On the contrary, in the low temperature limit at low frequencies, the following inequality holds $\gamma \ll \omega \ll \Gamma$. This range correspond to region **II** in §2.4.2. In this region, $R_p(\omega)$ also follows a power law behaviour given by Eq. 2.23. This allows us to perform the first check. Namely, in this limit, the parameters β and C of Eq. 3.2 should correspond to $\eta \approx 0.23$ and $4\Gamma^{\eta}\sin(\eta\pi/2)/\omega_p \approx 4.5 \times 10^3$, respectively. From Fig. 3.6 we see that the agreement is excellent. At intermediate temperatures, $R_p(\omega)$ does not follow a power law and the sudden drops of parameters C and β (Fig. 3.6) correspond to a change from one to the other limits just described, thus not corresponding to the entrance to the magnetic state. The second independent check, also at low temperatures and frequencies, is to verify if Eq. 2.22 holds and a plateau in the phase of the optical conductivity is seen (see §2.4.2). We have plotted the quantity $1/2 - \arg[\sigma(\omega)]/\pi$ in the lower inset of Fig. 3.4 from where we see the appearance of a low frequency plateau with the value 0.22. The agreement with the value of η obtained from the fit to Eq. 2.20 is outstanding.

From Eq. 2.20 we can easily see that $\rho_{DC} = 4\pi\omega_p^{-2}\Gamma^{2\eta}\gamma^{1-2\eta}$, but since ω_p, Γ and η are temperature independent, $\rho_{DC}(T) \propto \gamma(T)^{1-2\eta}$. For our sample, using the values of Fig. 3.4, we obtain $\rho_{DC} = 6.02\,\gamma^{0.54}$ [$\mu\Omega$ cm]. Recently, Dodge *et al.*[63] have emphasized a similar non-linear relationship between the DC resistivity and the parameter γ in the case of the weak itinerant ferromagnet $SrRuO_3$. The conclusions for $SrRuO_3$ have been questioned recently by Capogna *et al.*[66], who argued that the true temperature dependence of the optical properties may have been masked by the large residual resistivity of the sample used in Ref. [63]. In the present work this problem is absent due to the low residual resistivity of single crystalline MnSi. In fact, we can confirm this non-linear relation *independently* by fitting the low frequency $R_p(\omega)$ (at all the measured temperatures) to Eq. 2.20 using the known values of ω_p, Γ and η. The values obtained for γ are displayed in Fig. 3.8. The inset shows $\gamma^{0.54}$ and $\rho_{DC}/6.02$. We can see that the model represented by Eq. 2.20 describes the measured data (reflectivity and resistivity) down to approximately 20 K.

At low frequencies, deviations from the Drude formula of the optical conductivity have been seen accompanied by deviations from T^2 in ρ_{DC} (for example YBCO [67] and $CaRuO_3$ [68]). Therefore, a departure from Drude behavior has been usually considered as evidence against Fermi-liquid behavior. Here, for MnSi, we are confronted with an atypical case. The resistivity has a quadratic temperature dependence, but the optical conductivity is better described by Eq. 2.20 with $\eta \approx 0.23$, a clear departure from the Drude formulation. Moreover, instead of an ω^2-type frequency dependent scattering rate, which is usually observed in strongly interacting Fermi-liquids [57, 45], here $1/\tau(\omega)$ has a sublinear frequency dependence. Although Eq. 2.20 summarizes in a compact way the low frequency optical response, differing in a fundamental way from conventional Drude behavior, its microscopic origin is as yet not fully understood.

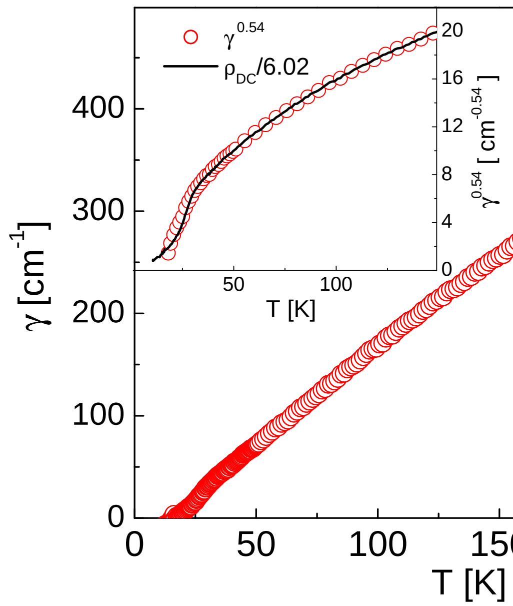

Figure 3.8: *Temperature dependence of γ (see text). Inset: Temperature dependence of $\gamma^{0.54}$ (circles) and of $\rho_{DC}\omega_p^2/(4\pi\Gamma^{2\eta})$ (solid line).*

3.4 Conclusions

For frequencies below 300 cm^{-1} and for $T < 100$ K the situation can be summarized as follows: (i) m^*/m decreases from 17 to 1 as temperature and frequency are increased. (ii) Phenomenologically the DC conductivity and the optical conductivity follow $\sigma \propto (\gamma(T) + i\omega)^{-0.5}$. In this formulation $\gamma(T) \propto T^4$ below T_C, whereas above T$_c$ the temperature temperature dependence is approximately linear. (iii) For $T > T_C$ the scattering rate $1/\tau(\omega, T)$ is proportional to T and ω^2 in contradiction with the theory of weak itinerant ferromagnetism.(iv) For $T < T_C$ the scattering rate is proportional to T^2 and ω. Given the frequency range for this type of measurements, we can not exclude the possibility, that for frequencies below 30cm^{-1} the scattering rate crosses over to the Fermi-liquid result $1/\tau \propto \pi^2T^2 + \omega^2$. However, it should be noted that if it can be confirmed that Eq. 2.20 describes the optical conductivity down to frequencies $\omega \to 0$, this crossover will not occur.

Chapter 4

Silicides II: Transfer of Spectral Weight

The optical properties of $Fe_{1-x}Co_xSi$ (x=0, 0.1, 0.2, 0.3) have been determined in the photon energy range from 2 meV to 4.5 eV using the combination of normal incidence reflectance (2 meV to 0.8 eV) and ellipsometry (0.8 to 4.5 eV). The experimental results permit us to settle a long standing controversy regarding the recovery of spectral weight. It is shown that the spectral weight is not recovered in the entire measured range, thus favoring models that include strong correlations.

4.1 Introduction

Among the transition metal silicides, three of them have particularly attracted the attention of the scientific community for more than five decades. These are MnSi, FeSi and CoSi. All of them crystallize in the same cubic structure, B20, whose main property is the lack of strict space-inversion symmetry. In MnSi, this leads to the helical ordering in its magnetic phase. The Curie temperature of this material is 30 K at ambient pressure but it can be decreased by the application of hydrostatic pressure and eventually becomes zero at $p_c = 14.6$ kbar [53, 51, 69]. MnSi is one of the so-called weak itinerant electron ferromagnets since its saturation magnetic moment ($\mu_s \approx 0.4\ \mu_B$/F.U.)[59] is smaller than the one obtained in the paramagnetic phase just above T_C ($\mu_C \approx 2.5\ \mu_B$/F.U.)[70] where its magnetic susceptibility follows a Curie-Weiss law (for a review on weak ferromagnetism see Ref. [71]). On the other hand, FeSi is paramagnetic down to at least 0.04 K [72] and CoSi is diamagnetic with a temperature independent susceptibility [73]. The solid solutions between them, $Fe_{1-x}Co_xSi$, also crystallize in the B20 structure with the metal sites being occupied randomly by Fe and Co atoms. However, in contrast to their parent compounds, they show helimagmetism[74] with low Curie temperatures in the concentration range $0.05 \leq x \leq 0.8$ (Fig. 4.1). The compo-

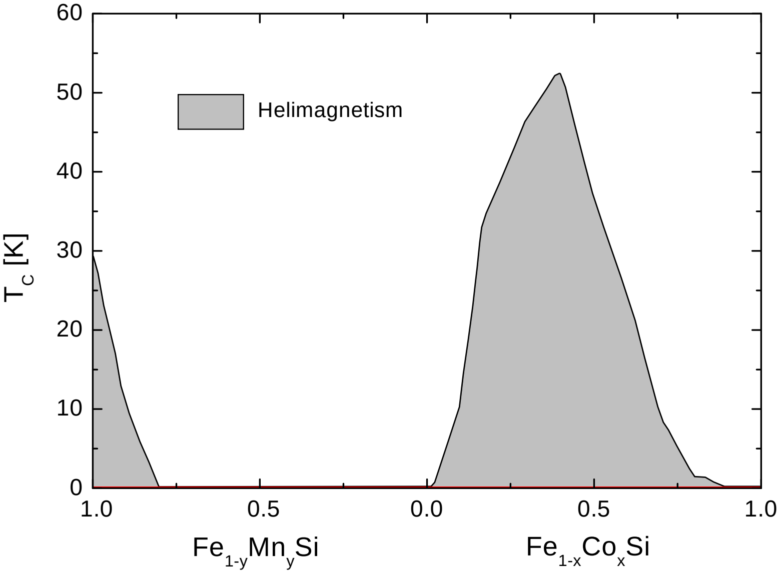

Figure 4.1: *Phase diagram of* $Fe_{1-y}Mn_ySi$ *and* $Fe_{1-x}Co_xSi$ *(adapted from Ref. [7]).*

sitions exhibiting magnetism follow also a Curie-Weiss law[75] in different ranges above T_c. Moreover, in these materials $\mu_C/\mu_s > 3$, which also indicates weak ferromagnetism [75]. At variance with MnSi and magnetic $Fe_{1-x}Co_xSi$, weak ferromagnetism appears usually in compounds whose individual components do not show magnetism in its elemental form, e.g. Sc_3In and $ZrZn_2$. These kind of compounds are also expected to show superconductivity, effect that has been indeed seen in $ZrZn_2$ [76] but not found in MnSi perhaps due to the lack of inversion symmetry center of its crystal structure [51]. Recently, in MnSi, a novel state of matter has been found for pressures larger p_c where a short range chiral magnetism co-exists with a conducting fluid that shows a non-Fermi liquid resistivity which is proportional to $T^{3/2}$. [53, 51, 69]

Since in weak ferromagnet compounds $\mu_C > \mu_s$, it is argued that local moments cannot explain the magnetism in these materials and an itinerant picture should be adopted. The Stoner model (*i.e.* the application of the Hartree-Fock method to the Hubbard model) is not enough to explain the thermodynamical properties of itinerant ferromagnets and various authors stressed the importance of including spin fluctuations (SF) for a correct description. Both, thermal[4] and zero point (quantum)[77] fluctuations have been included. This theory has been relatively successful in describing various aspects of weak magnetism. It explains, for example, the magnetization curves and the T^2-dependence of the DC resistivity, ρ, below T_C [4]. However, various authors have expressed their concerns with respect to this theory [78, 79]. Hirsch[78] has pointed out that the average square local moment (i.e. the amplitude of the thermal spin fluctuations) has not a strong temperature dependence as predicted in the spin fluctuation theory. Furthermore, Ohkawa [79] has shown that the chemical potential located at a sharp peak of the density of states, although favoring magnetism, is detrimental for the Curie-Weiss law in the SF theory. A peak in the density of states indeed occurs in Sc_3In [80], $ZrZn_2$ [81] and MnSi [82], for example. Experimentally, deviations from the predictions of the SF theory have been found in materials that are traditionally considered as described by this theory. In the case of MnSi at ambient pressure, its DC resistivity below T_C follows a T^2-law [46, 53, 51, 69] but above T_C does not follow the $T^{5/3}$-dependence [46] expected in the SF theory and seen in other weak ferromagnets[4]. We can also mention the case of magnetic $Fe_{1-x}Co_xSi$ which shows positive magnetoresistance [7] when the SF theory predicts a negative one.

The SF theory has also been applied to describe the properties of FeSi [4, 84, 83]. One of the main results is that this theory has reproduced qualitatively the magnetic susceptibility of FeSi at high temperatures. However, optical measurements have shown that FeSi develops a gap of approximately 700 cm^{-1} (87 meV) below 200 K, which cannot be explained by band theory solely. In this respect, it has been also suggested that the temperature dependence of the gap can be explained if thermal disorder is taken into account [85]. The thermal disorder is introduced via random displacements of the atoms in the unit cell which are then related to temperature. To reproduce the experimental results, an average square displacement of 8×10^{-3} Å^2 (at 300 K) is introduced, which is more than twice the thermal displacement factors found experimentally. At that temperature the maximum mean square displacement is $\sim 3.5 \times 10^{-3}$ Å^2 for Si perpendicular to the [111] direction and the minimum is $\sim 2 \times 10^{-3}$ Å^2 also for Si parallel to the [111] direction. [86]

In contrast to the itinerant theories, Aeppli and Fisk [87] have pointed out the similarity between the properties of this material and the Ce-based Kondo insulators, stressing the importance of strong correlations to describe FeSi. This point of view has been corroborated with the observation that the spectral weight of the optical conductivity, $\sigma_1(\omega)$, lost below the gap is not recovered in a region just above the gap as it occurs in conventional semiconductors [88]. Accordingly, various calculations in the large U limit have tried to explain this observation [32, 89]. However, the above mentioned experimental result is matter of controversy that has not yet been settled [90]. The main argument is that an error of 1% in the measured reflectivity is enough to explain the apparent lack of recovery of spectral weight [91]. Therefore, the objective of this chapter is to settle this controversy that has lasted already for ten years. For that purpose we have complemented reflectivity experiments in the far infrared with ellipsometry in the visible range and used these data to perform a Kramers-Kronig analysis. The advantage is that this procedure anchors the phase in the entire frequency range [45]. It will be shown that uncertainties as large as 1% in the measured reflectivity are not enough to explain the lack of recovery of spectral weight. Moreover, we will show that the spectral weight does not recover below 4.5 eV. We complement this study presenting the optical properties of MnSi [46], $Fe_{1-x}Co_xSi$ ($x = 0.1$, 0.2, 0.3), and CoSi.

4.2 Experiment and Band Structure Calculations

4.2.1 Sample Preparation

High-quality single crystals of TSi (T = Mn, Fe, Co) were grown from the stoichiometric melt either by the floating zone method using a light image furnace in a purified argon atmosphere, or by a modified tri-arc Czochralski method.[92] In this way, large crystals were obtained. The cubic symmetry of them was confirmed by x-ray diffraction analysis. Electron-probe microanalysis showed a stoichiometric and homogeneous single phase.

On the other hand, the single crystals of cobalt-doped FeSi were grown by the chemical vapor transport method. Stoichiometric amounts of the constituent elements were placed in an evacuated quartz tube with elemental iodine, which served as the transport agent. The iodine concentration was typically 2-5 gm/cm^{-3}. The mass of the iodine plus the starting charge totalled approximately 1 gram. The crystals were grown using two different diameter quartz tubes: 16 mm and 22 mm. The larger quartz tubes generally produced larger crystals. The tubes were place in a horizontal tube furnace and heated at 850 °C for a period of ten days. A temperature gradient of approximately 100 degrees was maintained across the tube during the heating process. The larger of the resulting crystals were ~ 2 mm^3 polyhedrons.

For the optical experiments (next Section), the crystals were polished shortly before the measurements. The resulting dimensions were of $\sim 3 \times 3 \times 1$ mm^3 for the pure silicides and no larger than $\sim 1.5 \times 1 \times 1$ mm^3 for the $Fe_{1-x}Co_xSi$ crystals.

4.2.2 Optical experiments

The optical responses of the different crystals were determined at different temperatures by combining reflectivity and ellipsometry in different energy ranges. In the range 6 meV to 0.74 eV (50-6000 cm^{-1}), reflectivity was measured using the Fourier transform technique with the sample inserted in a home-made cryostat. This experiment consisted of two steps. First, the signal reflected from the sample is measured at different temperatures. Then, at 300 K, gold is evaporated in-situ and the reference intensity is measured at the same set of temperatures. For the $Fe_{1-x}Co_xSi$ crystals, a near normal incidence configuration was used while a grazing incidence configuration at 80° was used for MnSi[46]. The latter was chosen to resolve the high reflectivity of MnSi at low temperatures. In addition, the temperature dependence of the normal-incidence reflectivity of FeSi was measured in the range 0.6 to 3.7 meV (5-30 cm^{-1}) using the submillimeter wave technique [94].

The ellipsometry technique was performed in the range 0.74 to 4.46 eV (6000 - 36000 cm^{-1}). We used a commercial ellipsometer equipped with a home-made cryostat which allows to determine the temperature dependence. The advantage of this method is that it permits to determine the complex dielectric function $\epsilon(\omega) = \epsilon_1 + i\epsilon_2$ directly, except for a temperature-independent correction to take into account the change of polarization caused by the windows in the cryostat. This correction can be easily determined at room temperature by performing an ellipsometric measurement with and without windows at the same angle of incidence (see §2.5). This experiment was also performed for a FeSi single crystal whose reflectivity was measured previously [93]. For the $Fe_{0.7}Co_{0.3}Si$ and CoSi crystals we only performed room-temperature ellipsometry since the reflectivity of these crystals changes less than 1% in the measured temperature range and, therefore, the expected changes in the visible range are even smaller. Finally, the temperature dependence of the dielectric function of the MnSi crystal was determined with a step of 1 K between 30 and 300 K, and 0.5K below 30 K.

4.2.3 Band Structure Calculations

The first principles band structure calculations of the compounds of the interest were performed within the framework of local density approximation (LDA) [95] with the Gunnarsson-Lundqvist exchange correlation potential [96]. The self consistent electronic structure calculations of TSi (T = Mn,Fe,Co) as well as $Fe_{0.8}Co_{0.2}Si$ were carried out by using the full potential linear muffin-tin orbital method (FP-LMTO) [97]. In order to calculate the band structure of $Fe_{0.8}Co_{0.2}Si$ a non-integer charge to iron in FeSi was assigned. The room temperature experimental lattice constants and atomic parameters [100, 86, 98] were used. On top of the electronic structure calculation the optical conductivity [99] was evaluated with the **k**-space integration over 216 points in the irreducible part of the Brillouin zone.

4.3 Results

4.3.1 Reflectivity and Dielectric Function

The experimental results are summarized in Figures 4.2 and 4.4. In the first place, the measured reflectivities of the different crystals are shown in Fig. 4.2. The same figure also shows the calculated reflectivity from the ellipsometry data via the Fresnel equations. Notice the good agreement between the two sets of data. For FeSi, the results of the reflectivity measured in the microwave region

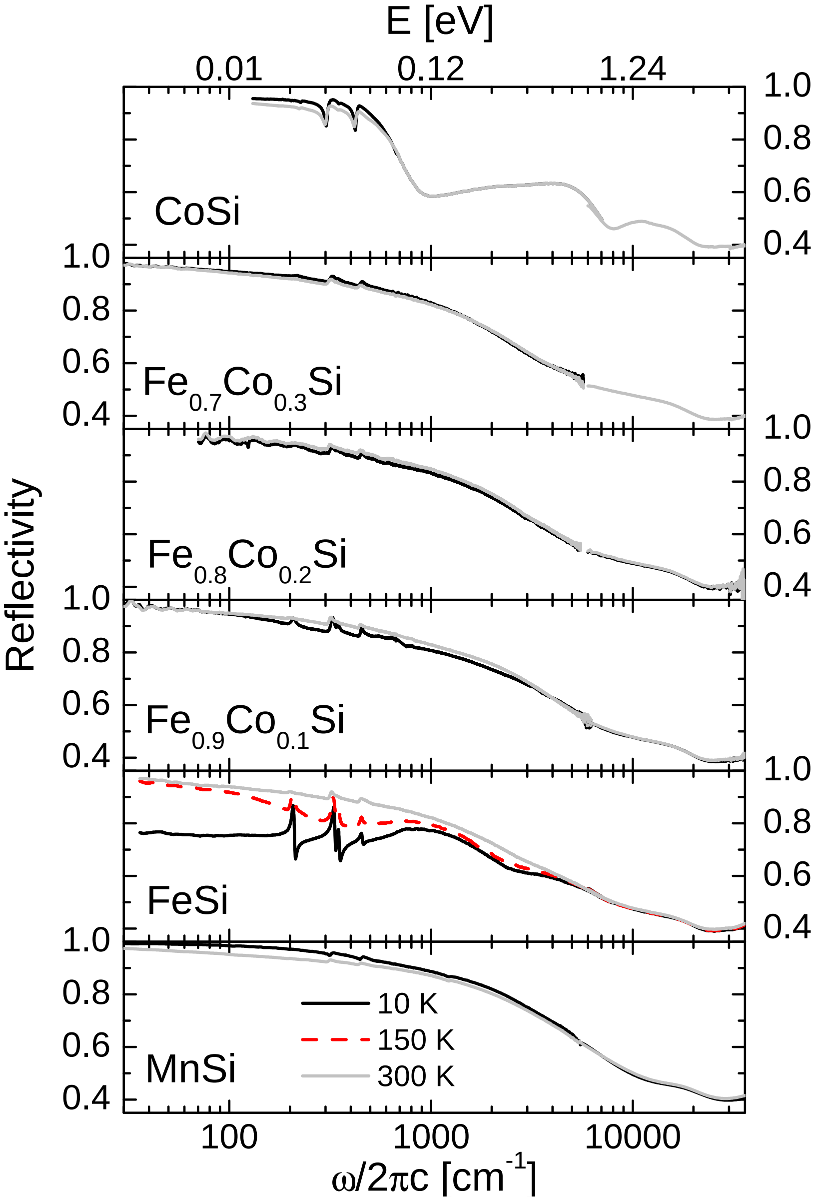

Figure 4.2: *Measured (30-6000 cm^{-1}) and calculated reflectivity from ellipsometry (6000-36000 cm^{-1}) at several temperatures. The agreement between the two techniques is better than 1% in the adjacent regions. For comparison, the normal incidence reflectivity of MnSi calculated from the dielectric function[46] is also reproduced here.*

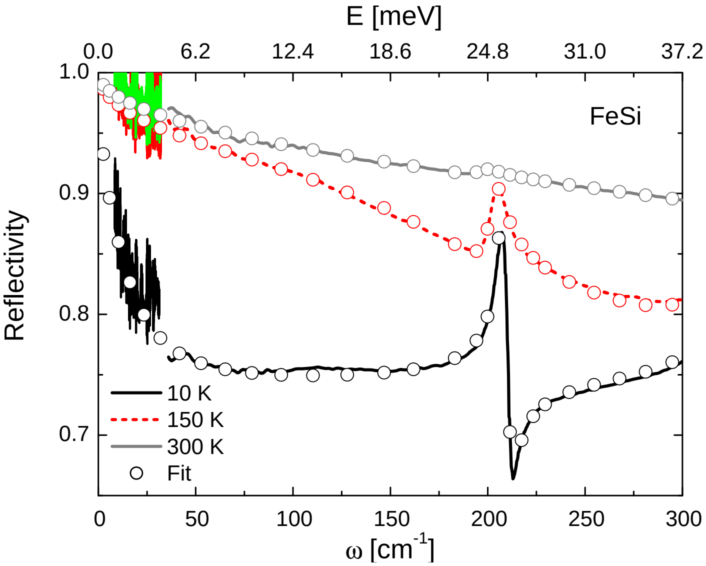

Figure 4.3: *Reflectivity of FeSi in the infrared and the submillimiter region, and fit (open circles), using Eq. 2.19, to the whole set of available data.*

are also shown. Additionally, for comparison purposes, we have also included the normal incidence reflectivity of CoSi [93] and that of MnSi as calculated from the dielectric function which in turn was calculated from grazing incidence reflectivity and ellipsometry[46].

Starting from 300 K, as the temperature is decreased, the reflectivity of FeSi decreases at low frequencies. The same trend can be seen in the $x = 0.1$ and 0.2 samples, though the effect is not as dramatic as in pure FeSi. The opposite tendency is seen in all the other samples. Another important point to notice is the reflectivity of FeSi in the microwave region (see Fig. 4.3). In this region, the reflectivity at 10 K goes smoothly to 100% as expected for a narrow Drude peak of weak strength. Moreover, there is no sign of a broad feature at $\sim$ 10 cm^{-1} assumed to explain the data of Ref. [91].

The second set of experimental data is presented in Fig. 4.4. In that figure we show the real and imaginary part of the dielectric function as obtained from ellipsometry and corrected for the presence of windows in the cryostat. In this region, both ϵ_1 and ϵ_2 are qualitatively similar for all the studied compounds although in CoSi an extra peak can be seen at around 10000 cm^{-1}. Where measured, the temperature dependence is weak but still noticeable. In general, the real part of the dielectric function increases with decreasing temperature, except for MnSi where this happens just above $\sim$10000 cm^{-1}. On the other hand, in all the samples ϵ_2 increases when going from low to high temperatures.

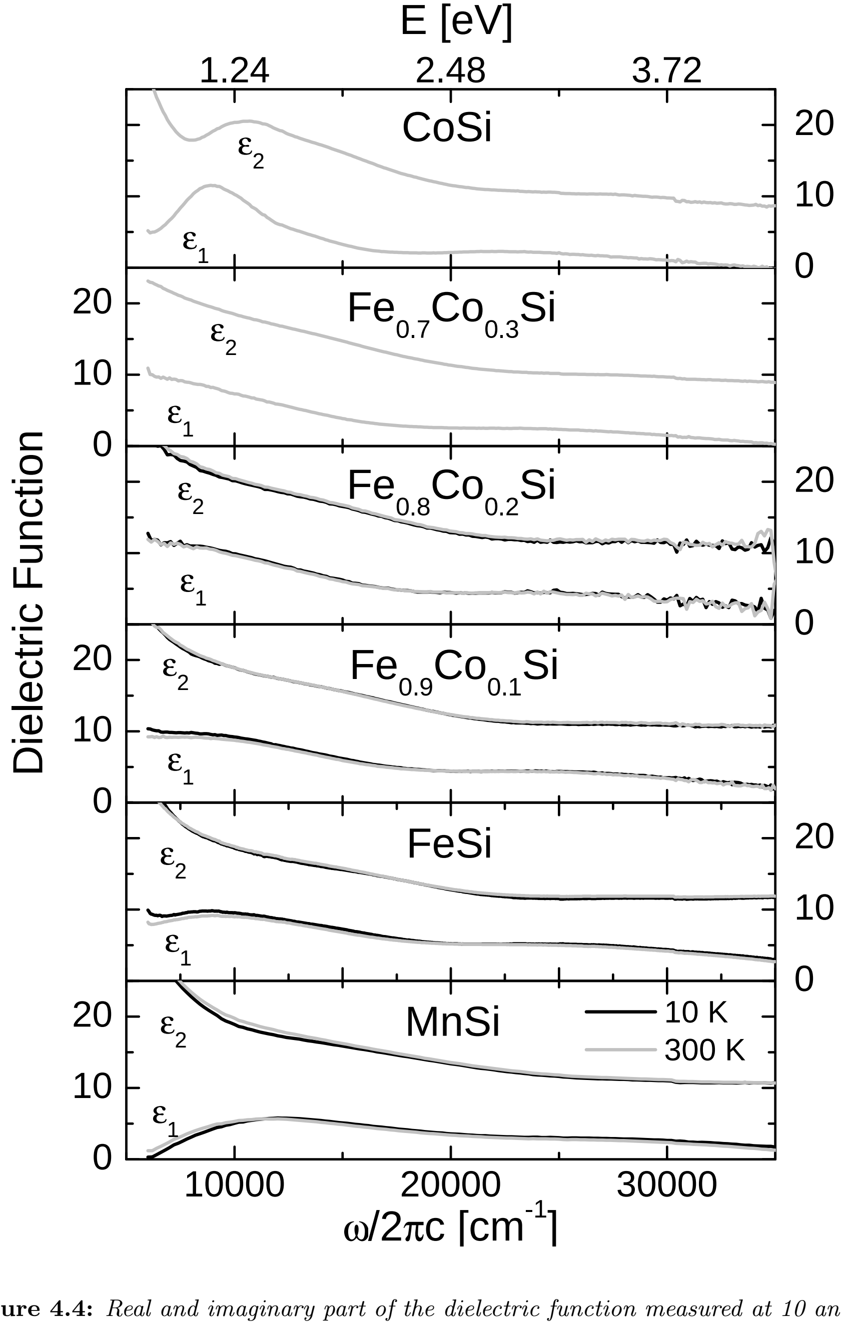

Figure 4.4: *Real and imaginary part of the dielectric function measured at 10 and 300 K.*

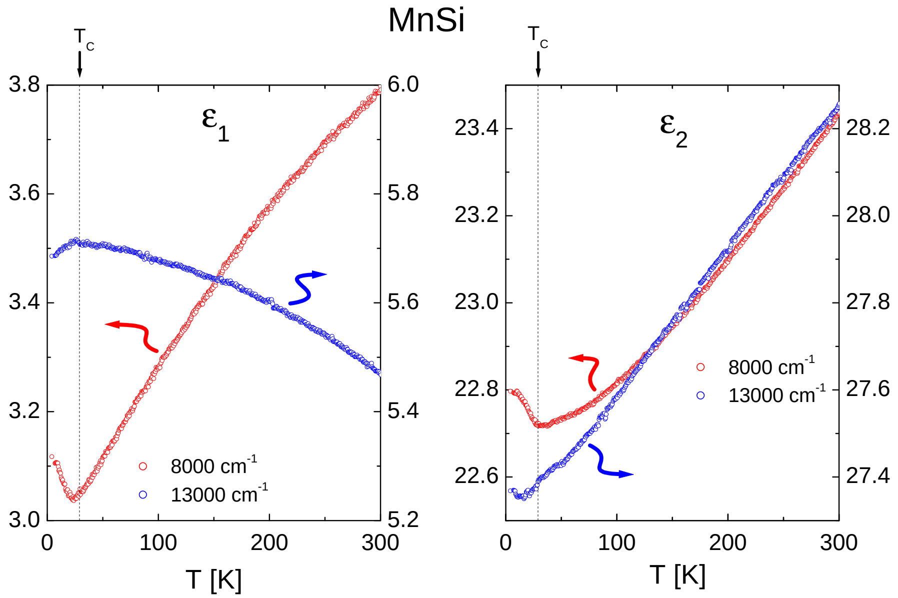

Figure 4.5: *Temperature dependence of the real and imaginary parts of the dielectric function of MnSi at two selected fequencies.*

At the end of this subsection, we want to show Figure 4.5 as an example of the high-resolution (in temperature) measurements of the dielectric function of MnSi. There we plot the temperature dependence of the the real and imaginary parts of the dielectric function at two selected frequencies. Notice the *kinks* below T_C. It will be clear in §4.4, when studying the plasma frequency, that this changes are indeed related to entering the magnetic phase.

4.3.2 Optical Conductivity

The next step in our study is to obtain the optical conductivity in the entire measured range from the two sets of data. For that purpose, we have followed the procedure described in §2.6.1, which we briefly describe here again. For every crystal we have fitted at the same time the DC conductivity (when available), reflectivity (via the Fresnel equations), and the dielectric function using a model dielectric function which is the combination of one Drude and various Lorentz oscillators (Eq. 2.19). For MnSi we used Eq. 2.20 for the zero mode (see Chap. 3). From the fit, we have obtained extrapolations below and above the measured range. This allows to perform a Kramers-Kronig transformation using the measured reflectivity, the reflectivity obtained from ellipsometry and the extrapolations. This procedure has the advantage that the resulting dielectric function is *locked* to the measured one.

The optical conductivities obtained in this way are presented in Fig. 4.6. At room temperature, the conductivity of the $Fe_{1-x}Co_xSi$ samples with a low concentration of Co is slightly dependent on the concentration of cobalt and is qualitatively similar to that in MnSi. Chernikov *et al.* [101] have found a similar behaviour in the case of even lower doping ($x \leq 0.03$), that is, in the non-magnetic region. In FeSi, the temperature dependence of the optical conductivity is similar to previous studies [88, 93, 102]: the optical gap, $\Delta_c \sim 1000$ K, starts to open at a temperature $T^* \sim 200$ K, with Δ_c smaller than the gap seen in scanning tunneling microscopy [103]. In the Kondo insulator picture (which has been proposed for FeSi in Ref. [87]), T^* corresponds to the coherence temperature below which the quasiparticles are formed. This is the reason for which the gap develops below T^*. T^* is an intermediate energy scale smaller than the gap itself. This interpretation is also suggested by scanning tunneling microscopy experiments.[103]

When FeSi is doped with cobalt, a progressive closing of the gap is found [101] and from our experiment we can see that it is already completely closed for $x = 0.1$ although there is still a decrease of the spectral weight in the region where the gap was present in FeSi. This can be easily understood if we considered that close to the gap the bands are mainly of Fe nature (the bands coming from Si lie well below E_F) [102, 104, 105] and, therefore, doping with an 3d element will readily affect the states near the gap [106].

4.3.3 Estimation of the Experimental Uncertainty in $\sigma_1(\omega)$

In this section we want, first, to compare the method just described with the standard one in which solely reflectivity is measured and, second, make an estimation of the experimental uncertainty of both procedures. The experimental uncertainty in obtaining the optical conductivity originate mainly from uncertainties in determining the absolute value of reflectivity. This error depends on the size of the sample and on the way the reference was measured but is usually around 1% and we have assumed this value for the following analysis. It should be noted, however, that the relative error (i.e. when comparing the temperature dependence) can be smaller.

First, to make the comparison, we have fitted only the reflectivity (measured and obtained from ellipsometry) with the model given by Eq. 2.19 and used it as extrapolations for a Kramers-Kronig analysis. The result of this procedure (for FeSi at 300 K) is shown in Fig. 4.7 together with the optical conductivity obtained as described in §4.3.2. The discrepancy between these two methods is evident and emphasizes the advantage of using reflectivity jointly with ellipsometry. A better agreement will be obtained, evidently, if reflectivity is measured in a larger range. Second, the error is estimated by displacing the reflectivity by ±1% in the entire range and repeating the fit and the Kramers-Kronig analysis. The estimation of the error for the method described in §4.3.2 is similar. We have

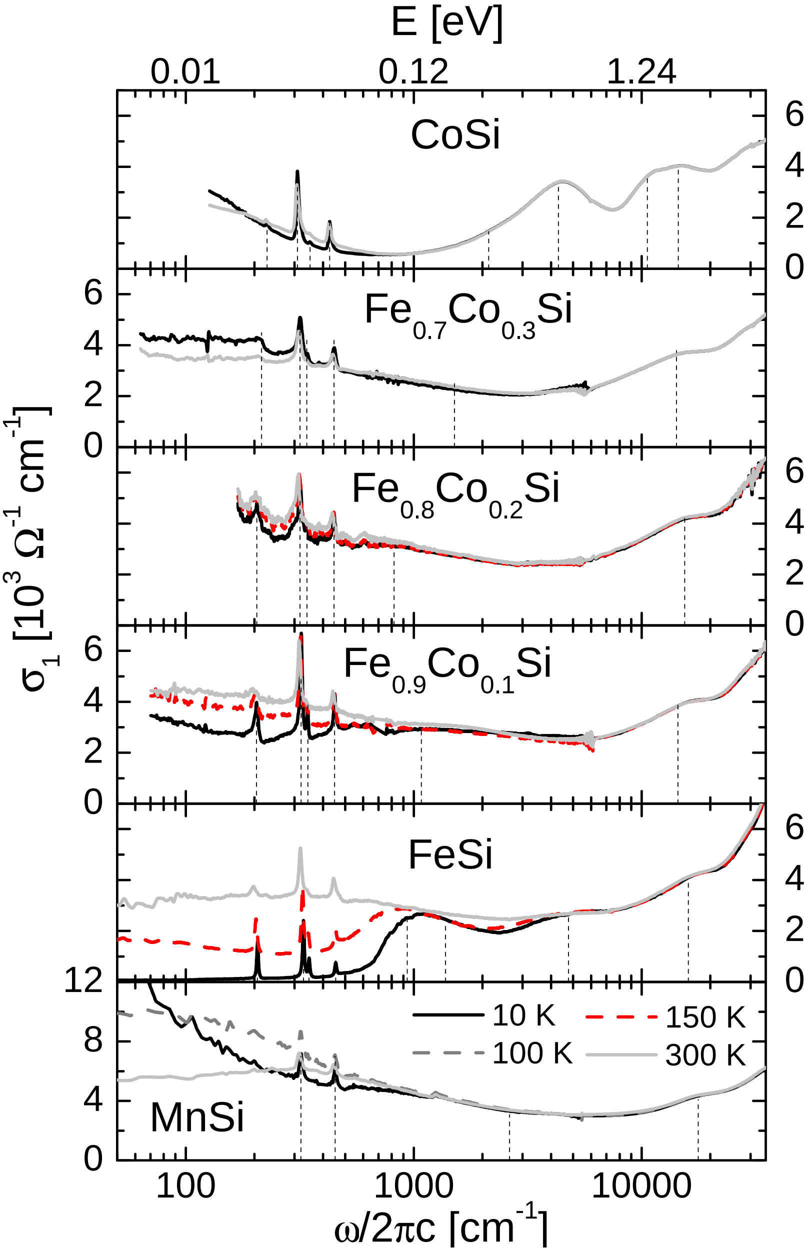

Figure 4.6: *Real part of the optical conductivity for the* $Fe_{1-x}Co_xSi$ *and MnSi crystals. The dotted vertical lines show the position of the oscillators needed to fit the reflectivity and ellipsometry data at 10 K.*

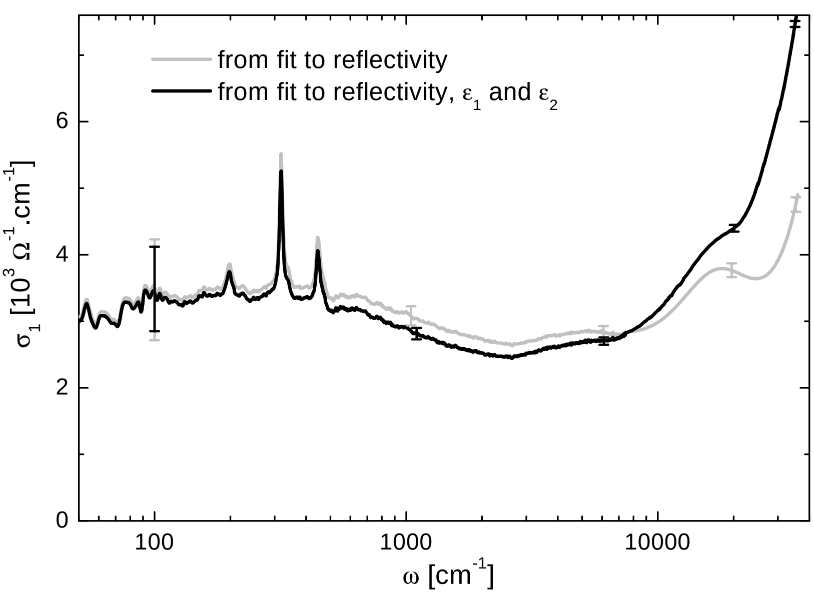

Figure 4.7: *Real part of the optical conductivity obtained from a fit to reflectivity and dielectric function (black line) and to reflectivity only (gray line) using Eq. 2.19 at 300 K for FeSi (for details see text).*

repeated the fit and the Kramers-Kronig analysis with the measured reflectivity displaced by ±1% and the reflectivity calculated from ellipsometry without such displacement. This last step is justified since an error of, for example, 1% (which is larger than the error estimated for our experimental setup) in the real and imaginary part of the dielectric function introduces an error of less than 0.2% in the calculated reflectivity through the Fresnel equations. Our method results in smaller experimental uncertainty in the entire range.

4.3.4 Band Structure

The calculated band structures of TSi (T=Mn, Fe, Co) and $Fe_{0.8}Co_{0.2}Si$ along the symmetry lines in the cubic Brillouin zone are shown in Fig. 4.8. Our results are in good agreement with previous calculations of electronic structure for MnSi [107] and $Fe_{0.8}Co_{0.2}Si$ [108] and with the electronic structure and optics for FeSi [105, 104, 102]. The band structure of all compounds is very similar to each other in the sense that it could be obtained by the rigid shift of one or both spin channels. This can be seen more easily in Fig. 4.9 where the densities of states are plotted. The theoretically predicted ground state of FeSi is non magnetic with a

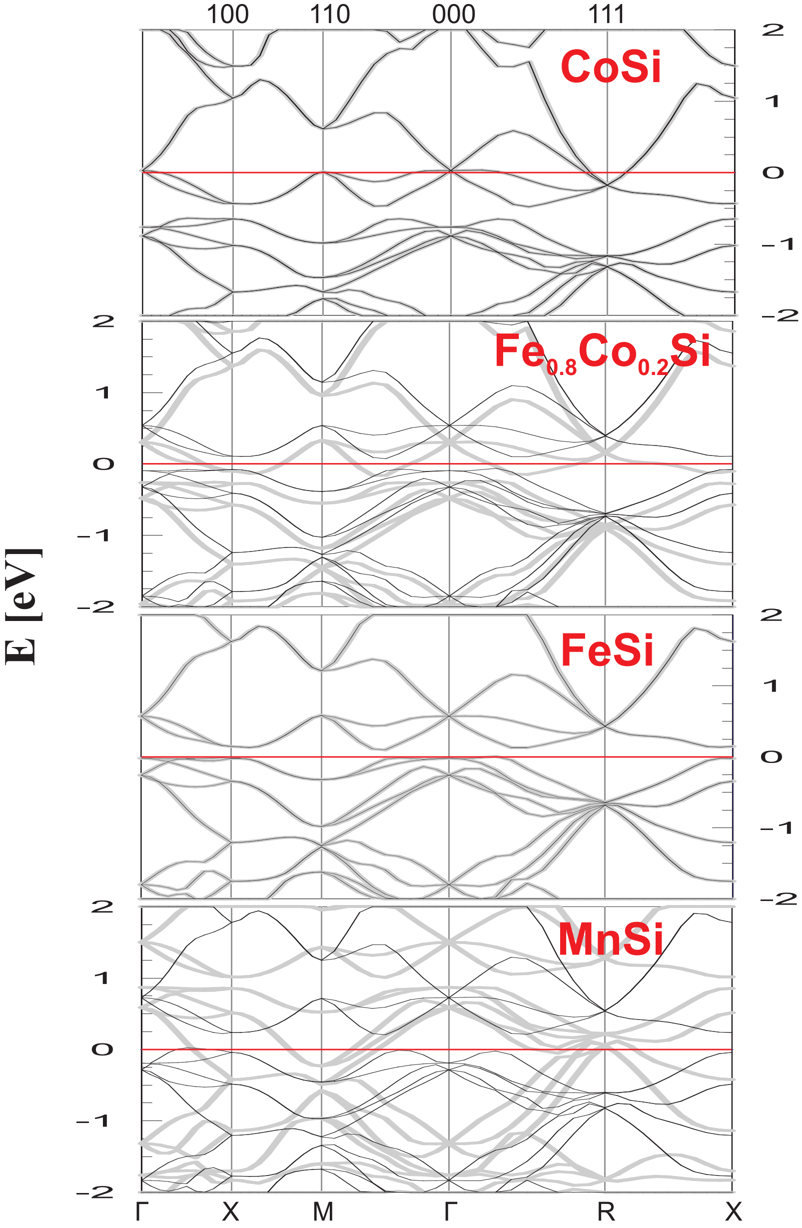

Figure 4.8: *Band structures of TSi (T = Mn, Fe, Co) and* $Fe_{0.8}Co_{0.2}Si$ *with the Fermi energy set to zero. Gray thick lines: spin up bands. Black thin lines: spin down bands. For FeSi and CoSi a non-magnetic ground state is predicted while half-metallicity is predicted for MnSi and* $Fe_{0.8}Co_{0.2}Si$*.*

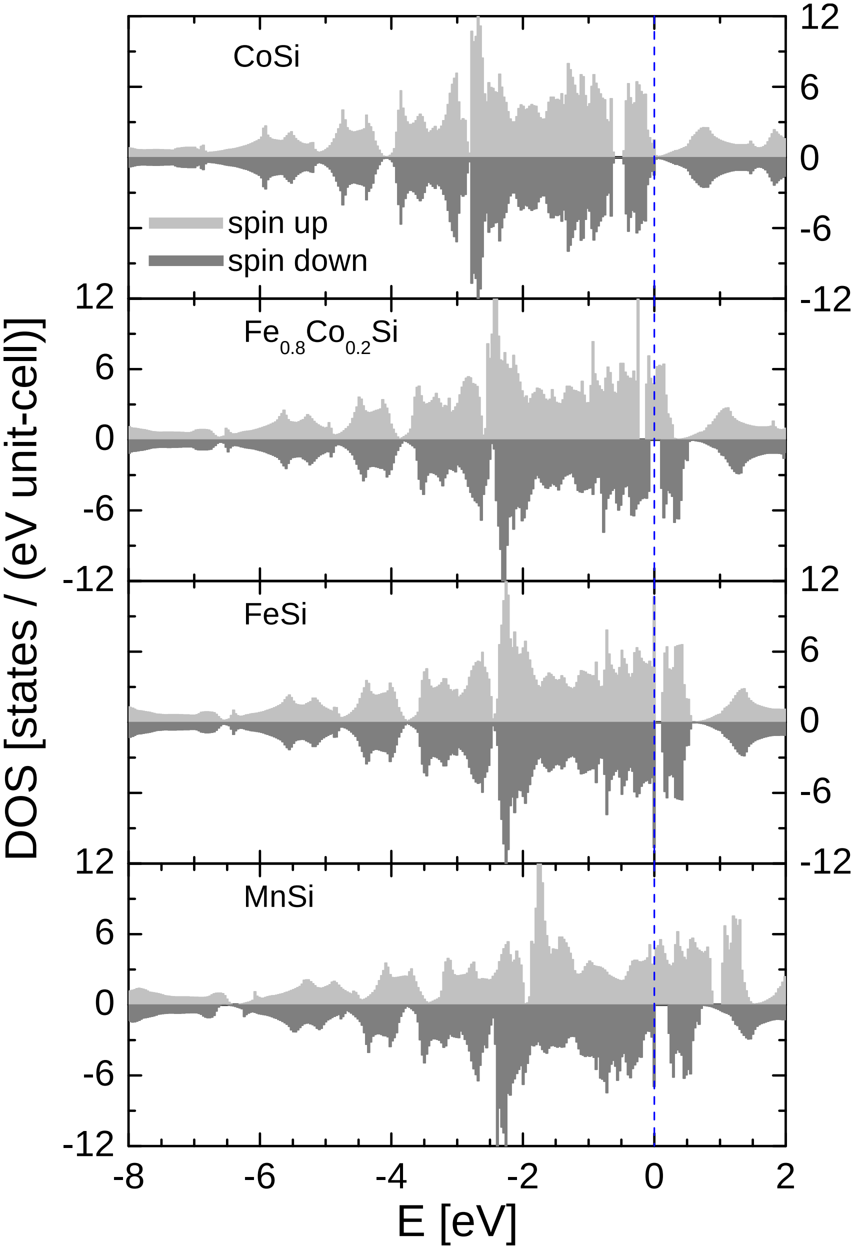

Figure 4.9: *Density of states of TSi (T = Mn, Fe, Co) and* $Fe_{0.8}Co_{0.2}Si$.

small indirect semiconducting gap of the value ~ 0.1 eV. The ground state of CoSi is also non magnetic but metallic which is in consequence of adding four extra electrons in the unit cell. For the other two compounds, MnSi and $\mathrm{Fe}_{0.8}\mathrm{Co}_{0.2}\mathrm{Si}$ the calculations show a half-metallic ground state, i.e. one spin direction is metallic while the other is semiconducting. The obtained values of magnetic moment are 1 and 0.2 μ_B per formula unit for MnSi and $\mathrm{Fe}_{0.8}\mathrm{Co}_{0.2}\mathrm{Si}$ respectively. For $\mathrm{Fe}_{0.8}\mathrm{Co}_{0.2}\mathrm{Si}$, these results, half-metallicity and magnetic moment, agree well with Hall effect and magnetization measurements [7] but, surprisingly, this is not the case for MnSi.

In Fig. 4.10 we have plotted the real part of conductivity calculated from the band structure together with the experimental curves obtained at the lowest temperatures. For a comparison with the experimental data we have introduced a relaxation rate for the Drude term which equals to the one obtained via the oscillator fit described in the previous section (see also Table 4.1). As it was reported previously for FeSi [102, 104], the agreement is good at high frequencies but worsens at low frequencies. We will discuss more about this point in the following section.

4.4 Discussion

4.4.1 Drude-Lorentz model

The results of the Drude-Lorentz fitting described in §4.3.2 are summarized in Tables 4.1 through 4.3. The position of such oscillators are also indicated by the vertical dotted lines in Fig. 4.6. In the first place, the Drude contribution is given in Table 4.1. When going from FeSi to CoSi we see an initial increase of the plasma frequency of this contribution indicating the closing of the gap and the addition of electrons. In CoSi, however, the contribution is smaller than in $\mathrm{Fe}_{0.7}\mathrm{Co}_{0.3}\mathrm{Si}$. We will return to this point latter. The oscillators given in Table 4.2 have been identified as phonons in FeSi[93]. It is clear that they are also present in the Co-doped samples, CoSi, and MnSi. This is not a surprise since all of them crystallize in the same structure. Moreover, for the series $\mathrm{Fe}_{1-x}\mathrm{Co}_x\mathrm{Si}$ ($x = 0$, 0.1, 0.2, 0.3), their strengths ($S_j \equiv \omega_{p,j}^2/\omega_{o,j}^2$) are approximately independent of the concentration.

FeSi

At the other end of the measured frequency range, in FeSi, we can distinguish two oscillators (see Table 4.3) that can be easily identified with the predictions of the optical conductivity obtained from band structure calculations. Such calculations predict peaks at 2 and 6 eV (C and D in Fig. 4.10). Of the two peaks, the former originates from transitions between different $3d$ levels [104]. The second peak is the result of hybridized d to p transitions between the iron and silicon sites with contributions from $4f$ states [102]. Our DL fit produces oscillators that are

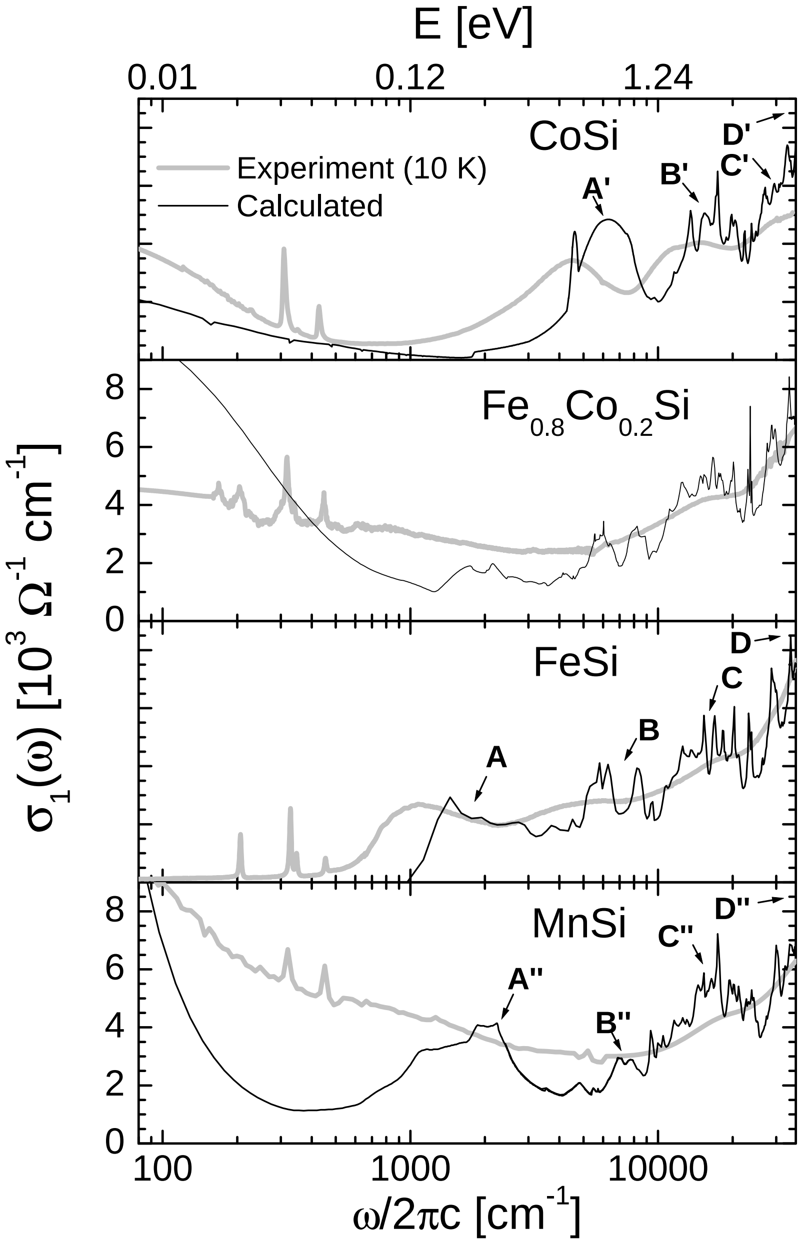

Figure 4.10: *Real part of $\sigma_1(\omega)$ obtained experimentally (thick lines) and calculated from the band structure (thin lines). Note that in the experimental data of $Fe_{0.8}Co_{0.2}Si$ and CoSi the extrapolations are also shown.*

Table 4.1: *Parameters, in cm^{-1}, corresponding to the Drude oscillator used to describe the zero-frequency mode of the different samples at 10 K. Note that for MnSi, instead of the Drude formulation, we used Eq. 2.20.*

Sample	ω_p	Γ	γ	η
CoSi	6852	166	-	-
$Fe_{0.7}Co_{0.3}Si$	10674	434	-	-
$Fe_{0.8}Co_{0.2}Si$	7548	243	-	-
$Fe_{0.9}Co_{0.1}Si$	5448	115	-	-
FeSi	1447	452	-	-
MnSi	18748	2249	0.73	0.23

centered at around 16000 and 42000 cm^{-1} (2 and 5.2 eV respectively), although we can only see the tail of the latter and therefore its precise position is difficult to be determined from the present experiment. The fit also identifies oscillators in the mid-infrared (MIR) region that, however, are not in good agreement with the band structure calculations. In that region, the calculations predict peaks at 0.2 and 1 eV (A and B in Fig. 4.10) also originating from transitions between different $3d$ bands. Our experimental results for FeSi, in contrast, show three oscillators (see Table 4.3), the first one being situated at 4765 cm^{-1}(0.59 eV). The other two oscillators are situated at 936 and 1376 cm^{-1} (0.12 and 0.17 eV), respectively, and are necessary to model the broad peak appearing just above the gap and probably represent only one set of transitions. Although these differences could be within the uncertainties of the calculations, the fact that the predicted peaks are at larger energies than those obtained in experiment can also be an indication of the renormalization due to the importance of electron-electron correlations in this material.[104, 89] Other indication of the importance of significant correlations is the fact that the value of the gap is overestimated in the calculations (middle panel of Fig. 4.10). Given the large experimental and calculated value of the real part of the dielectric function at low frequencies, the expected uncertainties in the determination of the gap are small.[104] In fact, as it will be discussed below, the introduction of correlation effects improves the agreement between theory and experiment [89, 109]. When the temperature is increased, it is not possible to resolve the MIR transitions and only one broad oscillator is sufficient to describe the optical properties of FeSi at room temperature in this region. Furthermore, the gap is closed at temperatures much smaller than the size of the gap, indicating also a non-conventional origin of the gap.

CoSi

Now, let us take a look at the results in CoSi. From the band calculations we see that the band structure is not drastically changed but the Fermi energy moves upwards (~0.6 eV) and is situated above the gap as result of the addition of

Table 4.2: *Parameters, in cm^{-1}, corresponding to the Lorentz oscillators used to describe the phonons of the different samples at 10 K.*

Sample	$\omega_{o,1}$	$\omega_{p,1}$	Γ_1	$\omega_{o,2}$	$\omega_{p,2}$	Γ_2	$\omega_{o,3}$	$\omega_{p,3}$	Γ_3	$\omega_{o,4}$	$\omega_{p,4}$	Γ_4
CoSi	227	126	1	309	1177	7	351	132	3	428	862	9
$Fe_{0.7}Co_{0.3}Si$	215	500	14	317	1035	11	339	300	2	447	687	10
$Fe_{0.8}Co_{0.2}Si$	205	443	5	317	1173	11	340	231	2	447	910	14
$Fe_{0.9}Co_{0.1}Si$	204	750	7	321	1424	9	343	468	3	450	1146	17
FeSi	206	592	3	328	931	5	347	519	5	455	435	7
MnSi	-	-	-	320	828	5	-	-	-	452	673	5

Table 4.3: *Parameters, in cm^{-1}, corresponding to the Lorentz oscillators used to describe the interband transitions of the different samples at 10 K.*

Sample	$\omega_{o,5}$	$\omega_{p,5}$	Γ_5	$\omega_{o,6}$	$\omega_{p,6}$	Γ_6	$\omega_{o,7}$	$\omega_{p,7}$	Γ_7
CoSi	2133	12313	4779	4311	25994	4003	10598	18950	4492
$Fe_{0.7}Co_{0.3}Si$	-	-	-	1509	25961	6178	-	-	-
$Fe_{0.8}Co_{0.2}Si$	-	-	-	820	26281	4365	-	-	-
$Fe_{0.9}Co_{0.1}Si$	-	-	-	1080	31866	6139	-	-	-
FeSi	936	6207	396	1378	10007	1073	4765	33817	8527
MnSi	-	-	-	2634	54180	18094	-	-	-

Sample	$\omega_{o,8}$	$\omega_{p,8}$	Γ_8	$\omega_{o,9}$	$\omega_{p,9}$	Γ_9
CoSi	14467	31000	9121	37410	129386	57585
$Fe_{0.7}Co_{0.3}Si$	14192	63420	24757	39420	99758	38701
$Fe_{0.8}Co_{0.2}Si$	15441	78876	31120	40152	99844	31726
$Fe_{0.9}Co_{0.1}Si$	14408	56635	21828	48016	154488	61694
FeSi	16016	52346	19866	44364	140832	45566
MnSi	17687	38206	16960	45953	145025	56595

the extra electron. Therefore, in the optical conductivity we expect a Drude contribution well separated from interband transitions. Those transitions should be similar to those found in FeSi but shifted ~0.6 eV. This is indeed what the calculated $\sigma_1(\omega)$ shows. Besides a narrow Drude peak we see interband transitions labeled as A'-D' in the upper panel of Fig. 4.10, although C' is somewhat blurred. Then, we can compare these results with the DL fit. Peak A' can be identified with the two broad contributions at 2133 and 4311 cm^{-1}. Peak B' corresponds to the oscillators placed at 10598 and 14467 cm^{-1}. Finally, the oscillator at 37410 cm^{-1} corresponds to peak C' and probably also the tail of D'.

$\mathbf{Fe_{1-x}Co_xSi}$

The doping of FeSi with cobalt can be viewed as a mere shift upwards of the Fermi energy. [106] Accordingly, the situation is expected to be similar to what has been already discussed for CoSi with a smaller shift. However, experimentally this is difficult to see, mainly due to the large width of all the oscillators. In this picture, we would also expect an increase of the spectral weight of the Drude peak which is indeed the case here as can be seen in Table 4.1. When reaching CoSi, ω_p has decreased again since the the Fermi energy is placed in such a way that some conduction bands are already filled.

MnSi

For MnSi a magnetic ground state is predicted. Both, the spin up and down bands are similar (and similar to FeSi) but shifted approximately 0.9 eV. The expected $\sigma_1(\omega)$ should, therefore, be similar to that in FeSi adding the contribution from the spin up bands. The spin up bands contribute with a large Drude contribution and weaker interband transitions. The calculated optical conductivity show these features. Experimentally, the situation is similar to FeSi: a good agreement at high frequencies but somewhat poorer at low frequencies. Particularly, the predicted peak A" transitions is not enough to explain the large spectral weight at low frequencies reflecting in part the non-Drude nature of the zero-frequency mode as described in Chapter 3.

4.4.2 Spectral Weight

The spectral weight contained in the optical conductivity up to a frequency ω was defined in Eq. 2.8 and which we reproduce here:

$$N_{eff}(\omega) = \frac{2mV}{\pi e^2} \int_0^{\omega} \sigma(\omega') d\omega' \tag{4.1}$$

From general principles it can be shown [33, 34] that when $\omega \to \infty$ this quantity is constant at all temperatures and equal to the total number of electrons in one formula unit. Therefore, the infinite frequency limit of $N_{eff}(\omega)$ corresponds to

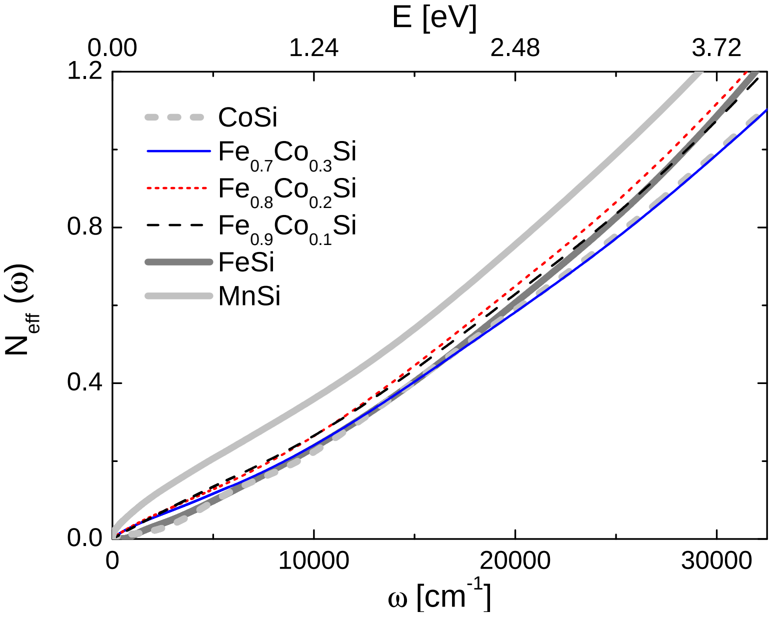

Figure 4.11: *Effective number of electrons per TMSi unit, as calculated with Eq. 4.1, for all the samples at 10 K.*

39 and $40 + x$ for MnSi and $\mathrm{Fe}_{1-x}\mathrm{Co}_x\mathrm{Si}$, respectively. In Fig. 4.11 we show the spectral weight of the different samples at 10 K. It is interesting to note the small number of electrons that participate in the optical properties at such high frequencies: in all the cases less than 1.5 electrons up to 35000 cm^{-1}. To calculate $N_{eff}(\omega)$ we have used the room temperature lattice parameters from References [100] and [86]. The decrease of the unit cell with decreasing temperature has not been taken into account. However, in FeSi this effect would decrease the value of N_{eff} at 10 K by 0.7% [86] and therefore does not affect the conclusions presented below.

Temperature Dependence of the Spectral Weight

The temperature variation of the spectral weight is small and can be seen in a better way by defining the quantity

$$\Delta_T N_{eff}(\omega) \equiv N_{eff}(\omega)|_T - N_{eff}(\omega)|_{10K} \tag{4.2}$$

In this manner, a recovery of the spectral weight would make $\Delta_T N_{eff}$ tend to zero. We show this quantity for the different studied samples in Fig. 4.12. In FeSi we see that at 300 K the spectral weight increases up to frequency of ~ 5000 cm^{-1}(0.62

eV), then there is a small recovery up to $\sim$ 20000 cm^{-1} (2.48 eV) indicated by the plateau and, finally, the spectral weight increases again. Therefore, there is no recovery of the spectral weight at frequencies as high as 4.5 eV. The experimental uncertainty associated with uncertainties in determining the value of reflectivity (see Sec. 4.3.3) are depicted for the room temperature curves. It is evident that the lack of recovery of the spectral weight cannot be explained solely on the basis of experimental uncertainties. As a consequence, this result settles the long standing controversy about the distribution of spectral weight in FeSi. Furthermore, we show that the spectral weight redistributes in an energy range much larger than previously thought.

In a conventional semiconductor the spectral weight lost below the gap is recovered with increasing temperature in an energy range of several times the gap. Therefore, the observation of the lack of recovery of spectral weight in FeSi [88] is seen as an effect of strong correlations confirming the ideas of Aeppli and Fisk [87]. In a system where strong correlations are significant, just few bands are important and models like the Anderson lattice or the one and two band Hubbard models are appropriate. In that case the spectral weight contained in the $\sigma_1(\omega)$ is proportional to minus the expectation value of the kinetic energy of the conduction electrons, $\langle K\rangle$, and thus can have a strong temperature dependance. In the case of Kondo insulators the periodic Anderson model is considered to be appropriate [87, 111] since they contain a flat band of localized f-electrons hybridizing with a broad band of conduction electrons. It has also been suggested that this model applies to FeSi [87] despite the fact that it does not contain f-electrons. Within this context, FeSi can be regarded as a low U Kondo insulator [87]. In fact, the Anderson lattice model applied to Kondo insulators seems to explain naturally the observed lack of recovery of spectral weight [111], that is, one has to integrate $\sigma_1(\omega)$ in Eq. 4.1 to frequencies of the order of the bandwidth to recover the spectral weight. Calculations of $\sigma_1(\omega)$ and $\langle K\rangle$ in the Anderson model using the iterated perturbation theory within the local impurity self-consistent approximation [32] have indeed proven the strong temperature dependence of the spectral weight. However, the predictions from such calculations do not completely reproduce the experimental results. First, in this approach it is necessary to include effects of disorder to obtain a reasonable agreement with the shape of the optical conductivity obtained by experiment [32]. Second, from calculations of $\langle K\rangle$ it can be seen that the spectral weight increases with temperature (inset of Fig. 4.13). This indeed is the behavior obtained in experiment as can be seen from the main panel of Fig. 4.13 where we have plotted the temperature dependence of N_{eff} at 30000 cm^{-1}. However, as the temperature is increased, $-\langle K\rangle$ reaches a maximum and when $T > T^*$ ($\sim$ 200 K in FeSi), it decreases again as result of thermal excitations of the electrons inside the conduction band [32]. This last effect is not seen in our experiment (Fig. 4.13) and, on the contrary, we observe a monotonous increase of the spectral weight. A comparison at a lower frequency (e.g. Fig. 4.14) reveals that the spectral weight tends to saturate at high temperatures but not completely.

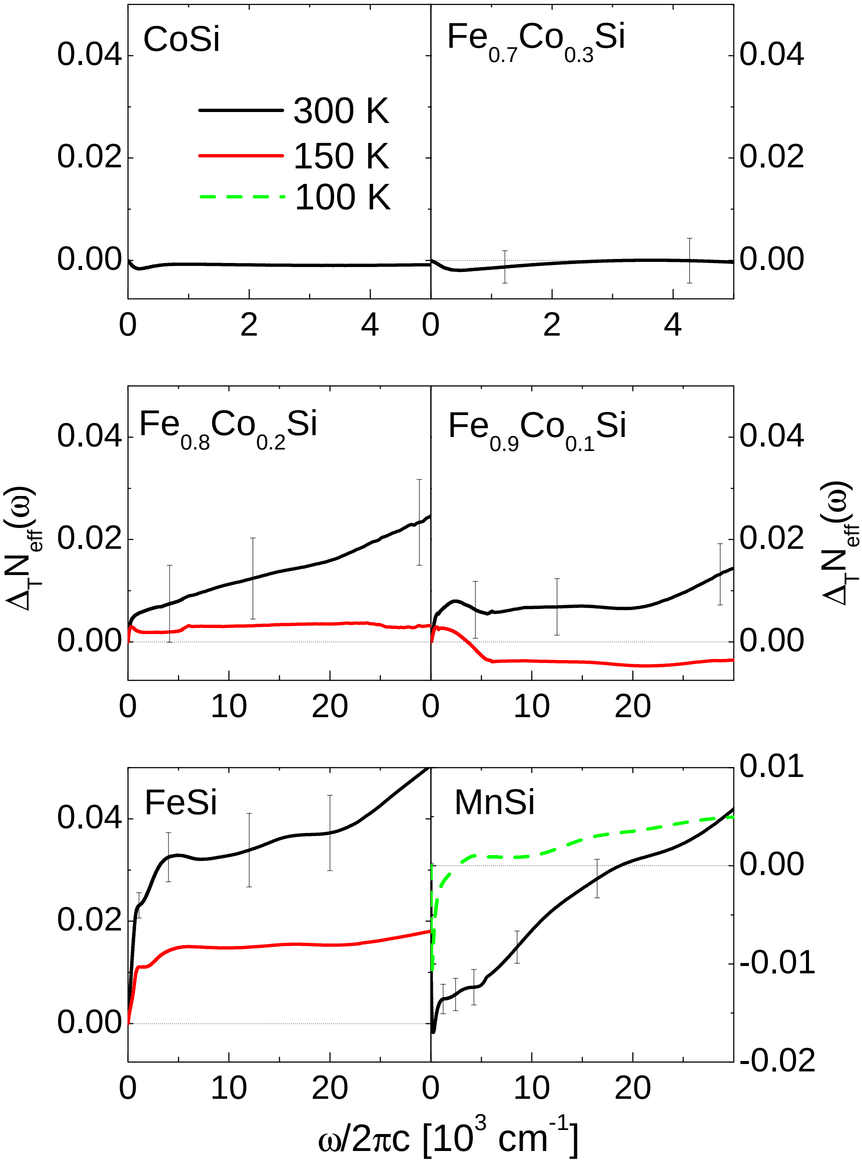

Figure 4.12: *The quantity $\Delta_T N_{eff}(\omega)$ as given by Eq. 4.2 allows to follow the variation of the spectral weight with frequency at different temperatures. Here we show this quantity at 300, 150, and 100 K to demonstrate the lack of recovery of spectral weight.*

Although the various properties of FeSi are similar to the Kondo insulators [87] and our results confirm the importance of strong correlations, the presence of sharp and localized orbitals in this material is a matter of controversy. As a result, the two band Hubbard model has been also proposed to explain the properties of FeSi [89]. In contrast with the Anderson model, the two band Hubbard model takes into account two symmetric bands hybridizing with each other. The original work of Fu *et al.* [89] found a good agreement between the calculated and measured magnetic susceptibility in FeSi. However, the calculated optical conductivity showed a fast recovery of the spectral weight. Subsequent work by Urasaki and Saso [112] found some errors in the calculations of Ref. [89] and when they used an extended two-band Hubbard model[109] (which includes both Coulomb and exchange interactions) with the DOS obtained from band calculations, an excellent agreement with the measured $\sigma_1(\omega)$ was obtained (see Fig. 1 of Ref. [109]). Although the authors have not discussed directly the problem of the spectral weight if it is calculated from their results, it also shows a good agreement with the behavior reported here (Fig. 4.14). This shows that the most suitable model for FeSi is that of the two-band Hubbard model.

The lack of recovery of spectral weight, although in less amount, is present also in the 10 and 20% Co-doped samples (Fig. 4.12). For the $\mathrm{Fe}_{0.8}\mathrm{Co}_{0.2}\mathrm{Si}$ sample, we also show the temperature dependence of $N_{eff}(30000\ \mathrm{cm}^{-1})$ in Fig. 4.13 to clearly demonstrate the lack of recovery of spectral weight. It is also important to notice that even at this high frequencies it is still possible to see the effects of entering the magnetic state. Below 50 K the spectral weight increases slightly and at T_C it starts to decrease again (note that DC resistivity also starts to show changes above T_C and also around 50 K [7]). To determine the origin of this contribution, in Fig. 4.15 we present the results of separating the total spectral weight in contributions below and above 4000 cm^{-1} which is the frequency where $\sigma_1(\omega)$ shows a minimum. This minimum is usually an indication of a separation between intra and interband transitions but in the case presented here the oscillator situated at 1100 cm^{-1} makes this distinction difficult. From Fig. 4.15 we see that the high frequency region mainly contributes with the small raise and posterior decrease of spectral weight associated with the transition to magnetism. Magnetism in this compound seems, therefore, to affect also localized electrons. A further separation of the contributions coming from the Drude peak and from the 1100 cm^{-1}-oscillator is difficult although the DL fit* discussed above can give us an idea of the temperature dependence of the Drude contribution. The spectral weight of this contribution has been plotted in the inset of Fig. 4.15 where we can also see a decrease with decreasing temperature. Hall effect measurements [7] show that there is just a small change of the carrier density when temperature is decreased and that no change at all occurs at T_C. Therefore, the effective mass of the carriers increases down to the lowest temperature without too much change

---

*Following a similar approach as in Ref. [10] (i.e. choosing the width of the Drude curve as large or small as possible that still fit the data) gives the same result.

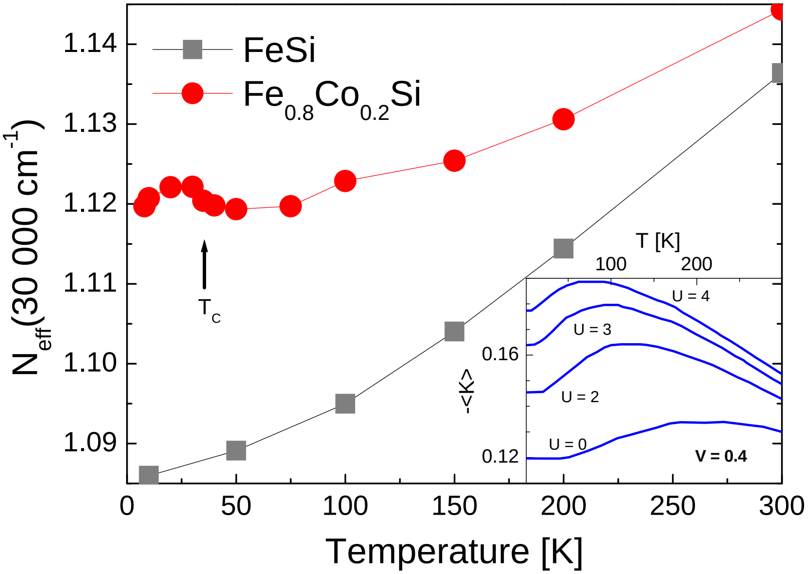

Figure 4.13: *Comparison between of the spectral weight for FeSi and* $Fe_{0.8}Co_{0.2}Si$ *at 30000* cm^{-1}*. In both materials the lack of recovery of spectral weight is evident. The behaviour of* $Fe_{0.8}Co_{0.2}Si$ *should be compared with that seen in manganites and* $Ga_{1-x}Mn_xAs$*. For example, see Fig. 11 of Ref. [113]. The arrow shows* T_C *of* $Fe_{0.8}Co_{0.2}Si$ *as determined in Ref. [74].* Inset: *Behavior of -*$\langle K \rangle$ *(which is proportional to the spectral weight) as obtained in Ref. [32] for the Anderson lattice model.*

at the transition to magnetism.

In contrast with the low-Co-doped samples, $Fe_{0.7}Co_{0.3}Si$ seems to gain spectral weight when the temperature is decreased. However, the DL fit reveals that there is indeed a lowering of the plasma frequency of the Drude contribution. The apparent increase of spectral weight is due to the accompanying large decrease of the scattering rate. A similar situation occurs in CoSi and MnSi. In the latter, this is particularly dramatic since the scattering rate is strongly temperature dependent giving rise to a narrow peak centered at zero frequency.

A further evidence of the direction of the transfer of spectral weight comes from studying the temperature dependence of the zero crossing of the real part of the dielectric function [115]. In a system where interband transitions are well separated from the intraband ones, the zero crossing of $\epsilon_1(\omega)$ (which we will denote ϖ_p) give directly the plasma frequency of the zero mode (and therefore its spectral weight). In our case, the presence of a strong mid-infrared oscillator makes the situation more complicated. However, ϖ_p will give us information of the spectral

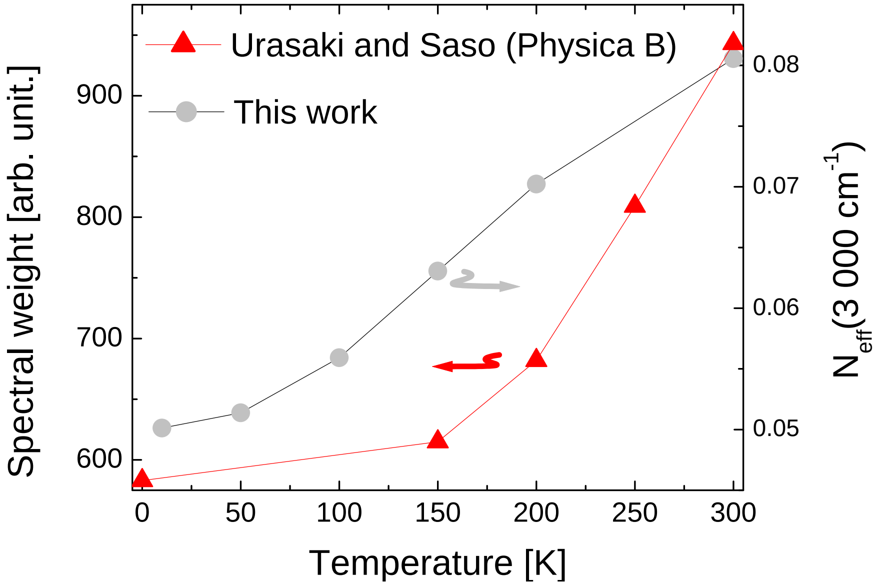

Figure 4.14: *Comparison between* $N_{eff}(3000)$ *cm*$^{-1}$ *in FeSi and the spectral weight calculated from Ref. [109]. Notice that both scales expand the same percentage.*

weight of the low laying oscillators. We show the temperature dependence of the zero crossing of $\epsilon_1(\omega)$ for MnSi in Fig. 4.16. In this Figure we can see how, starting from room temperature, ϖ increases when temperature decreases. However, after crossing the Curie temperature, it decreases signaling the decrease of the spectral weight at low frequencies when MnSi enters the magnetic state. The inset of the same Figure shows the derivative of ϖ which confirms a maximum at T_C.

The behaviour just described is in clear contrast with what occurs in other magnetic materials like the manganites [113], Mn-doped GaAs [10] or EuB$_6$[11]. In the first two systems the spectral weight above the Curie temperature is approximately constant, then as the temperature is lowered below T_C there is an increase of the spectral weight at low energies which recovers at some high energy depending on the specific material. In the manganites [113] this occurs at around 2-3 eV while, on the other hand, in the Ga$_{1-x}$Mn$_x$As system [10], it occurs at ~1 eV. In the case of EuB$_6$, a DL analysis found a strong increment of the plasma frequency (and, therefore, of the spectral weight) of the Drude peak below T$_C$ [11]. The increase of spectral weight below T$_C$ has been interpreted as a decrease of the effective mass of the carriers [9] which is the result of bond-charge Coulomb repulsion. This phenomenon is suggested to be the driving force of ferromagnetism in all cases [9]. Our experimental results show that this seems not

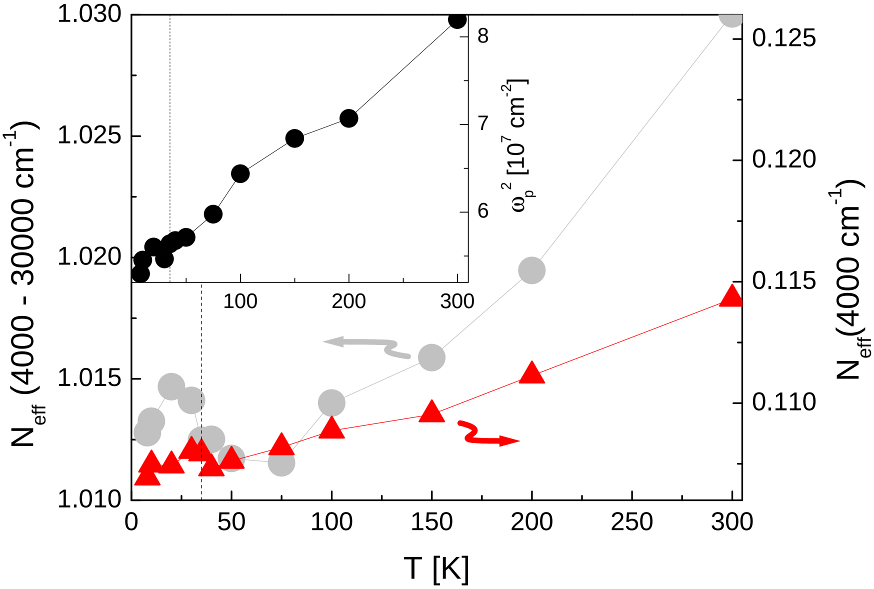

Figure 4.15: *Contributions to the the total spectral weight above and below 4000* cm^{-1} *(circles and triangles, respectively) in* $Fe_{0.8}Co_{0.2}Si$. *Notice that both scales span 0.02.* Inset: *Temperature dependence of the spectral weight of the Drude peak obtained in the DL fit. In the main panel and the inset, the vertical dotted lines indicate* T_C.

to be the case. Although the actual mechanism is not clear, a clue can be unveiled from the model proposed for transport in this system by Manyala *et al.* [7]. They proposed that the main ingredients for magnetism in the Co-doped FeSi is strong correlations enhanced by disorder [7]. Regarding the strong correlations, our optical measurements confirm their presence in these materials as is manifested by the lack of recovery of spectral weight.

Concentration Dependence of the Spectral Weight

Figure 4.17 shows how the effective number of carriers depends on concentration. This figure depicts the difference

$$\Delta_x N_{eff}(\omega) \equiv N_{eff}(\omega)|_{doped} - N_{eff}(\omega)|_{FeSi} \tag{4.3}$$

at 10 K. It has to be remembered that when $\omega \rightarrow \infty$, this quantity has to equal -1 for MnSi and x for $Fe_{1-x}Co_xSi$. At the highest measured frequency, the values of $\Delta_x N_{eff}(\omega)$ are still much lower than those limiting values. This reflects the large spectral weight that transitions at higher energies should have.

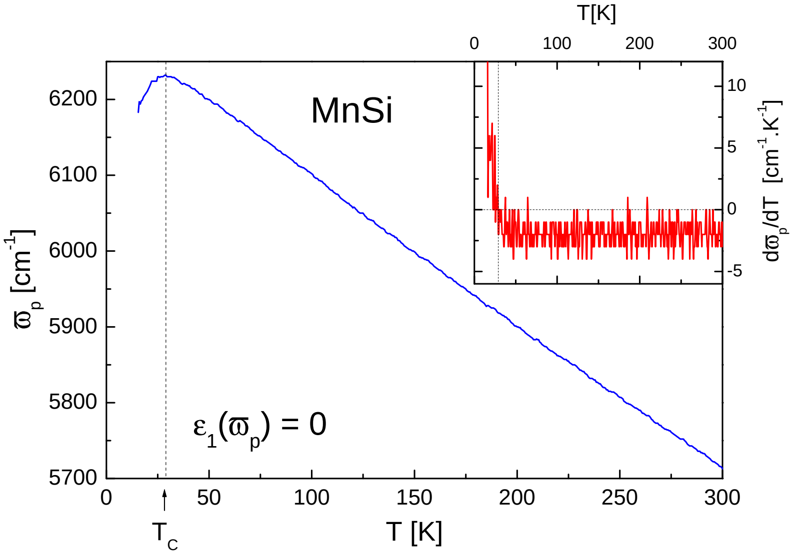

Figure 4.16: *Temperature dependence of the zero crossing of the real part of the dielectric function, ϖ, of MnSi. Inset: Derivative of ϖ.*

At the lowest temperature, all the silicides studied here, except FeSi, are metallic. This is reflected in $\Delta_x N_{eff}(\omega)$ which is larger than zero at low frequencies in all the cases. In MnSi the steep initial increase reflects the long mean free path of the free carriers[46]. Regarding the cobalt doping of FeSi, the addition of electrons is reflected in the progressive increase of N_{eff} in the compounds with a doping of 0.1 and 0.2. However this addition is not restricted to the free carriers since $\Delta_x N_{eff}(\omega)$ saturates at values below x.

The bottom panel of Figure 4.18 depicts the effective number of carriers at 1000 cm^{-1} as function of doping (respect to FeSi). This panel shows that the effective number of carriers start to increase with the addition of electrons but it is not linear with doping. The presence of a broad MIR oscillator contributing to the $\sigma_1(\omega)$ of the Co-doped samples does not allow to determine whether this is a characteristic of the free added carriers or not. For that reason we present the doping dependence of the plasma frequency of the Drude peak (top panel of Fig. 4.18). When FeSi is doped with cobalt, ω_p^2 starts to increase linearly with doping in the same fashion as magnetization does [7]. This can also be seen in the inset. However, when reaching $Fe_{0.7}Co_{0.3}Si$, the spectral weight of the Drude peak increases larger than linearly, suggesting that not all the conduction electrons are fully polarized as in the case of lower concentration. If from the squared plasma frequency of $Fe_{0.7}Co_{0.3}Si$ subtract ω_p^2 of CoSi (which is non-magnetic), the difference is proportional to magnetization (gray dots). This relation should

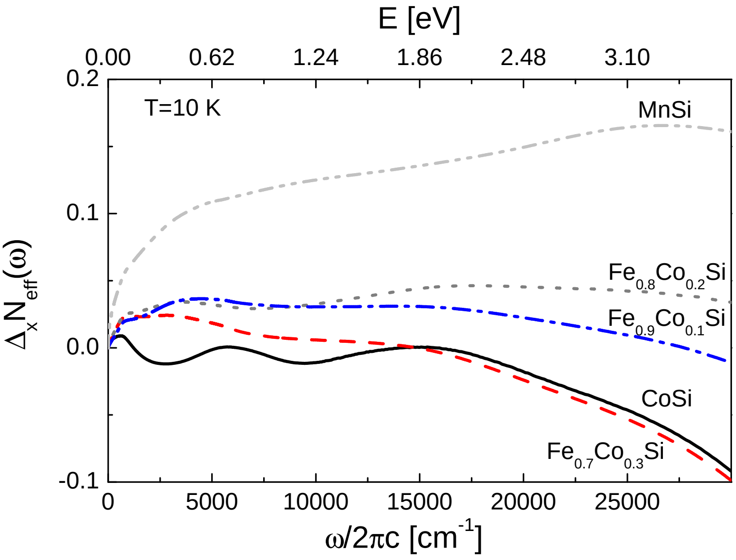

Figure 4.17: *Concentration dependence of $N_{eff}(\omega)$ as given by $\Delta_x N_{eff}(\omega)$ (Eq. 4.3).*

be checked experimentally for other concentrations.

4.5 Conclusions

In this chapter, we have presented the optical properties of various cobalt-doped iron silicides $Fe_{1-x}Co_xSi$ ($x = 0$, 0.1, 0.2, 0.3, 1), and MnSi. These properties were obtained by combination of reflectivity and ellipsometry measurements. The advantage of including ellipsometry is to reduce the uncertainties introduced when $\sigma_1(\omega)$ is obtained via the Kramers-Kronig relations. Then we have shown that, although the band structure calculations explain partially the optical properties of FeSi, it is necessary to introduce electron correlations for a complete description. Strong correlations explain in a better way the lack of recovery of spectral weight in a wide energy range. In this respect, calculations based on the Anderson lattice model account for this effect although not in detail [32]. A model with two symmetric bands seems to be more appropriate [89, 112, 109].

The origin of the Kondo picture for FeSi can be seen intuitively if an atomistic picture is considered.[114] In the B20 structure (Fig. 3.1), the Fe atom has seven Si atom neighbors as shown in Fig. 4.19a. Assuming that a ligand field description can represent the influence of the Si-matrix, the electronic diagram presented in Fig. 4.19b has been obtained, where the d-states of the Fe atom hybridize with p-states of the Si atom.[114] Around the Fermi energy there are two types of

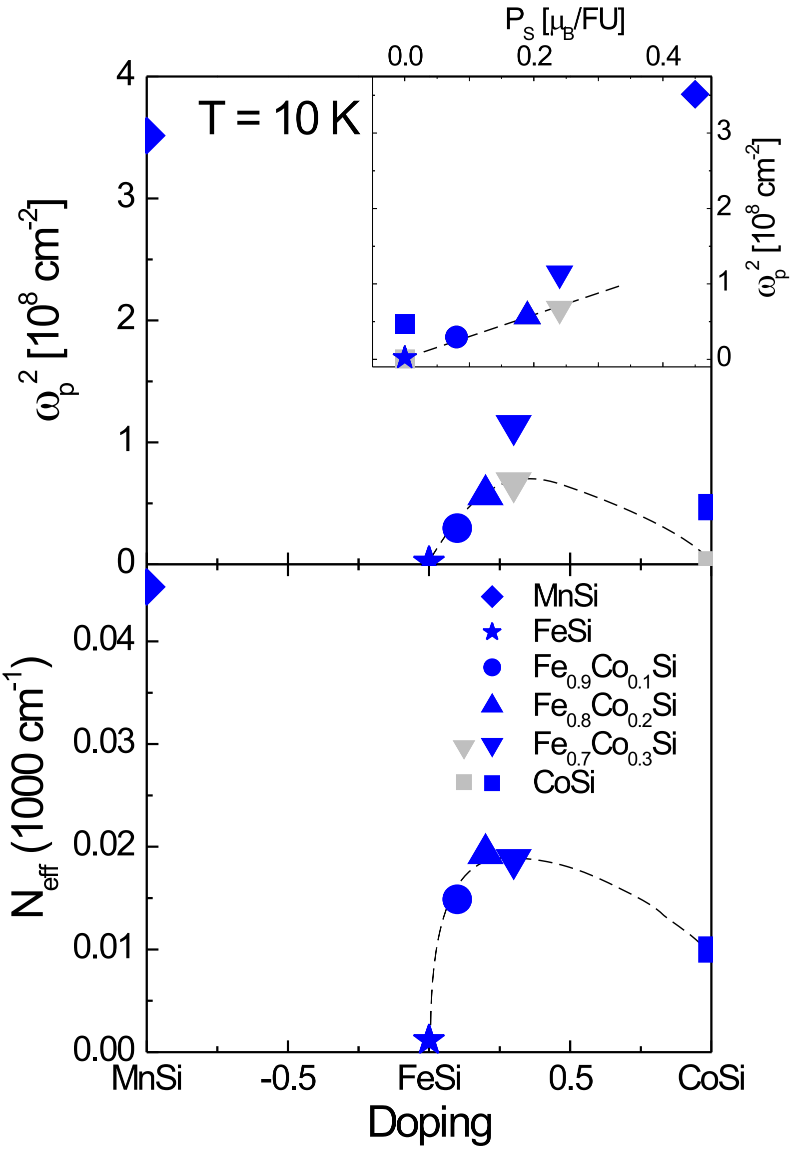

Figure 4.18: *Doping dependence (respect to FeSi) of: N_{eff}(1000 cm^{-1}) (bottom panel) and Drude plasma frequency (top panel). The inset of the top panel shows the plasma frequency of the Drude peak versus magnetization. The gray dots correspond to the plasma frequency after subtraction of ω_p^2 of CoSi. The dashed lines are guides for the eyes.*

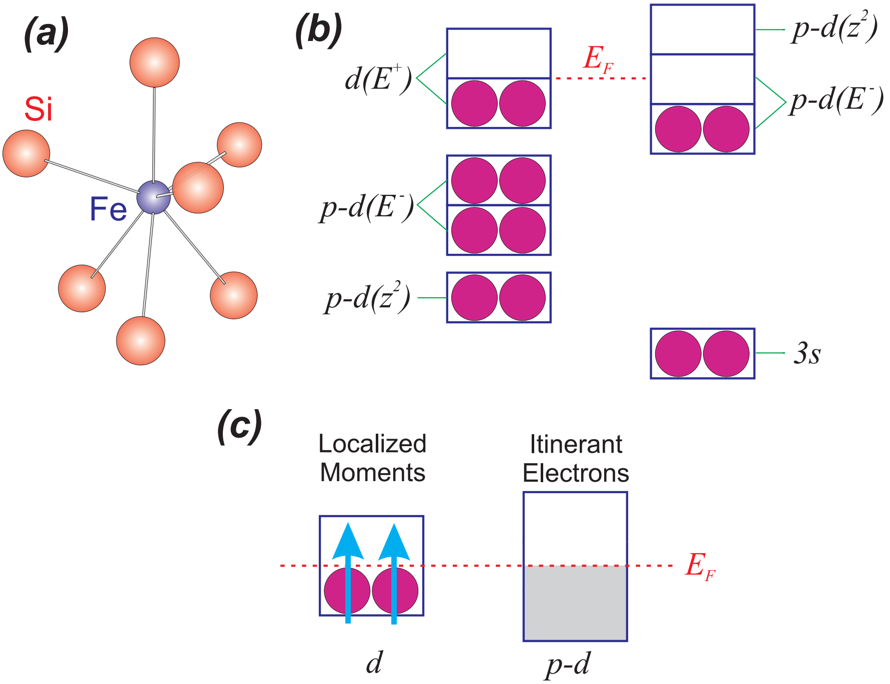

Figure 4.19: *(a) $FeSi_7$ cluster formed in the B20 structure. (b) Diagram of the energy levels in FeSi where the solid circles represent the electrons occupying each state. Notice the position of the Fermi energy. (c) Schematic diagram of the relevant low energy degrees of freedom in FeSi. (adapted from Ref. [114]).*

bands, one antibonding band containing three states and one non-bonding band with two states. If the width of the later is sufficientely small, it has quasiatomic character and fills following Hund's rule while the antibonding band has an itinerant character (see Fig. 4.19c). Therefore, we have all the ingredients for the Kondo picture. At high temperatures the localized moments and the itinerant electrons are independent and the total moment is $S = 1$. At low temperatures, the itinerant electrons quench the moment completely as there are also 2 electrons in the itinerant band.

Finally, regarding the magnetic samples ($Fe_{1-x}Co_xSi$ and MnSi), we have shown that the temperature dependence of the spectral weight is remarkably different from other magnetic compounds (manganites and Mn-doped GaAs), i.e. decreases below T_C at low frequencies. This behaviour suggest that the mechanism of magnetism is different in $Fe_{1-x}Co_xSi$. Its principal ingredient is the presence of strong correlations which have been identified from the lack of recovery of spectral weight also present in these compounds.

Chapter 5

Optical Spectroscopy of Heavy Fermion Systems

The optical properties of the heavy fermion family $\mathrm{CeMIn_5}$ (M = Co, Rh, Ir) have been determined in the photon energy range from 2 meV to 4.5 eV using the combination of near normal incidence reflectivity (2 meV - 0.8 eV) and ellipsometry (0.8 - 4.5 eV). In all compounds, signatures of the formation of a coherent state are found. However, as a result of the competition with antiferromagnetism, the energy region where the coherent state occurs is much lower in the compound that orders magnetically. Furthermore, the optical properties of the non-magnetic counterpart of one of the members have also been determined.

5.1 Introduction

Cerium based compounds are well known to exhibit strongly correlated electronic phenomena. Among them, the materials of the $\mathrm{CeMIn_5}$ (M = Co, Rh, Ir) group have recently attracted considerable attention. The reason is their unusual properties, especially their unconventional superconductivity similar to the high T_c superconductors [116, 120] and, presumably, proximity to a quantum critical point (with pressure [120, 121] and magnetic field [119] as tuning parameters). The analogy with the high T_c superconductors even starts with their crystal structure which can be seen as layers of $\mathrm{CeIn_3}$ separated by $\mathrm{MIn_2}$ layers (see Fig. 5.1). This has also have raised the question of the effect of low dimensionality in heavy fermion systems. These heavy fermion compounds exhibit an ample gamut of properties that reveal the subtle interplay between magnetism and superconductivity [122] as it can be seen in their phase diagram which is shown in Fig. 5.2. $\mathrm{CeCoIn_5}$ is the heavy fermion compound with the highest superconducting transition temperature, T_c, at ambient pressure (2.3 K) [117, 122]. $\mathrm{CeRhIn_5}$ does not superconduct at ambient pressure but is an antiferromagnet below T_N =3.8 K

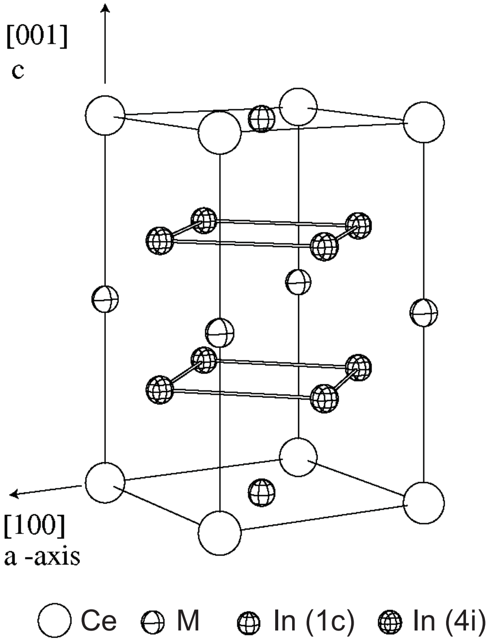

Figure 5.1: *Crystal structure of CeMIn$_5$ (adapted from Ref. [18]).*

[118]. Finally, CeIrIn$_5$ superconducts at a relatively low temperature (0.4 K) and does not order magnetically [116].

The physics of a single magnetic impurity in a non-magnetic metallic matrix is characterized by a single temperature T_K (Kondo temperature). Below T_K, the local moment of the impurity is screened by the conduction electrons and the system can be described as a Fermi liquid. Moreover, all thermodynamic quantities scale with the reduced temperature T/T_K. An important question in the Kondo lattice (a lattice of magnetic centers) is whether the temperature below which the moments are locally screened (T_K) coincides with the temperature below which the Fermi liquid is formed (T^*) and how these are related to the Kondo temperature of the single impurity[123]. Experimentally, T^* is usually associated with T_{coh} which is the temperature where the resistivity shows a maximum. If intersite interactions are not taken into account, calculations in the dynamical mean-field theory [123, 124] indicate that there are two completely different energy scales. The first one, T_K, coincides with that of the single impurity case while the second one depends only on the ratio between the conduction and f-electron densities, (n_c/n_f). It turns out that when $n_c/n_f \sim 1$, T^* is slightly enhanced over T_K but rapidly decreases as the exhaustion regime is reached ($n_c \ll n_f$). If, on the other hand, intersite interactions are considered [126], the single impurity and the

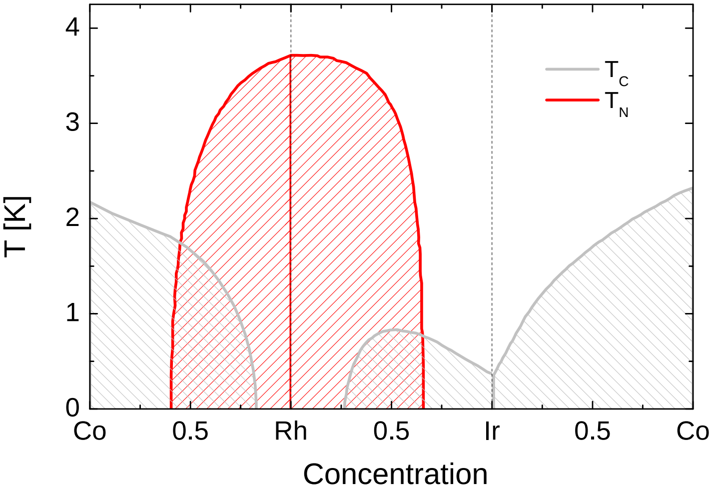

Figure 5.2: *Phase diagram of CeMIn$_5$ (adapted from Ref. [122]).*

lattice are caracterized by two different Kondo temperatures.

In contrast with this point of view, from the study of the effect of substitution of the Ce atom by La in CeMIn$_5$ (M = Co, Rh, Ir), Nakatsuji *et al* [127, 128] have proposed that the single impurity energy scale ”survives” when going to the lattice with T^* being the result of intersite correlations. At high temperatures, the Kondo lattice behaves as a set of non-interacting magnetic impurities (Kondo gas) which condense below T^* (Kondo liquid). However, they suggest, the condensation is not complete when the material is close to a quantum critical point, and at low temperatures the material can be described as a two component system. Since there is no evidence for a spatial phase separation, what occurs below T^* is a transfer of spectral weight from the high frequency part of the spectrum (corresponding to the localized Kondo moments) to the low frequency part (corresponding to the coherent state). In the present work we present optical measurements in the CeMIn$_5$ family. We experimentally see how antiferromagnetism (AF) competes with the formation of the coherent state. This competition manifests itself in lower values for the characteristic energies of CeRhIn$_5$ in comparison to the compounds that do not order magnetically. We will see that the loss of spectral weight associated with the formation of the coherent state occurs in the same energy range for all three members of the CeMIn$_5$ family. Furthermore, the energy where this recovery occurs is much larger than the region where the mass enhancement occurs which seems to be a common feature in Kondo systems.

5.2 Optical Properties of CeMIn$_5$ (M = Co, Rh, Ir)

5.2.1 Experiment and Results

High quality single crystals of CeMIn$_5$ (M = Co, Rh, Ir) were obtained from an In-rich flux [116, 117, 118]. After polishing, the optical properties of the ab-plane were determined at different temperatures by combining reflectivity at near normal incidence (11°) and ellipsometry. The reflectivity (Fig. 5.3) was determined from 30 to 6000 cm^{-1} using a Fourier transform spectrometer. The temperature dependence was measured using a home-built cryostat with the intensities calibrated against a gold reference film evaporated *in situ* on the sample. In the Co and Ir compounds, the overall behaviour of the reflectivity is similar to a previous study of CeCoIn$_5$ [129]: a metallic behavior at high temperatures and a strong temperature dependence especially below 2000 cm^{-1} and 50 K which signals the development of the coherent state. In the Rh compound the temperature dependence is weaker.

Ellipsometry of the ab-plane, on the other hand, was performed from 6000 to 36000 cm^{-1} with an ellipsometric spectrometer at an angle of incidence of 80°. At the same set of temperatures as the reflectivity experiment, spectra were taken using a home-made ultra high vacuum cryostat. These spectra give the *pseuso-dielectric function* which have to be corrected for the c-axis response. For this purpose we also measured, at room temperature, the near normal reflectivity of the ab-plane*. As an example, we show the results for CeCoIn$_5$ in the gray circles of Fig. 5.3(a). The correction was of less than 1% and, therefore, we have taken the ellipsometric spectra as the dielectric function.

5.2.2 Optical Conductivity and Hybridization Gap

From the complete data set, the complex dielectric function, $\epsilon(\omega) = \epsilon_1(\omega) + i(4\pi/\omega)\sigma_1(\omega)$, was calculated in the infrared (30-6000 cm^{-1}) using Kramers-Kronig relations (KK), following the procedure described in Chapter 2. In Fig. 5.4 we show $\sigma_1(\omega)$ in the entire frequency range. The temperature dependence of the optical conductivity of the Co and Ir compounds at low frequencies follows closely what has been previously seen in other heavy fermion systems. Above T_{coh} the optical conductivity can be described by a single Drude peak while below it, a minimum appears signaling the appearance of a more narrow Drude peak. The origin of this behavior is the development of the so-called hybridization gap, Δ, as

---

*For this measurement, we started with the sample with gold evaporated in its surface. The dielectric function of this film was determined first via ellipsometry. Later, in near normal incidence configuration, the intensity of the gold was measured. Then the gold film was removed and the intensity of the sample was also measured. The ratio of this two quantities, corrected by the gold reflectivity (obtained from the ellipsometric measurement), gives the high frequency reflectivity.

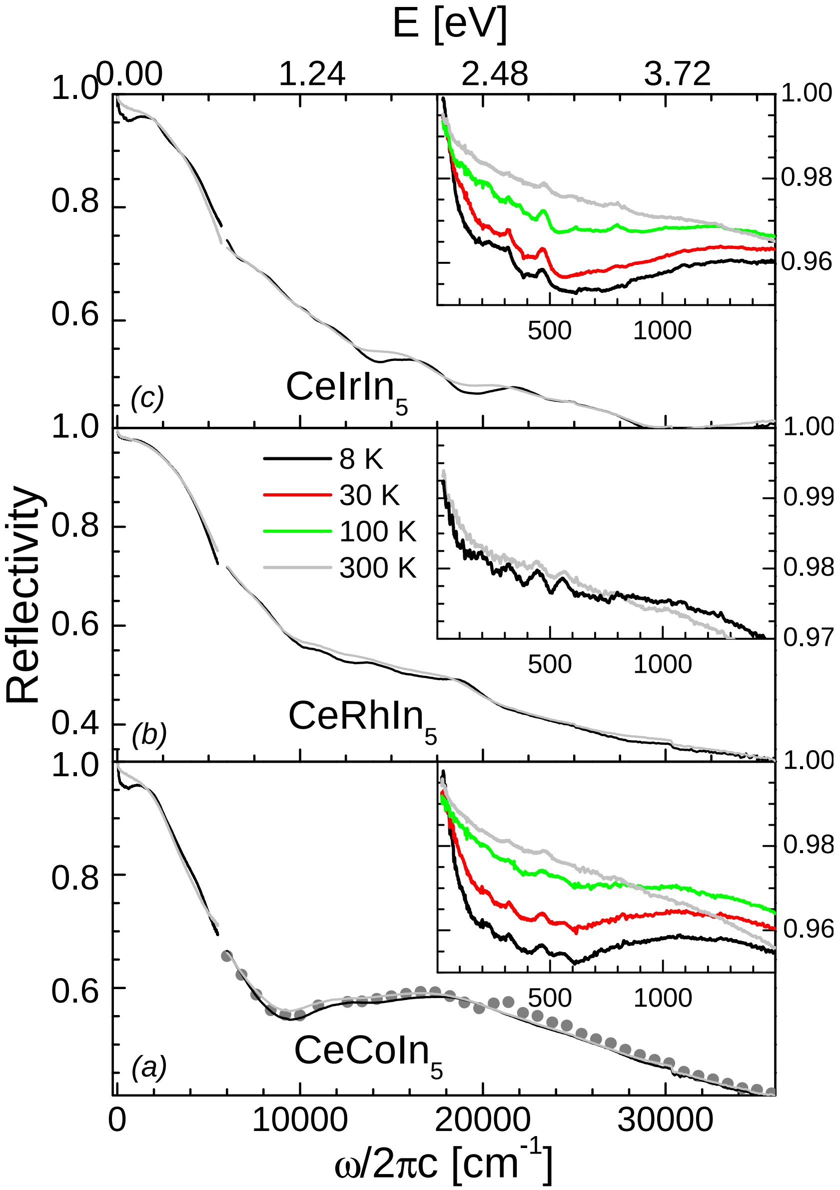

Figure 5.3: *Reflectivity of the different samples at several temperatures. Below 6000 cm^{-1}: measured. Above 6000 cm^{-1}: calculated from the dielectric function. The gray dots show the measured reflectivity of the ab-plane of CeCoIn$_5$. Insets: Reflectivity below 2000 cm^{-1}.*

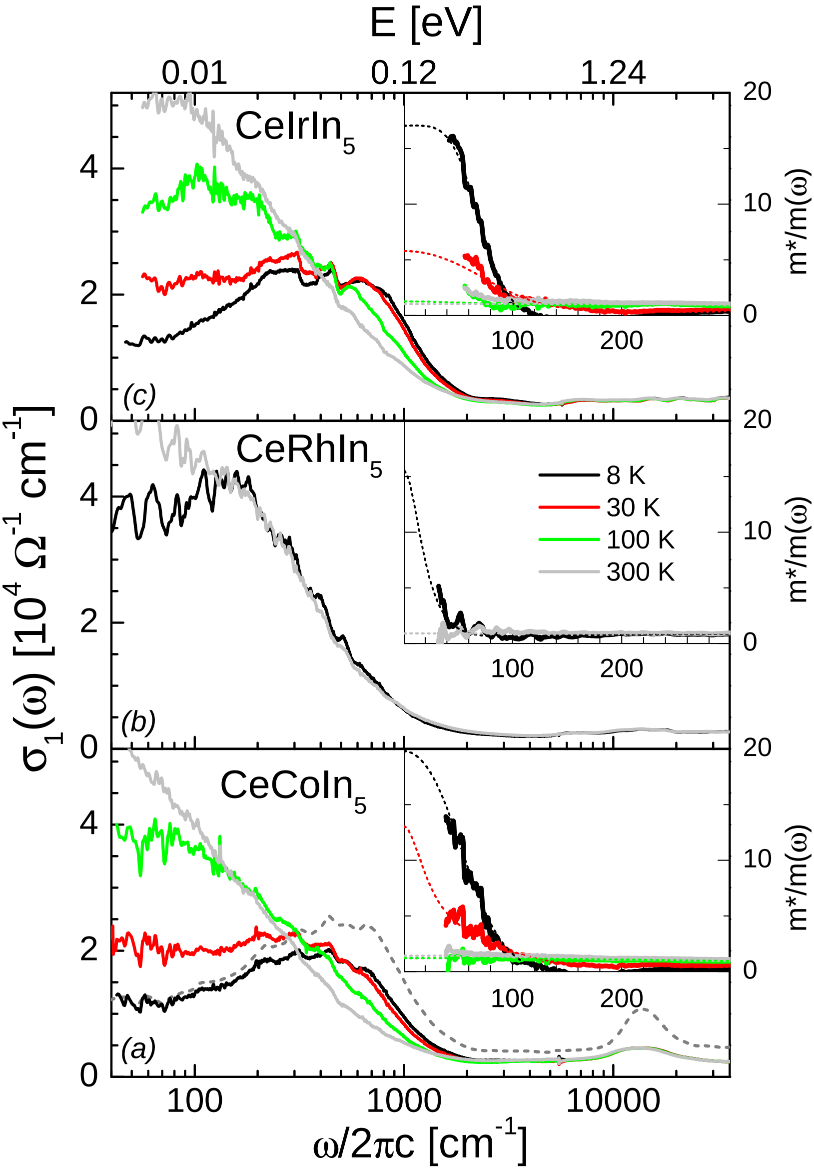

Figure 5.4: *Real part of the optical conductivity in the entire frequency range at several temperatures. The lower panel also shows the obtained $\sigma_1(\omega)$ if the high frequency reflectivity of Ref. [129] is used in the KK analysis (gray dotted line). Insets: Measured frequency dependent mass (solid lines) and obtained from a fit to the experimental data (dotted lines).*

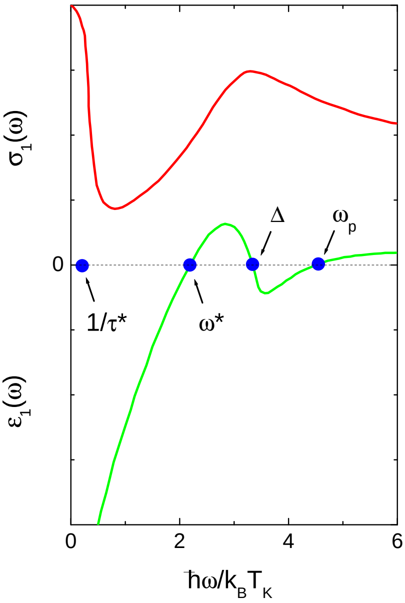

Figure 5.5: *Schematic representation of the optical conductivity in heavy fermion metals (from Ref. [136]). Referring to Fig. 1.9, the intraband transitions in the lower band produce the narrow Drude mode while the interband transitions between the two resulting bands produce the bump seen at higher frequencies.*

a result of the hybridization between the conduction electrons and the localized f-moments [17] (for a schematic representation of this situation see Fig. 1.9). The intraband transitions in the lower band produce the narrow Drude mode while the interband transitions between the two resulting bands produce the bump seen at higher frequencies [17, 131, 132, 136] (see Fig. 5.5). In the Rh compound these characteristics are less strong but still a decrease in the optical conductivity can be seen at low frequencies. Since this compound eventually becomes AF at 3.8 K, this seems to be the result of the competition between the magnetic ordering and the coherent state. We will discuss more about this point below.

When comparing our results for CeCoIn$_5$ with those of a previous report [129], we notice that both show the minimum in $\sigma_1(\omega)$ at the same position and a shoulder at 250 cm^{-1}. The later feature was interpreted as a Holstein band (an absorption corresponding to the bosons that couple the electrons in the SC state) inside of the gap which could be attributable to AF critical fluctuations [129, 127]. The argument for such assignment is that, in contrast with what has been seen in other heavy fermion systems [130], there is not a sudden decrease of the optical conductivity just below the peak originated by the transitions across

Table 5.1: *Characteristics parameters of CeMIn$_5$. T^* is taken from Refs. [127, 128]. T_{coh} was calculated from the DC resistivities of Refs. [116, 117, 118] while γ was taken from the same References. $m^\star/m$ has been calculated from spectral weight considerations.*

Sample	ω^* cm^{-1}	ω_1 cm^{-1}	T^* cm^{-1}(K)	T_{coh} cm^{-1}(K)
CeCoIn$_5$	140	200	31 (45)	31 (45)
CeRhIn$_5$	<100	<100	10 (15)	28 (41)
CeIrIn$_5$	120	220	14 (20)	36 (52)

Sample	N_{eff} (at 2000 cm^{-1})	$m^\star/m$ –	γ mJ mol^{-1} K^{-2}
CeCoIn$_5$	1.5	15	300
CeRhIn$_5$	1.8	13	400
CeIrIn$_5$	2.0	16	750

the hybridization gap. The interband transitions were related to a strong peak seen at 600 cm^{-1} which has less spectral weight in our experiments. Besides the understandable differences between different experimental sets, the origin of such large spectral weight could be due to an overestimation of the reflectivity in the visible range (where we used ellipsometry). To check this supposition, we have performed KK using our own reflectivity data and the reflectivity from Ref. [129] above 6000 cm^{-1}. The result is presented as the gray dotted line in Fig. 5.4(a). Such procedure gives more spectral weight at around 600 cm^{-1}. Therefore, the shoulder at 250 cm^{-1} most probably corresponds to transitions across Δ. This assignment is further supported below when we discuss the properties of $\epsilon_1(\omega)$.

5.2.3 Dielectric Function and Plasma Oscillation of the Condensate

The development of the hybridization gap can also be seen in the real part of the dielectric function at low frequencies (Fig. 5.6). As the temperature is lowered, $\epsilon_1(\omega)$ changes from purely metallic (monotonically decreasing) to a region with a maximum. At the lowest measured temperature, in the Co and Ir compounds, it even has two extra zeros whose values are given in Table 5.1. This behaviour shows the definitive establishment of the coherent state, a well known effect [17] that has been experimentally seen only recently [130]. The lowest zero, ω^*, may be thought of as the heavy fermion plasma mode [131] while the second one, ω_1, comes from the contribution of the interband transitions to $\epsilon_1(\omega)$. Since these transitions have a threshold energy Δ, ω_1 gives an estimate of the value of the hybridization gap. The shoulders seen at ~250 cm^{-1} in the Co and Ir compounds are above the gap and therefore most likely correspond to transitions across the gap. The dielectric function of CeRhIn$_5$, though it shows a maximum at 8 K, has not zero crossings indicating that, in contrast to the other compounds, the

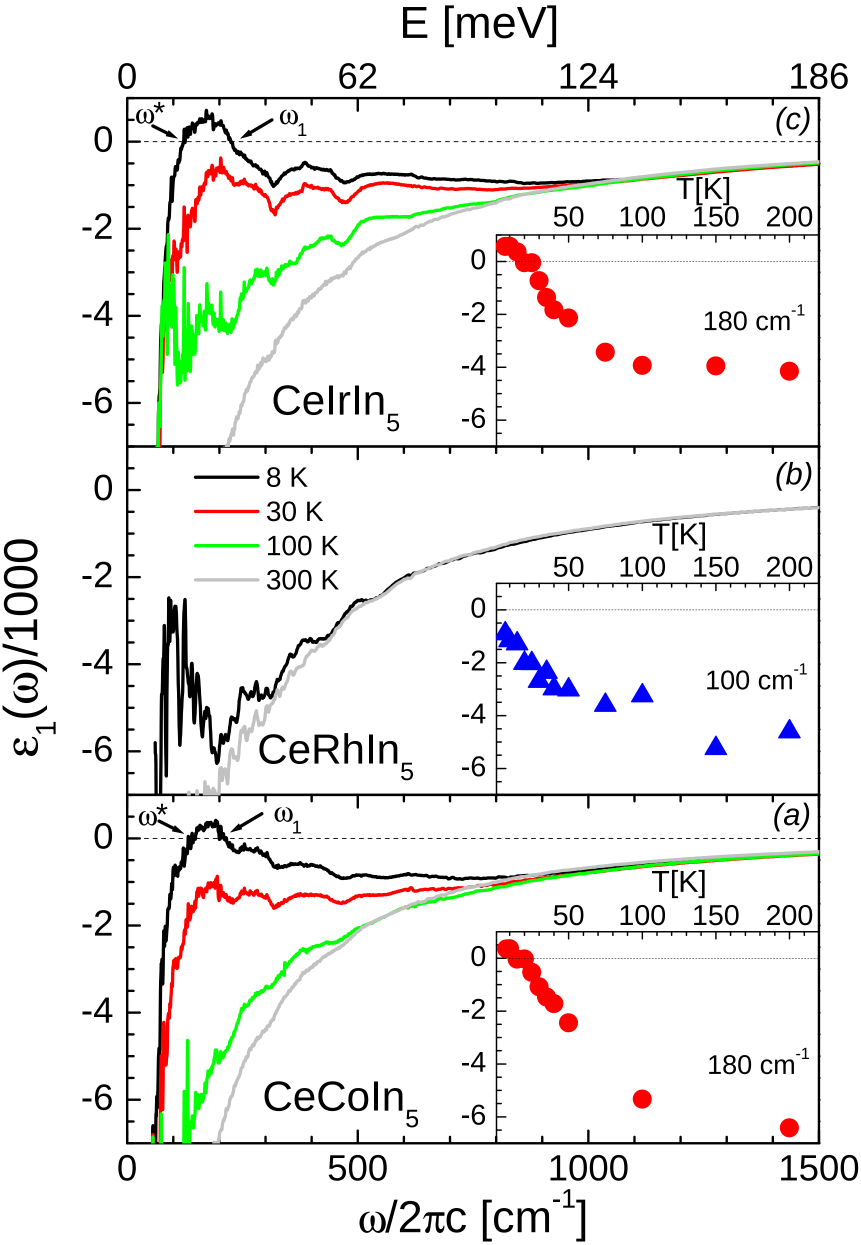

Figure 5.6: *Real part of the dielectric function in the infrared. The arrows indicate the zero crossings of $\epsilon_1(\omega)$. Insets: Temperature dependence of $\epsilon_1(\omega)$ at selected frequencies: 100 (triangles) and 180 (circles) cm^{-1}.*

coherent state is not completely formed. We interpret this phenomenon as the well known competition between magnetic ordering and the formation of the correlated state. Those systems that form a magnetically ordered state, usually present a smaller heavy fermion character[125]. To get more insight about this point, we analyze our results with the generalized Drude formulation (Eq. 2.24):

$$\sigma(\omega) = \frac{\omega_p^2}{4\pi} \frac{1}{1/\tau(\omega) - i\,\omega\, m^\star(\omega)/m}$$

where we used ω_p corresponding to the effective number of electrons, N_{eff}, at 2000 cm^{-1} and given in Table 5.1. The obtained frequency dependent mass, $m^\star(\omega)/m$, is plotted in the insets of Fig. 5.4. The increase of the effective mass is evident at low frequencies as soon as the temperature is lowered below T_{coh}. At the lowest measured frequency, the mass enhancement depends on the sample. However, from a fit to reflectivity, ellipsometry and DC conductivity, we estimate similar mass enhancements at $\omega \to 0$. Analogous results are obtained if the effective mass is calculated using spectral weight arguments (see Table 5.1) [†]. The difference between them is the energy range where the mass enhancement occurs, being much smaller for CeRhIn$_5$. In contrast, specific heat measurements [116, 117, 118] indicate (in the normal state) γ = 300, 400, and 750 mJ/(mol K^2) for Co, Rh, and Ir, respectively. At least for CeRhIn$_5$, as indicated by measurements of the de Haas-van Alphen experiment [139] and of the specific heat in magnetic field [134], this value of γ seems to be overestimated as the specific heat contains large contributions from magnetic interactions and not only from strong interactions. Another way to see the smaller heavy fermion character of CeRhIn$_5$ is by studying a simple relation obtained from the calculation of the dielectric function for the Anderson lattice [131]:

$$\omega^{*2} = 6(1 + n_f/n_c)T^{*2} \tag{5.1}$$

where n_c and n_f are the density of conduction and f-electrons. Since it is expected that these two quantities do not change in the CeMIn$_5$ (M = Co, Rh, Ir) group[‡] and given the values found for $\omega^\star$, the characteristic temperature T^* should be approximately the same for CeCoIn$_5$ and CeRhIn$_5$ but markedly decreased for CeRhIn$_5$. If we identify T_{coh} with T^*, this is indeed the case (CeRhIn$_5$ does not show a maximum in its resistivity but we have taken T_{coh} as the inflection point; see Fig. 1.10). From the study of the specific heat and the magnetic susceptibility [127, 128], different values of T^* were obtained (Table 5.1) contradicting our

---

[†] The mass enhancement is the ratio between the integrated spectral weights of the broad Drude peak at room temperature and the narrow peak at low temperatures. The limit of the integration was 2000 cm^{-1} for the room temperature peak. For the narrow peak the limits were 55, 35, and 60 cm^{-1} for the Co, Rh, and Ir compounds, respectively.

[‡] From a naive point of view this is expected since Co, Rh and Ir are isoelectronic and therefore no change in n_c is expected. As an experimental confirmation we remit to Table 5.1 where N_{eff} at 2000 cm^{-1} is shown.

observation of a completely settled coherent state in CeIrIn$_5$ at 8 K. It seems that more sophisticated calculations are needed to understand the various energy scales involved and how they impact the spectral weight transfer. Moreover, this effect in CeIrIn$_5$ also argues against some results that suggest that the f-electrons in this compound are more localized than those in CeCoIn$_5$. This latter point has been rather controversial [135].

5.2.4 Spectral Weight

The last point we want to discuss is the spectral weight contained by $\sigma_1(\omega)$ which was defined in Eq. 2.8 and we reproduce here:

$$N_{eff}(\omega) = \frac{mV}{\pi e^2} \int_0^{\omega} \sigma_1(\omega')d\omega'$$

The volume V was calculated from the lattice parameters given in References [116], [117], and [118]. N_{eff} is depicted in Fig. 5.7 and the temperature dependences at 400 and 2000 cm^{-1} are shown in its insets. For comparison purposes, the DC resistivities [116, 117, 118] are also shown in the insets. When the hybridization gap develops, spectral weight is removed from the low frequency part as evinced, for example, by the behavior of N_{eff} at 400 cm^{-1}. The spectral weight does not start recovering immediately above the gap but eventually does at an energy range much larger than the gap itself, ~2000 cm^{-1} (0.25 eV). Other Kondo systems show similar behavior. In particular, an interesting case is FeSi, where the spectral weight lost during the formation of the Kondo insulator state is transferred to an energy range on the order of several eV (see Chapter 4). The difference between the energies where the recovery of spectral weight takes place seems to be related with the nature of the local moments, d versus f-electrons. While the f-electrons form extremely narrow bands, the d-electrons form rather broad bands.

5.3 Optical Properties of LaRhIn$_5$

A common practice in the study of Kondo lattices is to replace the magnetic centers by a non-magnetic element. In the case of cerium-based compounds this is achieved by substituting it with lanthanum. In the CeMIn$_5$ (M = Co, Rh, Ir) system this procedure has proven to be very useful as the continuous substitution of Ce by La does not change important characteristics as the crystalline electric field or the Kondo coupling [127]. In this work we have measured the reflectivity (at different temperatures) and ellipsometry (at room temperature) of a single crystal of LaRhIn$_5$. The experimental results are summarized in Fig. 5.8.

Figure 5.8a and its inset show the reflectivity of this compound. In contrast with the magnetic lattices studied in the previous section, the reflectivity increases when lowering the temperature. This effect is common in metals due to the

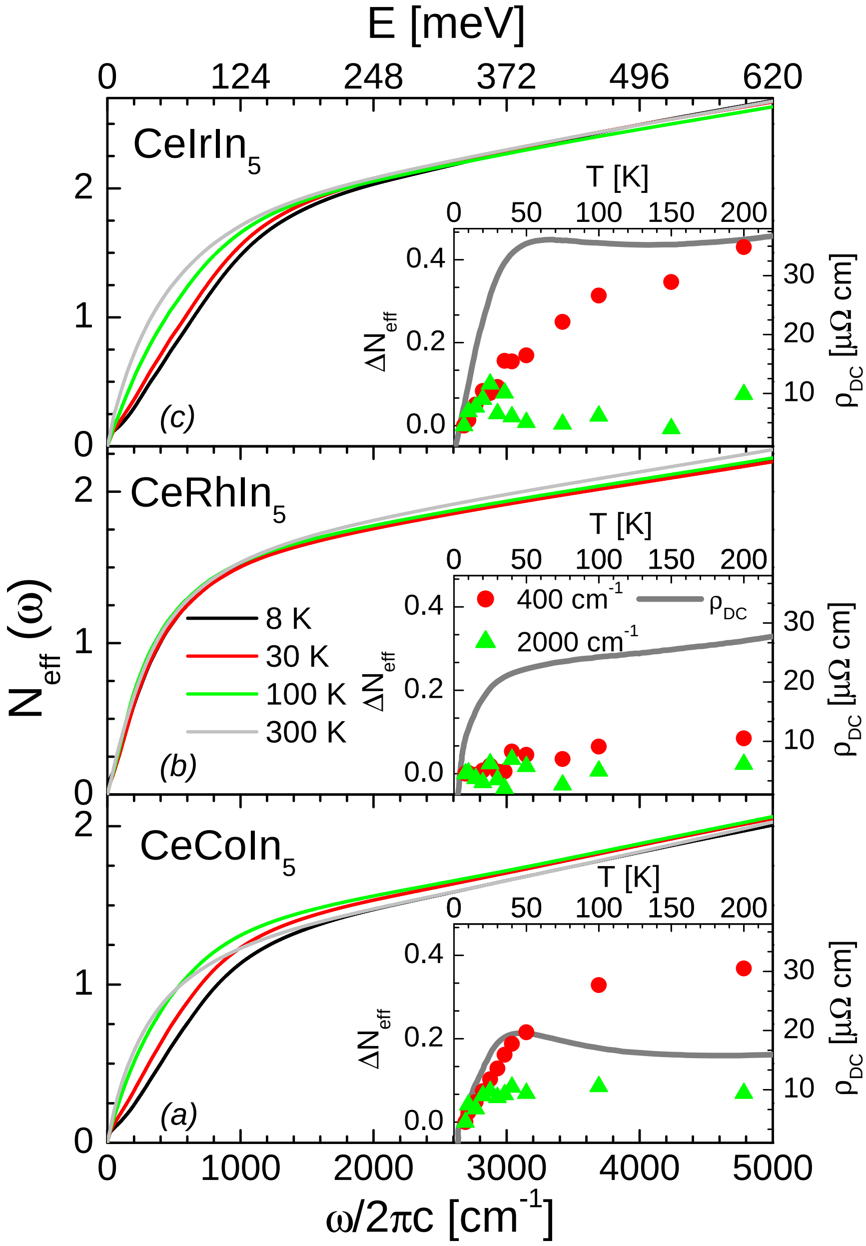

Figure 5.7: *Spectral weight of* $\sigma_1(\omega)$. *Insets: Temperature dependences of* ΔN_{eff} *at 400 (circles) and 2000 (triangles)* cm^{-1}, *and DC resistivities (gray line) from Refs. [116, 117, 118].*

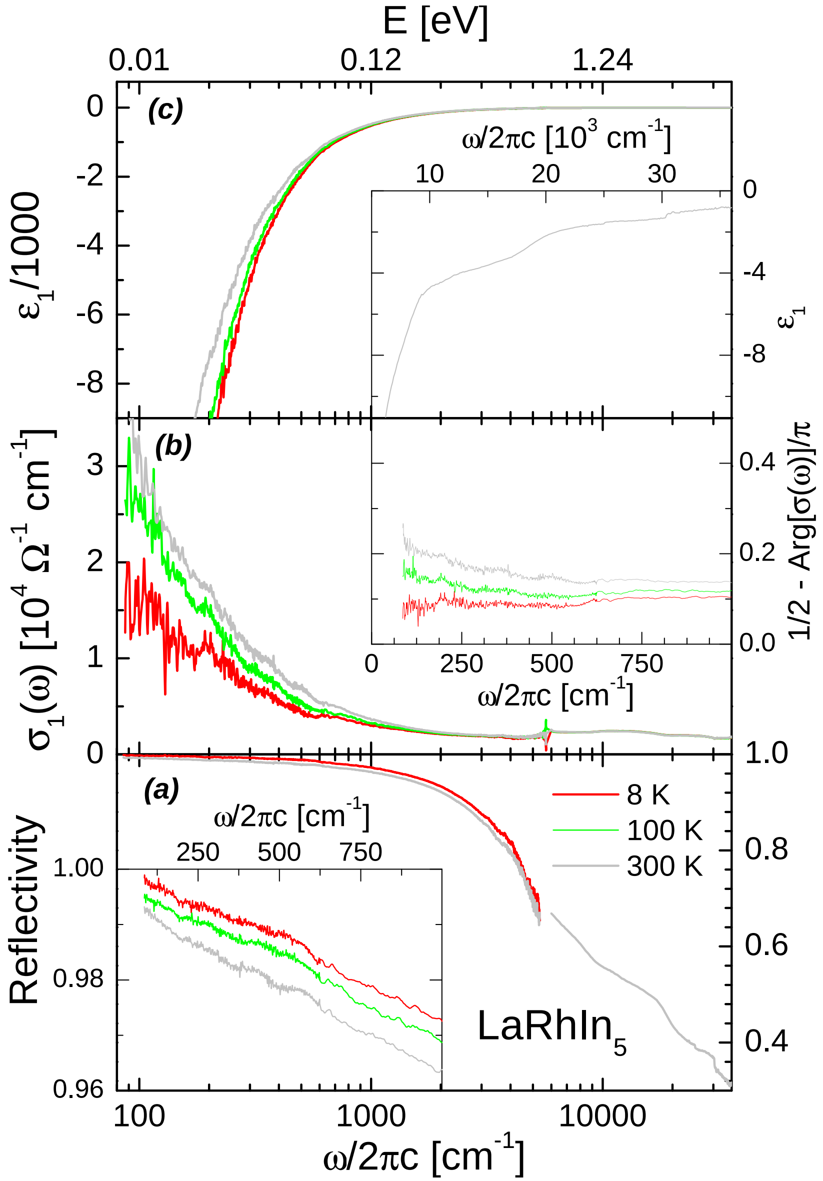

Figure 5.8: *Results of the optical spectroscopy performed in a single crystal of LaRhIn$_5$. (a) Measured reflectivity at several temperatures and room temperature reflectivity calculated from ellipsometry. Inset: Reflectivity below 1000 cm^{-1}. (b) Real part of the optical conductivity. Inset: Phase of the complex conductivity below 1000 cm^{-1}. (c) Real part of the dielectric function. Inset: Expanded view of $\epsilon_1(\omega)$.*

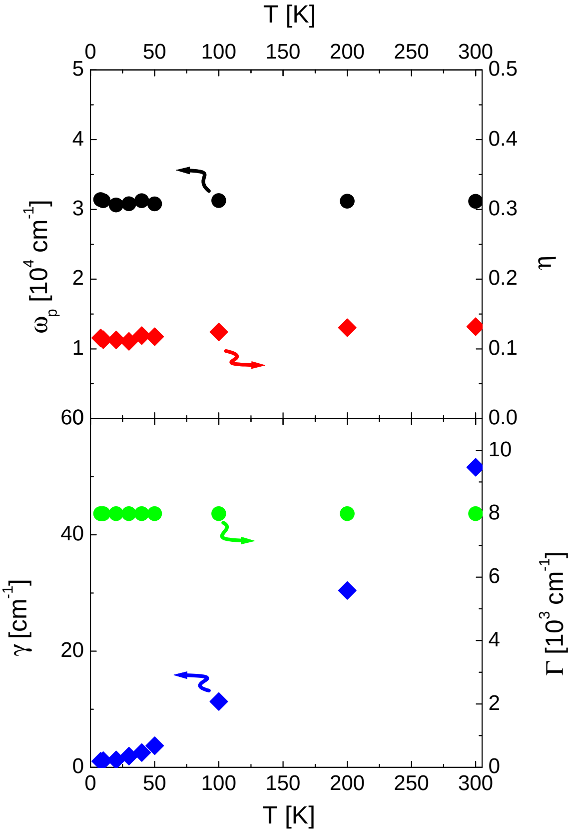

Figure 5.9: *Parameters used to fit the low frequency part of the optical properties. The parameter* Γ *was kept constant during the fit at different temperatures.*

reduction of the scattering rate. Both the real parts of the optical conductivity (Fig. 5.8b) and of the dielectric function (Fig. 5.8c) show that indeed the scattering rate is reduced. This can be seen from the fact that, at low frequencies, both decrease with decreasing temperature. In particular, $\epsilon_1(\omega)$ remains metallic down to the lowest measured temperature without the appearance of the maximum seen in the magnetic counterpart. Finally, the inset of Fig. 5.8b shows the quantity $\frac{1}{2} - \frac{\arg[\sigma(\omega)]}{\pi}$ which above above ~ 250 cm^{-1} reaches a plateau at around 0.1. According to the discussion in §2.4.2, this signals a departure from the Drude model. In the context of Eq. 2.20 this would mean that $\eta = 0.1$.

We have indeed fit reflectivity and ellipsometry data with the above mentioned equation. The results are depicted in Fig. 5.9. It is important to mention that, since the fit at different temperatures gives a large value for Γ, this parameter

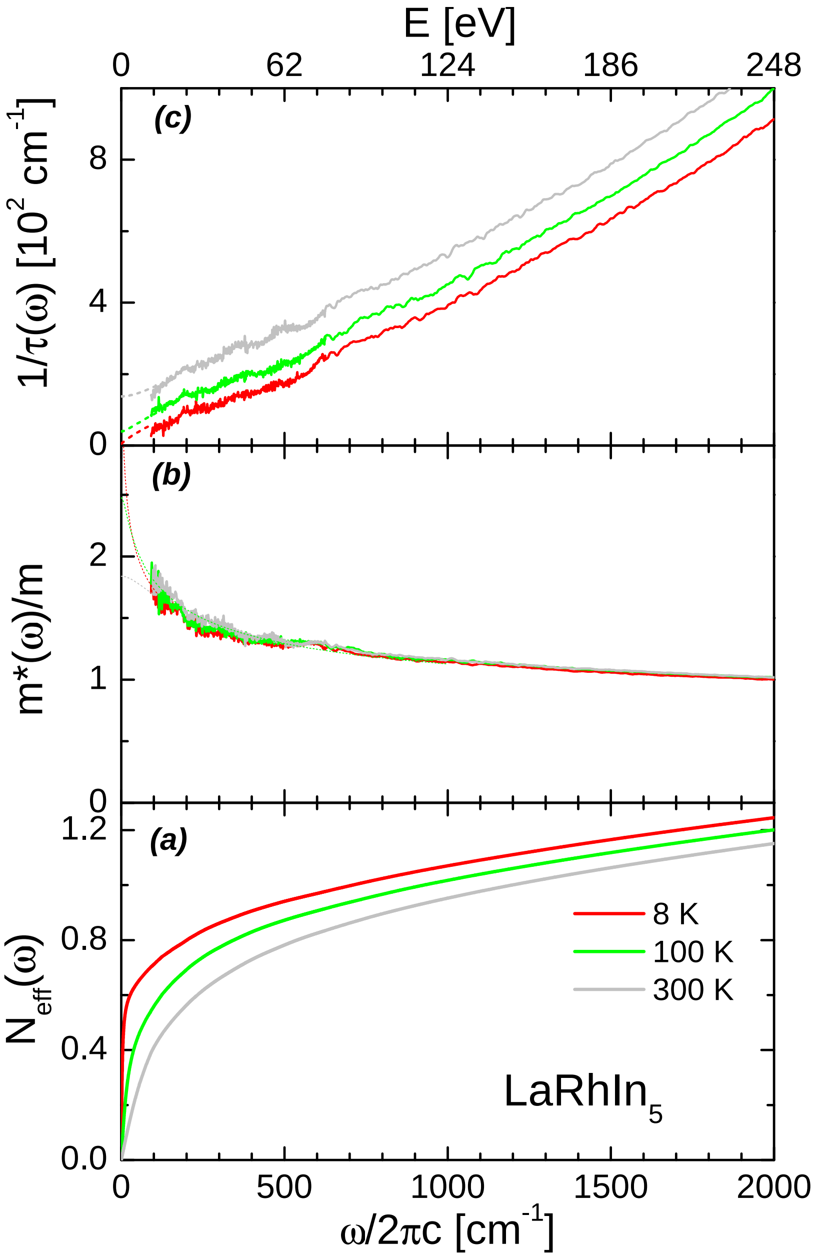

Figure 5.10: *(a) Effective number of carriers. (b,c) Frequency dependent mass and scattering rate.*

was kept constant at all temperatures. The results indicate that both, the plasma frequency, ω_p, and the exponent η do not show a strong temperature dependence. Moreover, the value of the later is ~0.1 as expected from the phase of the optical conductivity. In contrast, parameter γ has a strong temperature dependence. The situation is similar to what was found in MnSi.

For $LaRhIn_5$ we have also calculated the spectral weight and performed the extended Drude analysis. The former is shown in Fig. 5.10a where we have used the lattice parameters reported in Ref. [138]. As it happens in $CeMIn_5$, after a sharp raise, N_{eff} exhibits a plateau and reaches ~1.2 at 2000 cm^{-1}. At the same frequency, N_{eff} is ~1.8 in $CeRhIn_5$ (see Table 5.1), which is consistent with the fact that cerium has one more electron than lanthanum.

The results of the extended Drude analysis are given in Figures 5.10b-c. The fact that both, the mass enhancement and the scattering rate are not constant, indicate a strong deviation from the Drude response as it was concluded in the previous analysis of the phase of the optical conductivity. The extrapolation (dotted lines in 5.10b) gives an mass enhancement of 3. This is ~5 times smaller than the mass enhancement found in $CeRhIn_5$. Similar ratios have been found when comparing results of de Hass-van Alphen and heat capacity experiments [18]. The former gives a ratio of 7-9 for the cyclotron masses in the main bands. Heat capacity results, instead, give a ratio of ~9 between the γ-coefficients. The frequency dependent scattering rate depicted in Fig. 5.10c is quasi-linear at low frequencies. In comparison, the DC resistivity is linear from 300 down to ~ 20 K where it saturates[137]. This indicates a strong electron-phonon coupling which naturally leads to deviations from the Drude formulation[39].

5.4 Conclusions

In conclusion, we have presented optical measurements on one of the recently most studied families of heavy fermion systems, $CeMIn_5$ (M = Co, Rh, Ir). We have shown that in all the compounds presented here, the spectral weight is recovered in the same frequency range of about 0.2 eV which is larger than the hybridization gap. Moreover, we can directly see how the coherent state is quenched by a competing phenomenon: antiferromagnetism.

Finally, we have also performed optical experiments in one of the non-magnetic counterparts of this family, $LaRhIn_5$. None of the characteristic features of the heavy fermion systems has been found in this material. However, we were able to distinguish a strong deviation from the Drude formulation. Since the DC resistivity is linear, this can be an effect of a strong phonon-electron coupling.

Chapter 6

Phase Separation and Isotope Effect in $(La_{0.5}Pr_{0.5})_{0.7}Ca_{0.3}MnO_3$ Thin Films

The optical conductivities of films of $(La_{0.5}Pr_{0.5})_{0.7}Ca_{0.3}MnO_3$ with different oxygen isotopes (^{16}O and ^{18}O) have been determined in the spectral range from 0.3 to 4.3 eV using a combination of transmission in the mid-infrared and ellipsometry from the near-infrared to UV regions. We have found that the isotope exchange strongly affects the optical response in ferromagnetic phase in a broad frequency range, in contrast to the almost isotope-independent optical conductivity above T_C. The optical response is similar to the one extracted from measurements in polished samples and other thin films, which signals to the importance of internal strains. A qualitative explanation can be given in terms of the phase separation present in these materials.

6.1 Introduction

Few compounds manifest a so ample variety of states as the manganite perovskites when conditions such as magnetic field, temperature, or hole doping are changed. $La_{1-x}Ca_xMnO_3$, a particular well studied family of manganites, is an example of this. Its phase diagram (at ambient pressure and no magnetic field) is given in Fig. 1.11. As it becomes evident from the phase diagram, at low temperatures, the particular state of the manganites depends on the ratio of Mn^{+3} to Mn^{+4} (which is given by the hole doping x). Moreover, a given state also depends on specific particular lattice characteristics: Mn-O and cation-O bond lengths, and

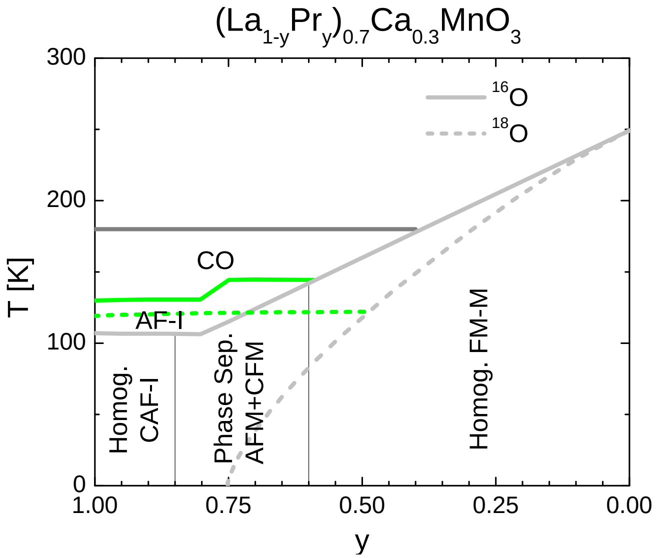

Figure 6.1: *Phase diagram of ($La_{1-y}Pr_y$)$_{0.7}$$Ca_{0.3}MnO_3$ (from Ref. [141] for ^{16}O and as suggested in Ref. [142] for ^{18}O).*

the cation-O-cation bond angles. These bond characteristics in turn depend on the average cation radius, $\langle r_A \rangle$.[24] At a given hole doping, the direct influence of $\langle r_A \rangle$ can be studied by replacing the rare earth with another. However, this replacement can also induce disorder if $\langle r_A \rangle$ exceeds a particular critical value.[140] ($La_{1-y}Pr_y$)$_{0.7}$$Ca_{0.3}MnO_3$ is particularly suitable to study the effect of the average cation radius as it always remains below the critical value inducing disorder.[141] Neutron diffraction experiments in this system[141] have permitted to construct the phase diagram shown in Fig. 6.1 (solid lines). At low temperatures, as the Pr concentration increases, the system goes from a homogeneous ferromagnetic metal to a homogeneous canted antiferromagnetic insulator. Between these two extremes, the neutron diffraction data[141] suggest the presence in the system of two different phases, one is antiferromagnetic while the other is canted ferromagnetic. Phase separation indeed seems to be a common feature of strongly correlated systems (see Ref. [26] and references therein). For example, the double-exchange model (which is recognized as describing the main properties of the manganites) has a natural tendency to phase separation at low doping.[26, 23, 29] The regions formed in this way are one of an undoped antiferromagnet and one of higher electron (or hole) concentration which is ferromagnetic (or strongly canted) and metallic.[26] However, long-range Coulomb forces compete against phase separation and the regions are broken in small pieces.[26, 23] It is also important to mention that there can be also phase separation between electron rich regions and charge ordered regions. [26] Several experimental techniques seem to confirm the existence of phase separation in the manganites (see references cited in Refs. [26] and [23]).

Recently, the effect of oxygen isotope substitution ($^{16}O \rightarrow {}^{18}O$) has been studied in various members of the $(La_{1-y}Pr_y)_{0.7}Ca_{0.3}MnO_3$ family. [142, 143] At high temperatures there are no appreciable differences between the two samples, their lattice parameters, [144] and DC conductivities [142, 143] are the same. At low temperatures, the situation is different. In particular it was found that for $y = 0.75$ the isotope substitution induces a metal-insulator transition.[143] This phenomenon could be naturally explained in the phase separation scenario.[26] As seen in Fig. 6.1, $(La_{0.25}Pr_{0.75})_{0.7}Ca_{0.3}MnO_3$ (with ^{16}O) seems to be in a region of phase separation. Then, the small changes produced by the isotope substitution would favor one phase over the other producing the metal insulator transition seen in Fig. 6.1. The isotope effect has also been studied in thin films of $(La_{0.5}Pr_{0.5})_{0.7}Ca_{0.3}MnO_3$ grown in either $LaAlO_3$ (LAO) and $SrTiO_3$ (STO). [146, 145] For the films grown in LAO, the isotope substitution produces a metal-insulator transition similar to the one seen in ceramic samples of $(La_{0.25}Pr_{0.75})_{0.7}Ca_{0.3}MnO_3$. [145, 146] For those grown in STO, the behaviour is qualitatively the same in samples with both isotopes. However, films with ^{18}O exhibit a much lower T_C and the value of the DC conductivity (σ_{DC}) at low temperatures is one order of magnitude lower than those containing ^{16}O. These differences arise from the different strains they support due to mismatches between the lattice parameters of the film and the substrate. [145] When grown in LAO, the films are contracted in-plane but stretched perpendicularly. The opposite is true for films grown in STO. These deformations are reflected in the magnitude of the Mn-O-Mn bond angles. Compared to the ceramic samples, this angle is increased for films in STO and decreased for LAO. This structural difference put the films grown in LAO at an angle closer to the critical value corresponding to localization of carriers (remember that the conduction bandwidth depends on the cosine of the Mn-O-Mn angle). [145]

Optical spectroscopy has played an important role in studying the physics driving the behavior of manganites. [2] It has also offered some indications of phase separation occurring at some specific concentrations. [23] For example, let us consider the optical spectra of $La_{7/8}Sr_{1/8}MnO_3$ [147] which remains insulating even below T_C and does not show any Drude contribution. It was found that below T_C a mid-infrared (MIR) peak appeared at around 0.4 eV without changing its position. [147] This peak was assigned to a small polaron absorption (small polarons are strongly confined and, therefore, are expected to produce only a small coherent contribution [148]). Moreover, it was noticed that the temperature dependence of its spectral weight resembles a percolation-type transition. [147] Regarding this point, Moskvin et al. [149] have been able to describe the temperature dependence of the optical conductivity in this compound by using an effective medium approximation in which the manganite is considered to have metallic regions (assumed spherical for simplicity) in an insulating matrix

($LaMnO_3$). In this approximation the MIR peak is a geometric resonance whose position is mainly determined by the shape of the metallic regions. [149] This would explain the seemingly fixed position of this peak. Such MIR peak has also been seen in the FM metallic part of the phase diagram. [150, 151, 152] It is already visible at high temperatures but below T_C its intensity increases being also accompanied by a narrow Drude peak. This behaviour suggested the change from a small to a large polaron. [150] However, more recently, optical experiments performed also in reflectivity configuration but on cleaved samples in the metallic state [153], have questioned the presence of the narrow and the MIR peaks (the other optical experiments were obtained in either polycrystalline or single crystal samples whose surface was polished prior to the experiments). The experiments on cleaved samples show, in contrast, the development of only a broad zero-centered peak (the specific characteristics of this mode do not correspond to a simple Drude formulation). The difference in the results emphasize the sensitivity of the manganites to static imperfections and/or structural strain. [153]

Optical experiments in thin films have also shown the presence of a narrow Drude-like mode and a MIR peak in FM-metallic samples (see, for example, Refs. [154] and [155]). These MIR peaks have also been assigned to polaronic absorptions. Particularly, it was possible to distinguish between small and large polarons in $La_{2/3}Ca_{1/3}MnO_3$ and $La_{2/3}Sr_{1/3}MnO_3$, respectively. [155] In contrast to the work of Kim et al.[150] (discussed above), Hartinger and collaborators made the assignment by fitting the optical conductivity to the corresponding theoretical expressions. [155] Evidence of phase segregation has also been inferred from measurements of the absorption coefficient in manganite thin films (see Refs. [156, 157, 158] and references therein). One of the main points in such studies is the appearance, at high carrier concentrations, of low energy absorptions (below 3 eV) ascribed to localized states. Such states have been interpreted in a cluster model [156] assuming the presence of electron and hole rich clusters. Transitions in this clusters produce these MIR absorptions (at energies $\Delta_{e,h}$) which in turn produce a common band at $\Delta_M = c_h \Delta_h + c_e \Delta_e$ ($c_{e,h}$ are the concentrations of the electron and hole clusters). [156] These bands have not been seen in reflectivity experiments since, it is argued, [158] they have low intensity and would be seen only in transmission experiments.

In this chapter we will elaborate on the points discussed above based on optical experiments performed on films of $(La_{1-y}Pr_y)_{0.7}Ca_{0.3}MnO_3$ ($y = 0.5$) containing two different oxygen isotopes. We will see how the isotope substitution produces changes in the optical conductivity at energies much larger than the phonon region. Both samples show a strong MIR infrared peak whose intensity decreases when temperature is increased. The spectral weight lost by this peak is mainly transferred to a peak lying at around 1.5 eV. By a detailed study of their temperature dependence we will argue that this behavior is consistent with a phase separation.

6.2 Experiment

6.2.1 Sample Preparation

Thin films of $(La_{0.5}Pr_{0.5})_{0.7}Ca_{0.3}MnO_3$ were grown on $SrTiO_3$ using the aerosol MOCVD technique (for details in the preparation and characterization see Ref. [145]). The films obtained had a nominal thickness of 60 nm. For the isotope exchange two strips of 1×8 mm^2 were annealed simultaneously in different atmospheres. One was heated in a $^{16}O_2$ atmosphere, while the other was heated in an oxygen atmosphere containing 85% of $^{18}O_2$. Hereafter, these samples will be referred as S16 and S18, respectively. As mentioned in the introduction, the XRD analysis shows that the films are highly strained. [145] Since the STO lattice constants are larger than the film, it produces an in-plane expansion of the perovskite cube. In contrast, perpendicularly to the plane, the film is contracted. In this conditions, a buckling of the MnO_6 octahedrons is expected. [145]

6.2.2 Optical Experiments

Transmission

In the frequency region [1000 - 5500] cm^{-1} the transmission of the samples was measured using a Bruker 113v FT-IR spectrometer. Below this frequency the STO substrate is not transparent. At room temperature the absolute transmission was measured while only the transmitted intensity was measured at different temperatures. For the temperature dependence a home-built cryostat was used, the special construction of which guarantees a stable and temperature independent optical alignment of the sample. The measured intensities where then normalized to the room-temperature transmission. The results of these measurements are summarized in Fig. 6.2.

Substrate

The optical properties of the STO substrate, at room temperature, were determined below 6000 cm^{-1} using the combination of reflectivity and transmission. The complex dielectric function was then determined by numerically inverting the corresponding Fresnel equations. [49] The results are shown in the inset of Fig. 6.3. Moreover, the temperature dependencies of transmission and reflectivity were measured. However, the dependence is much smaller than the changes in the films. As an example, the transmission of STO at 2000 cm^{-1} (displaced down by 30%) is shown in the inset of Fig. 6.2. Therefore, in the calculations described below, only the room temperature dielectric function of the substrate was used. Above 6000 cm^{-1}, we have used the data of Ref. [159] which is also plotted in the inset of Fig. 6.3.

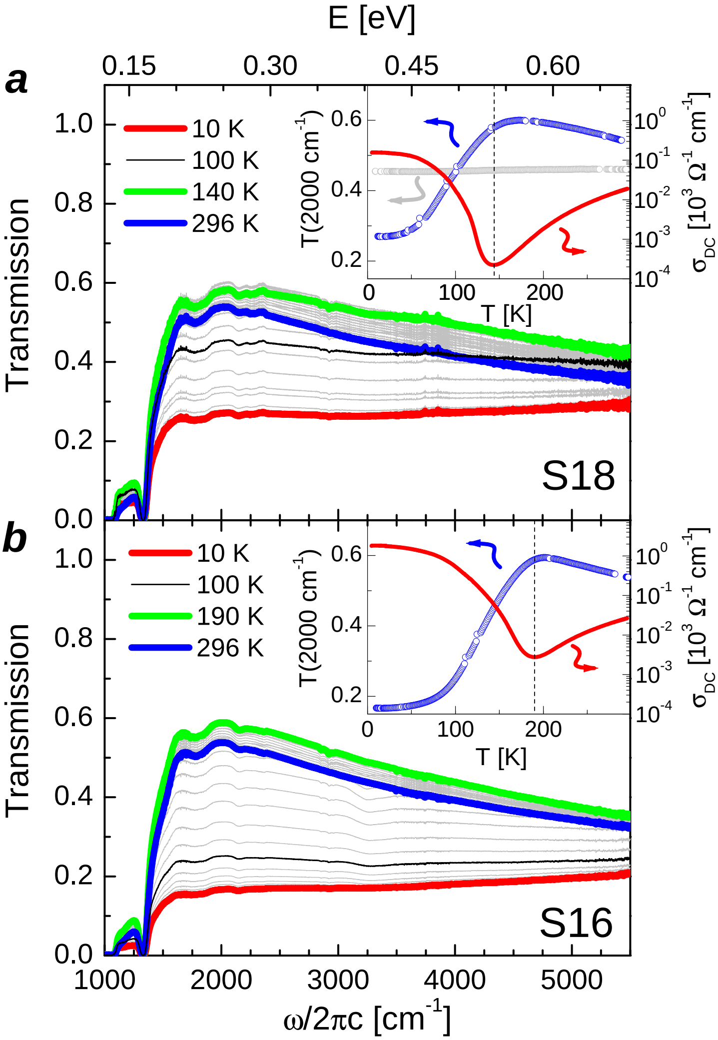

Figure 6.2: *Measured transmission between 10 and 296 K every 10 K in films of* $(La_{0.5}Pr_{0.5})_{0.7}Ca_{0.3}MnO_3$ *containing* ^{16}O *and* ^{18}O *(labeled hereafter S16 and S18, respectively). The highlighted transmissions correspond to the highest and lowest measured temperatures and to the minimum seen in* σ_{DC} *Insets: Temperature dependence of the transmission at 2000* cm^{-1} *and of the DC conductivity, both measured during heating with no magnetic field. The vertical dotted line signals the minimum in* σ_{DC} *and which is associated with the entrance to the ferromagnetic state (we will refer to it as* T_C*). The inset of the upper panel also shows the temperature dependence of the transmission (shifted down by 30%) of an STO substrate. It is clear that the temperature effects are related solely with changes in the films.*

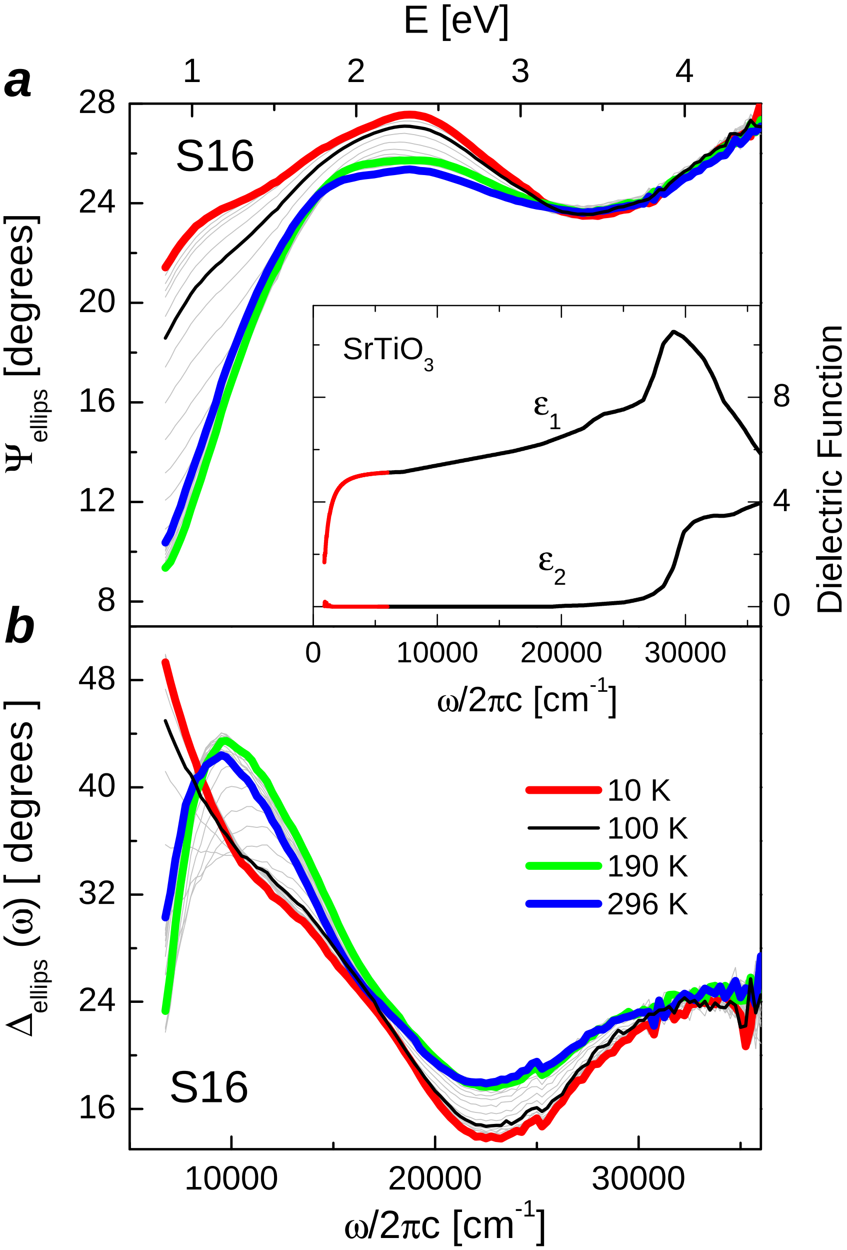

Figure 6.3: *Parameters Ψ and Δ for S16 as obtained directly from ellipsometry between 10 and 296 K every 10 K. Inset: Complex dielectric function of STO, measured (below 6000 cm^{-1}) and from Ref. [159] (above 6000 cm^{-1}).*

Ellipsometry

Ellipsometry of the samples was performed with a commercial (Woollam VASE32) ellipsometric spectrometer in the range 6000 to 36000 cm^{-1}, using an ultra high vacuum cryostat. The ellipsometry experiment was carried out in a grazing reflectivity configuration at an angle of incidence of 80°. This experiment gives the ellipsometric parameters Ψ and Δ that define the ratio between the Fresnel reflection coefficients for the s- and p-polarized light, $\rho \equiv \frac{r_p}{r_s} \equiv \tan(\Psi)\mathrm{e}^{i\Delta}$. As an example of the results obtained in this experiment we show in Fig. 6.3 the corresponding ellipsometric parameters for S16. The ratio ρ, obviously, depends on the dielectric functions of both, substrate and film. Since we know the optical properties of the substrate, the complex dielectric function of the film, $\epsilon(\omega) = \epsilon_1(\omega) + i(4\pi/\omega)\sigma_1(\omega)$, was obtained by inverting numerically the analytical expression corresponding to ρ for a two layer system. [49] At different temperatures we used only the room temperature data for the substrate and also assumed a semi-infinite substrate. The real part of the optical conductivity, $\sigma_1(\omega)$, obtained from this inversion is shown in Fig. 6.4.

Optical Conductivity in the MIR Range

Below 6000 cm^{-1}, the complex dielectric function of the film was obtained using a similar approach to the one used in our previous experiments (see Chapter 2). As a first step we performed a simultaneous fit to the DC conductivity, transmission of the film+substrate system (via the Fresnel equations), and the dielectric function of the film at higher frequencies. The fit used a model dielectric function which is the combination of one Drude and a limited number of Lorentz oscillators (Eq. 2.19). This Drude-Lorentz (DL) fit sets extrapolations below and above the measured range. Finally, a procedure *à la* Kramers-Kronig (KK) is used where every detail of the the measured data is reproduced by introducing an arbitrary number of oscillators on top of the previous fit. [50] The real part of the optical conductivities obtained in this way are also plotted in Fig. 6.4. As in the usual KK transformation, the obtained optical conductivity depends on the extrapolations. Since we have used the dielectric function obtained from ellipsometry at a rather broad energy range, the most influential are the low frequency extrapolations. To estimate the uncertainties coming from this factor, we have repeated the procedure just described using different extrapolations (all of them congruent with the DC conductivity). The associated error bars are small for $\sigma_1(\omega)$ though rather large for $\epsilon_1(\omega)$. This is not a surprise since the transmission is mostly determined by the absorptive part of the optical conductivity, $\sigma_1(\omega)$. Moreover, we have repeated the same calculations assuming an error as large as 5% in the measured transmission. The total uncertainty related with both sources of errors is indicated by the error bars of Fig. 6.4.

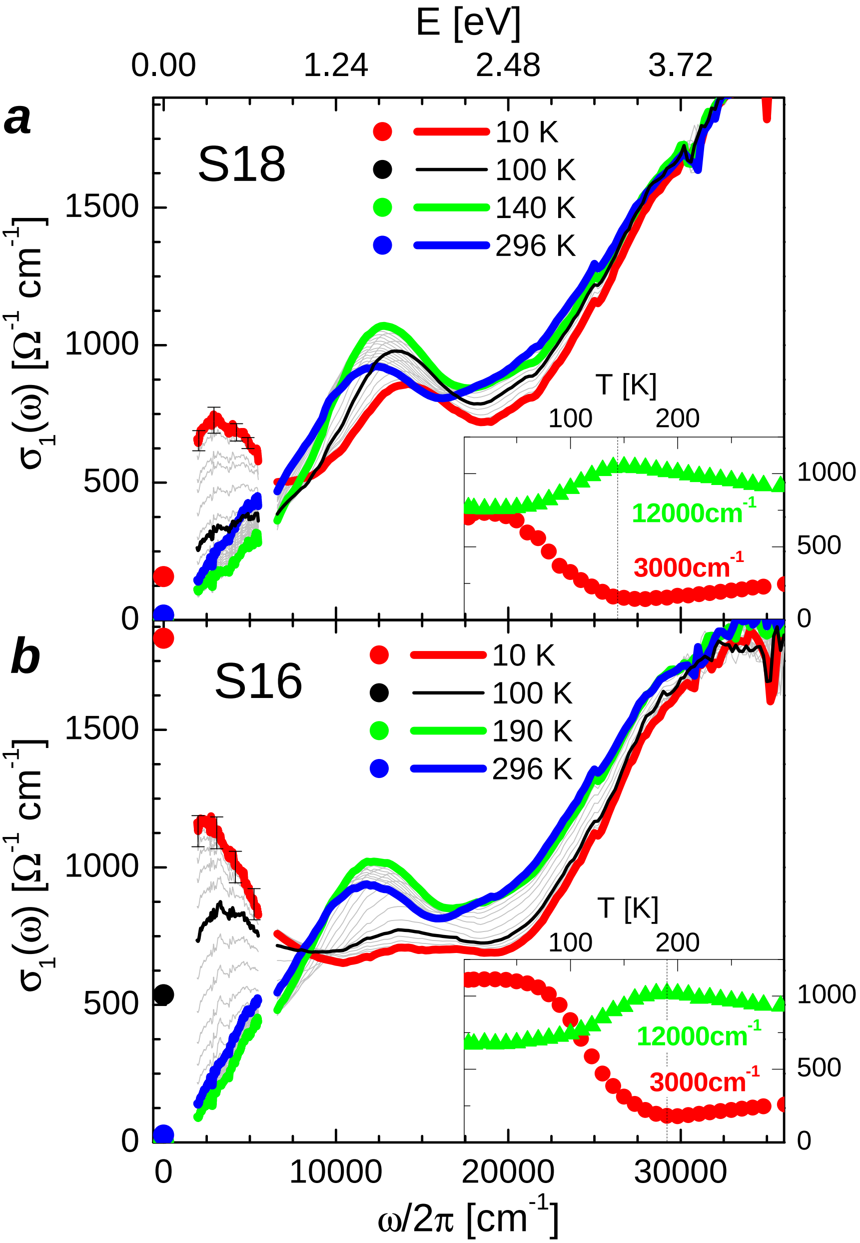

Figure 6.4: *Optical conductivity of the S16 and S18 samples between 10 and 296 K every 10 K. Circles at the far left represent DC conductivities. Insets: Temperature dependencies of the optical conductivity at two selected frequencies.*

Table 6.1: *Parameters, in* cm^{-1} *(eV), corresponding to the oscillators used to describe the optical conductivity of the two films at 10 K.*

Sample	$\omega_{p,1}$	Γ_1	$\omega_{o,2}$	$\omega_{p,2}$	Γ_2	$\omega_{o,3}$	$\omega_{p,3}$	Γ_3
S16	8320	632	2853(0.35)	21154	7725	13155(1.63)	12872	9300
S18	2449	632	3054(0.38)	15999	6132	13559(1.68)	18091	9426

Sample	$\omega_{o,4}$	$\omega_{p,4}$	Γ_4	$\omega_{o,5}$	$\omega_{p,5}$	Γ_5
S16	32236(3.99)	29631	16843	43600(5.41)	55234	47633
S18	30930(3.84)	31347	18300	43600(5.41)	53329	24540

6.3 Results and Discussion

6.3.1 Transmission

The measured σ_{DC} in both films shows hysteresis, being rather large in the S18 sample. [145] This gives an indication of phase separation. The DC conductivities plotted in the insets of Fig. 6.2 correspond to heating cycles. This is the mode in which the transmissions of both films were measured. From the main panels of Fig. 6.2 we can see that, starting from the lowest temperature, the transmission of both samples increases. Then, it reaches a maximum at around the same point as σ_{DC} and the decreases again. To exemplify in a better way the temperature dependence, we plot the transmission at 2000 cm^{-1} in the insets. This temperature behavior correlates with the changes in σ_{DC}. However, a closer look at the figures indicate that the maxima of transmission occur at a slightly higher temperature than those in the DC conductivity. Although the reason is not clear, it could be related with the fact that a CO phase appears at higher temperatures than T_C [141] (see also Fig. 6.1 keeping in mind that it was established for bulk samples).

6.3.2 Optical Conductivity and Drude-Lorentz Fit

The obtained optical conductivities are shown in Fig. 6.4. At room temperature, both samples have an almost identical $\sigma_1(\omega)$, which contrasts with the differences appearing at low temperatures (see also Fig. 6.5). As an example of the changes with temperature see the insets of Fig. 6.4 where we plotted $\sigma_1(\omega)$ at two different frequencies. Notice that at 3000 cm^{-1} the optical conductivity increase below T_C is larger in the more metallic S18 sample. On the other hand, the temperature dependence at 12000 cm^{-1} is opposite to that at 3000 cm^{-1} which indicates that there is a transfer of spectral weight between these two regions. Other point to notice is that the frequency dependence of the optical conductivity, at different temperatures, is similar to that one obtained from reflectivity measurements in polished samples. [147, 150, 151, 152, 165] In particular, both samples exhibit an MIR peak which seems to be accompanied by a narrow zero-frequency mode in the S16 sample.

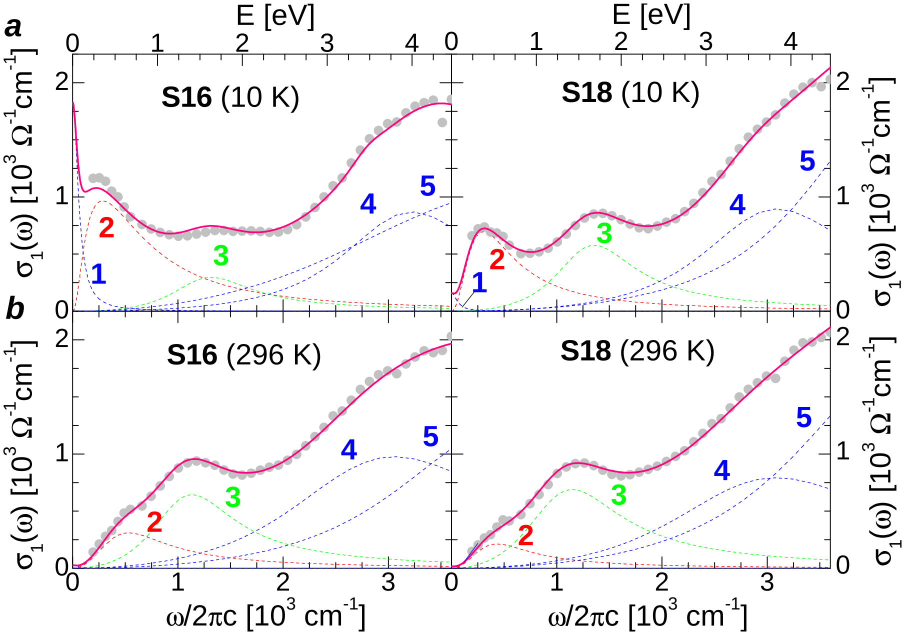

Figure 6.5: *Results of the Drude-Lorentz fit. Optical conductivity (gray circles), fit (solid line) and individual oscillators (dashed lines) at (a) 10 K and (b) room temperature.*

The multiple oscillator fit described in Section 6.2.2 permitted us to recognize the different contributions to the optical conductivity and their temperature dependencies. At all temperatures and in both samples, we used the same number of oscillators. For example, at 10 and 296 K, the oscillators used in the fit can be seen in Fig. 6.5. Furthermore, the fit parameters at 10 K are given in Table 6.1. We have to mention that during the fitting routine we have kept the width of the Drude peak constant at 632 cm^{-1} since we cannot access its exact shape at low frequencies. This is an *ad hoc* assignment but it is in agreement with observations in polished samples [150] and thin films [155]. Nevertheless, the precise width does not affect the main conclusions presented below. The same applies for the last peak which falls outside our spectroscopic window but it is necessary for an acceptable fit. For this oscillator we fixed its position.

At first sight, the scenario that arises from the DL fit is similar to the one described by Noh et al. [160] However, notice that some of these features, particularly the narrow Drude peak, has not been seen in experiments performed in cleaved single crystals. [153, 161, 162]. These differences in the optical response have been ascribed to static imperfections and/or structural strain. The latter seems to be the most probable cause since the films studied here are under large

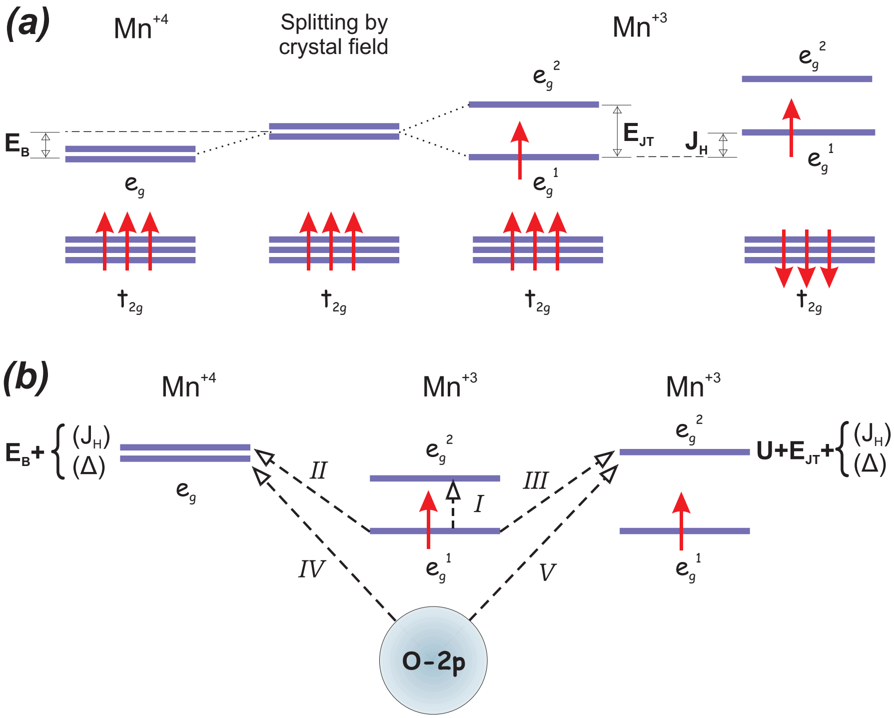

Figure 6.6: *Energy diagram of the manganites (adapted from Refs. [19] and [154]). (a) The Mn-d levels, due to crystal field, are split in the so-called* t_{2g} *and* e_g *levels. If the* e_g *level is occupied, this state is further split by* E_{JT}*, due to distortions of the surrounding O atoms. If the* e_g *level is empty, its original energy can be shifted by* E_B *due to a "breathing" distortion (i.e. a distortion that couples to changes in the occupation density of* e_g *in a short time scale). Furthermore, the* e_g *level can correspond to spin states either parallel or antiparallel to* t_{2g}*. In the latter case, the energy of* e_g *is higher by an energy given by the Hund's coupling,* J_H*. We have plotted this situation for the case of an occupied* e_g *level. (b) Possible transitions occurring in the manganites. The different levels shown here correspond to different Mn atoms. The initial states are depicted in the center of the figure (an occupied* e_g *level and a filled O-2p band). To determine the final energies, one has to take into account the different situations noted before, the origin of the excited electron (either coming from an* e_g *or an O-2p state), and the fact that putting an extra electron in an already occupied* e_g *level costs an energy* U*. When excited electron comes from an O-site, an energy* Δ *has to be added.* Δ *is the charge transfer energy.*

strains (see Section 6.2.1). In the following, given the extraordinary similarity between the results of the present work and those performed in polished samples and thin films, we will discuss the optical properties in the light shed by those experiments. Moreover, to make the discussion easier to follow, in Fig. 6.6a we reproduce the well known energy diagram proposed for the manganites (see the figure caption for details). [19, 154] The possible transitions between those states are depicted in Fig. 6.6b. Referring to this figure, the transitions are:

- *I:* A transition between different e_g levels at the same atomic site. This transition is not dipole allowed and, therefore, is expected to be weak. [154, 163] However, it has been argued [160, 164] that due to the strong hybridization between the e_g and O-2p bands, and the strong local distortion of the Mn-O octahedra, these transitions can be allowed.
- *II, III:* Interatomic $e_g \rightarrow e_g$ transitions, i.e. from a Mn^{+3} ion to either another Mn^{+3} ion or to a Mn^{+4} ion.
- *IV, V:* Charge transfer transitions, O-2$p \rightarrow e_g$.

Now we address the possible assignments to the peaks recognized by the DL-fit. Let us start from the high frequency features. The strong absorption starting at 2.5 eV is represented by peaks number 4 and 5 in Fig. 6.5 which, taken together, they have a small temperature dependence. There is a general consensus that this feature stems out the charge-transfer transitions from the O-2p band to bands of Mn-d character, namely the unoccupied e_g levels. [154, 160, 165] Notice that experiments in cleaved samples suggest that this band is split and that the O-2p electrons can also reach t_{2g} levels. [161]

Before discussing the possible provenance of peaks 2 and 3, let us notice several points regarding these peaks. First, in most of the experiments, these two features are not so well defined as in the present case. In fact, the sharpness of these features allowed us to extract their temperature dependencies rather unambiguously, especially below T_C. Second, these two peaks are closely related as it is shown by their temperature dependence in Fig. 6.7. At high temperatures, in both samples, only peak 3 is clearly visible and does not significantly change down to T_C. From this point its intensity decreases in favor of peak 2. This transfer of spectral weight between these two peaks is accompanied by a displacement, to low frequencies in the case of peak 2 and to high frequencies in peak 3. This process stops at around 100 K in S16 and 75 K in S18. Third, the less metallic sample, S18, shows a lower decrease (increase) in the intensity of peak 3 (2) at low temperatures. This points to the fact that peak 3 (2) is favored in the insulating (metallic) state.

The assignment of peaks number 2 and 3 (Fig. 6.5) is an ongoing debate. [154, 153, 168, 164] In part, this is due to the fact that in some experiments there is no clear difference between them. In the insulating phase all manganites undoubtedly present a large peak at around 1.5 eV. When decreasing temperature,

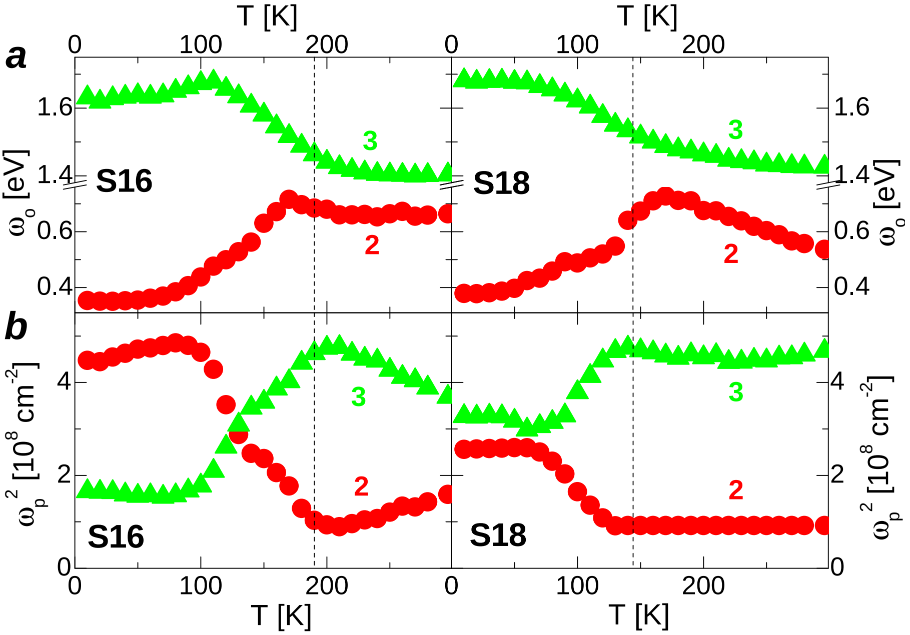

Figure 6.7: *Temperature dependence of the (a) plasma frequency,* ω_p^2*, and (b) position,* ω_o*, of the oscillators number 2 and 3 (see Fig. 6.5). Notice also that in sample S18 above 110 K, peak 2 almost merges with peak 3. Therefore, above this temperature, we have kept* $\omega_{p,2}$ *constant.*

in manganites presenting a metallic phase, the intensity of this peak decreases. In some cases it looks like the whole feature shifts to lower frequency increasing its intensity and eventually converting in a Drude peak. [154, 153] In other cases, it seems that it splits in two peaks, one behaving as described before, the other shifting to higher frequencies and loosing its intensity. [150, 165, 151] In the first case, from measurements in thin films, the entire feature was assigned to intersite transitions (*II* and *III* in Fig. 6.6b) where the spin of the final state is parallel to the t_{2g} core. This explains the increasing intensity in the FM state. In the second case, a similar assignment is given to peak 2, namely it is a transition of type *II* in the parallel configuration. [152] When clearly separated from peak 2, oscillator 3 has been given two interpretations. One candidate is a transition type *I* [152, 164] which, though not allowed, can be enhanced by local distortions and strong hybridization. It is argued that depending so strongly on the lattice distortions, its decrease in temperature is related to the fact that lattice distortions also become weaker. [160] The other candidate is an interatomic transition of the type *III* where the final state is antiparallel to the t_{2g} core. [165] This kind of transitions is strongly linked to transitions where the final state is parallel.

Starting at $T = 0$, where the material is FM, only transitions to a parallel final state are possible. Then, as T increases, the t_{2g} spins are not perfectly aligned anymore and the intensity of parallel transitions decrease in favor of antiparallel transitions. [154] Quijada et al. assigned this kind of transitions to a region at around 3 eV that also decreases as T is lowered from room temperature. [154]

It is rather difficult to solve this controversy with optical measurements alone. However, with the detailed temperature dependence obtained in our experiments we can give some hints to what could be a good assignment. Let us start with peak number 2. According to the previous discussion, there are few doubts that this peak correspond to parallel transitions of either type *II* or type *III*. The fact that this peak is favored in the FM state confirms it. If we take into account that the energy U is estimated to be at least larger than 3 eV, [167, 166] a transition of the type *III* has to be located are rather large frequencies. Therefore, as concluded by Jung et al., [152] this peak most probably correspond to parallel transitions of the type *II*. Moreover, it is well established that it has a polaronic origin, probably enhanced in films and polished samples due to strains. There has also been some discussion about whether it corresponds to a change from small to large polaron [150, 154, 163] or remains small [155] in the whole temperature range. A careful fit to the corresponding analytical expressions allowed to recognize, at least in $La_{2/3}Ca_{1/3}MnO_3$ thin films, as always being an small polaron. [155] The temperature dependence of its position was found to be much larger than in the case of $La_{2/3}Sr_{1/3}MnO_3$ where the polaron seems to be large. The temperature dependence of the position of peak 2, in both S16 and S18, is more similar to the one found for the small polaron case.

Regarding peak 3, it is evident from our experiments (see Fig. 6.7) that its temperature dependence closely follows that of peak 2. Its strength, moreover, is rather large for a dipole prohibited transition. Therefore, it is more likely that it corresponds to an antiparallel transition *II* (as discussed above, the large value of U makes it less likely to be a type *III* transition). It has to be mentioned that if the transition is indeed antiparallel, it should disappear completely in the FM state. This is not the case as demonstrated in Fig. 6.7, however, we will argue below that this is a manifestation of phase separation. The other candidate for this kind of transitions is the feature at 3 eV. Following the same procedure that Quijada et al [154] used to recognize the temperature dependence at 3 eV, in Fig. 6.8 we plot the difference between $\sigma_1(\omega)$ at any given temperature and $\sigma_1(\omega)$ at 10 K. As in Ref. [154] we can also see that at around 2.8 eV there is a region where the conductivity is suppressed below T_C. Although this region can also correspond to antiparallel transitions, it is less likely as the temperature dependence seems to be less *linked* to T_C as expected for this kind of transitions (see insets in Fig. 6.8).

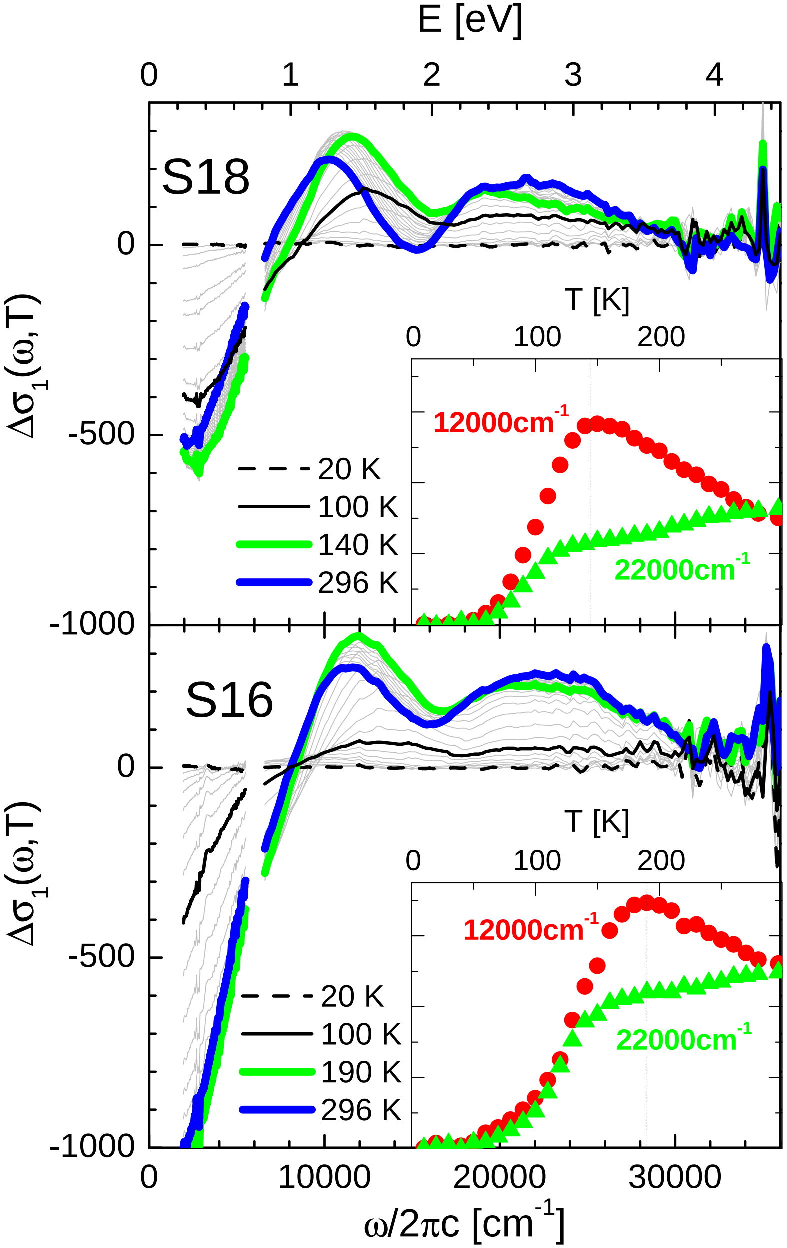

Figure 6.8: *Difference between optical conductivities, $\Delta\sigma_1(\omega, T) \equiv \sigma_1(\omega, T) - \sigma_1(\omega, 10K)$ for the two samples. There are two clear regions where $\sigma_1(\omega)$ decreases below T_C. The insets show the temperature dependencies at 12000 and 22000 cm^{-1}.*

6.3.3 Phase Separation

A scenario that can possibly explain the optical results, at least qualitatively, is phase separation. In the first place it is clear that, whatever the interpretation, peak 2 is favored in the metallic FM phase, while peak 3 is favored in the insulating phase (even in the AF phase as can be seen in $\mathrm{Pr_{0.69}Ca_{0.31}MnO_3}$)[169]. In the phase separation scenario proposed to explain the isotope effect, [26] at high temperatures the insulating phase is dominating. When the temperature is lowered, there is first tendency to charge ordering ($T_{CO} > T_C$) in the insulating phase. Below T_C, FM metallic droplets start to form until the relative volume between them stabilizes. The temperature variation of the spectral weights of both peaks 2 and 3 are consistent with this interpretation. Moreover, their temperature dependence is similar to the one seen in the MIR peak of $\mathrm{La_{7/8}Sr_{1/8}MnO_3}$ where it was also suggested to be caused by phase separation. [147] The large isotope effect seen in this compounds results from the fact that the small change induced by the isotope substitution shifts the relative stability of one phase over the other, especially close to the phase boundary. [170] In the present case, the ^{18}O substitution favors the insulating phase. This is also in agreement with the behavior of peaks 2 and 3 when comparing their strengths between S16 and S18 at the lowest temperature. In S18 (the less metallic of the two), the former oscillator is weaker while the latter is stronger. As discussed in Ref. [170], the isotope substitution changes the effective hopping integral, t_{eff}, which actually determines the relative stability of the different phases. The change produced by the isotope substitution is small but can be enhanced if the charge carriers have polaronic nature. This, as we have seen in the previous section, is the case in the samples studied here, and may help to explain the large isotope effect.

6.3.4 Spectral Weight

Finally, we want to comment about the spectral weight contained in $\sigma_1(\omega)$ and which was defined in Eq. 2.8. Applying this formula to the optical conductivity, we obtain the results presented in Fig. 6.9. The most conspicuous feature in the figure is the difference in spectral weight at low temperatures in the different samples, being lower in the sample with lower T_C. Since they have approximately the same spectral weight at high temperatures, this reduces the range where it is recovered. This is at variance with other experiments, where the recovery happens in roughly the same range, although the amount of spectral weight is different for different samples. [154, 151] In particular, for $\mathrm{(La_{1-y}Pr_y)_{0.7}Ca_{0.3}MnO_3}$ samples with different Pr concentrations, a scaling between N_{eff} at 0.5 eV and T_C was found. In our case no scaling has been found.

It is also interesting to compare different compounds where the distribution of spectral weight has also been studied. In the manganites studied here, the increase of spectral weight at low frequencies due to the formation of the metallic state is recovered in an energy region of approximately 4 eV. This is an indication

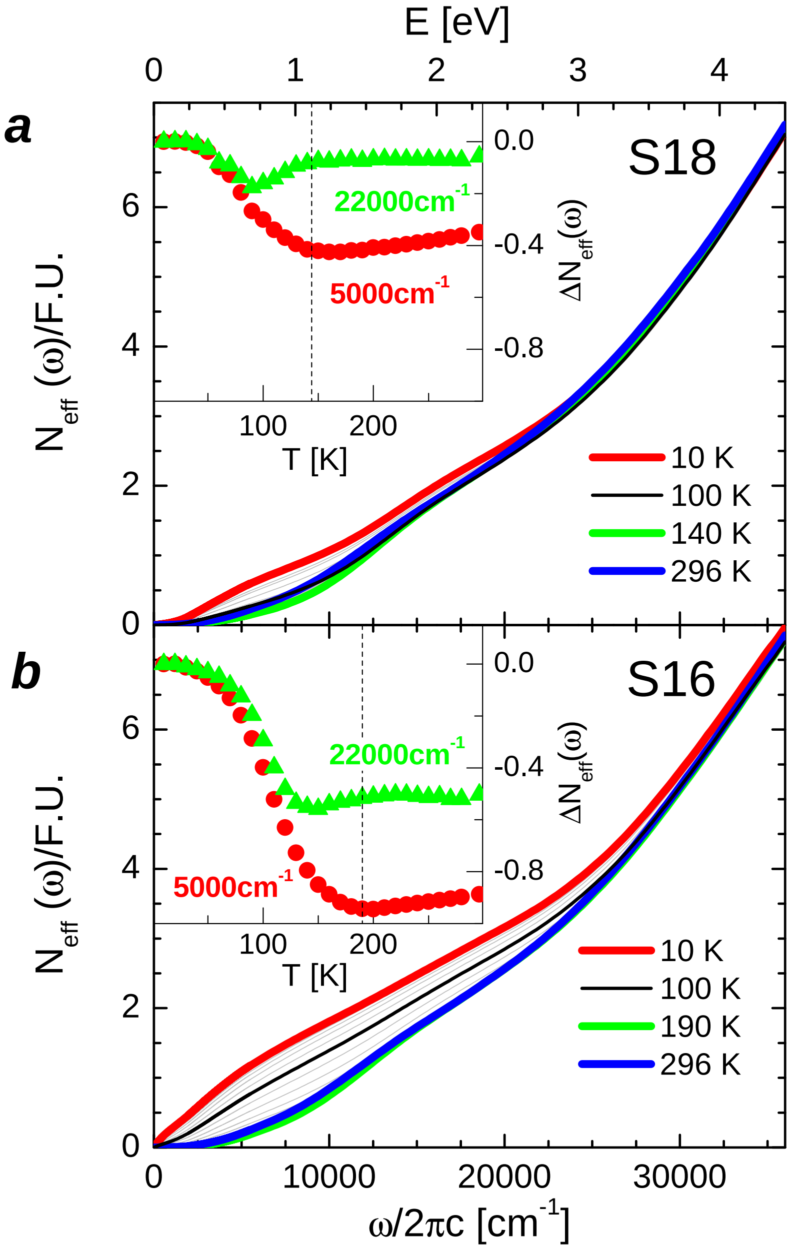

Figure 6.9: *Integrated spectral weight, N_{eff}, in the whole measured range. The insets show the temperature dependence of $\Delta N_{eff} \equiv N_{eff}(T) - N_{eff}(10\ K)$ at two different frequencies.*

of the width of the d bands involved in the physical process. In heavy fermion systems, the spectral weight is recovered in an energy range of 0.2 eV which indicates the narrowness of the f-bands participating in the process of forming the heavy fermion coherent state. [57] On the other hand, in FeSi the spectral weight lost in the formation of the Kondo insulating phase is not recovered below 4 eV. This is also an indication of the width of the d-bands describing its behavior. [88]

6.4 Conclusions

The optical properties of two $(La_{0.5}Pr_{0.5})_{0.7}Ca_{0.3}MnO_3$ films containing different oxygen isotopes were presented here. These films were grown on $SrTiO_3$ substrates. The mismatch between the film and substrate lattice constants makes the films to be under high strains. In turn the strains change the properties of the films and make them more susceptible to phase separate at low temperatures. Evidence of this behaviour was found in the observed optical response at low frequencies. In the paramagnetic insulating phase the optical conductivity of both films is similar and is dominated by a large peak identified as $e_g^1(\mathrm{Mn}^{+3}) \rightarrow e_g(\mathrm{Mn}^{+4})$ where the moved electron ends up being antiparallel to the t_{2g} core. At temperatures below T_C it looses intensity until it saturates at around 100 K. In the less metallic sample (that containing ^{18}O), the intensity of this peak at low temperatures is larger than the more metallic one. On the other hand, the decrease of this transition is accompanied by the increase of another peak located at lower frequencies. This one has been identified as the same kind of transition but with the important difference that the moved electron ends up being parallel to the spin of the t_{2g} electrons. The intensity of this peak is larger in the more metallic sample. These observations taken together suggest that below T_C the samples separate in two phases, one ferromagnetic metallic and one paramagnetic insulating. The relative volume of these phases is different in every sample, the metallic one being larger in the sample containing ^{16}O. Moreover, we have seen that the peak located at lower temperatures has polaronic character and that in the more metallic sample goes in hand with a narrow Drude peak containing only a small fraction of the total spectral weight.

Bibliography

[1] E. F. Nichols, Phys. Rev. (Series I) **1**, 1 (1893).

[2] A. J. Millis, J. El. Spec. and Rel. Ph. **114-116**, 669 (2001).

[3] A. Chattopadhyay, A. J. Millis, and S. Das Sarma, Phys. Rev. B **61**, 10738 (2000).

[4] T. Moriya, *Spin Fluctuations in Itinerant Electron Magnetism*, (Springer, Berlin 1985).

[5] J. E. Hirsch, Phys. Rev. B **59**, 6256 (1999) and references therein.

[6] P. W. Anderson, Phys. Rev. **124**, 41 (1961).

[7] N. Manyala, Y. Sidis, J. F. DiTusa, G. Aeppli, D. P. Young and Z. Fisk, Nature **404**, 581 (2000).

[8] S. Ogawa, Physica B **91**, 82 (1977).

[9] J. E. Hirsch, Phys. Rev. B 59, 436 (1999).

[10] E. J. Singley, R. Kawamani, D. D. Awschalom and D. N. Basov, Phys. Rev. Lett. **89**, 97203 (2002).

[11] L. Degiorgi, E. Felder, H. R. Ott, J. L. Sarrao and Z. Fisk, Phys. Rev. Lett. **79**, 5134 (1997).

[12] S. Kondo, D. C. Johnston, C. A. Swenson, F. Borsa, A. V. Mahajan, L. L. Miller, T. Gu, A. I. Goldman, M. B. Maple, D. A. Gajewski, E. J. Freeman, N. R. Dilley, R. P. Dickey, J. Merrin, K. Kojima, G. M. Luke, Y. J. Uemura, O. Chmaissem, and J. D. Jorgensen, Phys. Rev. Lett. **78**, 3729 (1997).

[13] P. Fulde, *Electron Correlations in Molecules and Solids* (Springer-Verlag, Berlin, 1995).

[14] G. R. Stewart, Rev. Mod. Phys. **56**, 755 (1984).

[15] K. Andres, J. E. Graebner, and H. R. Ott, Phys. Rev. Lett. **35**, 1779 (1975).

[16] C. Kittel, *Introductio to Solid State Physics* (John Wiley & Sons, New York, 1996).

[17] A. J. Millis and P. A. Lee, Phys. Rev. B **35**, 3394 (1987).

[18] H. Shishido, R. Settai, D. Aoki, S. Ikeda, H. Nakawaki, N. Nakamura, T. Iizuka, Y. Inada, K. Sugiyama, T. Takeuchi, K. Kindo, T. C. Kobayashi, Y. Haga, H. Harima, Y. Aoki, T. Namiki, H. Sato, and Y. Nuki, J. Phys. Soc. Jap. **71**, 162 (2002).

[19] A. J. Millis, Nature **392**, 147 (1998).

[20] C. Zener, Phys. Rev. **82**, 403 (1951).

[21] G. H. Jonker and J. H. van Santen, Physica **16**, 337 (1950). J. H. van Santen and G. H. Jonker, Physica **16**, 599 (1950).

[22] N. Furukawa, in *Physics of Manganites*, edited by T. A. Kaplan and S. D. Mahanti (Kluwer Academic, New York, 1999).

[23] A. Moreo, S. Yunoki, and E. Dagotto, Science **283**, 2034 (1999).

[24] H. Y. Hwang, S-W. Cheong, P. G. Radaelli, M. Marezio, and B. Batlogg, Phys. Rev. Lett. **75**, 914 (1995).

[25] P. G. de Gennes, Phys. Rev. **118**, 141 (1960).

[26] D. Khomskii, Physica B **280**, 325 (2000).

[27] S. Yunoki, J. Hu, A. L. Malvezzi, A. Moreo, N. Furukawa, and E. Dagotto, Phys. Rev. Lett. **80**, 845 (1998).

[28] D. P. Arovas and F. Guinea, Phys. Rev. **58**, 9150 (1998).

[29] M. Yu. Kagan, D.I. Khomskii, and M. V. Mostovoy, Eur. Phys. J. B 12, 217 (1999).

[30] P. F. Maldague, Phys. Rev. B **16**, 2437 (1977).

[31] D. Baeriswyl, C. Gros, and T. M. Rice, Phys. Rev. B **35**, 8391 (1987).

[32] M. J. Rozenberg, G. Kotliar and H. Kajueter, Phys. Rev. B **54**, 8452 (1996).

[33] F. Wooten, *Optical Properties of Solids* (Academic Press, New York and London, 1972).

[34] M. Dressel and G. Grüner, *Electrodynamics of Solids* (University Press, Cambridge, England, 2002).

[35] P. W. Anderson, Phys. Rev. B **55**, 11785 (1997).

[36] D. van der Marel, Phys. Rev. B **60**, R765 (1999).

[37] D. van der Marel, H. J. A. Molegraaf, J. Zaanen, Z. Nussinov, F. Carbone, A. Damascelli, H. Eisaki, M. Greven, P. H. Kes, and M. Li, Nature **425**, 271 (2003).

[38] S. V. Shulga, O. V. Dolgov, and E. G. Maksimov , Physica C **178**, 266 (1991).

[39] J. W. Allen and J. C. Mikkelsen, Phys. Rev. B **15**, 2952 (1977).

[40] P. B. Allen, Phys. Rev. B **3**, 305 (1971).

[41] A. V. Puchkov, D. N. Basov, and T. Timusk, J. Phys.: Condens. Matter **8**, 10049 (1996).

[42] R. M. A. Azzam and N. M. Bashara, *Ellipsometry and Polarized Light* (North Holland Publ. Co., Amsterdam, 1997).

[43] C. Presura, Ph. D. Thesis, University of Groningen (2003).

[44] H. Somal. S. Somal, B. J. Feenstra, J. Schützmann, J. H. Kim, Z. H. Barber, V. H. M. Duijn, N. T. Hien, A. A. Menovsky, M. Palumbo, and D. van der Marel, Phys. Rev. Lett. **76**, 1525 (1996).

[45] J. W. van der Eb, A. B. Kuzmenko, and D. van der Marel, Phys. Rev. Lett. **86**, 3407 (2001).

[46] F. P. Mena, D. van der Marel, A. Damascelli, M. Fäth, A. A. Menovsky, and J. A. Mydosh, Phys. Rev. B **67**, 241101 (2003).

[47] H. Somal. PhD thesis, University of Groningen (1998).

[48] F. P. Mena, D. van der Marel, C. Presura, A. Damascelli, G. Aeppli, J. DiTusa, D. P. Young, A. Lichtenstein, A. Poteryaev, B. Gorshunov, M. Dressel, A. A. Menovsky, and J. A. Mydosh, to be published.

[49] O. S. Heavens, *Thin Film Physics* (Methuen, London , England, 1970).

[50] A. Kuzmenko, *Guide to Reffit: Software to fit optical spectra* (2004). Available online at *http://optics.unige.ch/alexey/reffit.html.*

[51] C. Pfleiderer, S.R. Julian and G.G. Lonzarich, Nature **414**, 427 (2001).

[52] A. Damascelli, Ph.D. Thesis, University of Groningen, The Netherlands, 1999.

[53] N. Doiron-Leyraud, I. R. Walker, L. Taillefer, M. J. Steiner, S. R. Julian, and G. G. Lonzarich, Nature **425**, 595 (2003).

[54] M. Fäth, Ph.D. Thesis, University of Leiden, The Netherlands, 1999.

[55] H. Wiesmann, M. Gurvitch, H. Lutz, A. Ghosh, B. Schwarz, M. Strongin, P. B. Allen, and J. W. Halley, Phys. Rev. Lett. **38**, 782 (1977).

[56] M. Calandra and O. Gunnarsson, Phys. Rev. B **66**, 205105 (2002).

[57] L. Degiorgi, Rev. Mod. Phys. **71**, 687 (1999).

[58] L. Taillefer, G. G. Lonzarich, and P. Strange, J. Magn. Magn. Mater. **54-57**, 957 (1986).

[59] E. Fawcett, J. P. Maita, and J. H. Wernick, Intern. J. Magn. **1**, 29 (1970).

[60] T. Katsufuji and Y. Tokura, Phys. Rev. B **60**, 7673 (1999).

[61] D. Pines and P. Noziers, *The Quantum Theory of Solids* (Benjamin, New York, 1966).

[62] P. S. Riseborough, Phys. Rev. B **27**, 5775 (1983).

[63] J. S. Dodge, C. P. Weber, J. Corson, J. Orenstein, Z. Schlesinger, J. W. Reiner, and M. R. Beasley, Phys. Rev. Lett. **85**, 4932 (2000).

[64] M. S. Laad and E. Müller-Hartmann, Phys. Rev. Lett. 87, 246402 (2001).

[65] J. C. Phillips, Phil. Mag. B **81**, 757 (2001).

[66] L. Capogna, A. P. Mackenzie, R. S. Perry, S. A. Grigera, L. M. Galvin, P. Raychaudhuri, and A. J. Schofield, C. S. Alexander, G. Cao, S. R. Julian, and Y. Maeno , Phys. Rev. Lett. **88**, 76602 (2002).

[67] Z. Schlesinger, R. T. Collins, F. Holtzberg, C. Feild, S. H. Blanton, U. Welp, G. W. Crabtree, Y. Fang, and J. Z. Liu, Phys. Rev. Lett. **65**, 801 (1990).

[68] Y. S. Lee, Jaejun Yu, J. S. Lee, T. W. Noh, T. H. Gimm, Han-Yong Choi, and C. B. Eom , Phys. Rev. B **66**, 041104(R) (2002).

[69] C. Pfleiderer, D. Reznik, L. Pintschovius, H. v. Löhneysen, M. Garst, and A. Rosch, Nature **427**, 227 (2003).

[70] H. Yasuoka, V. Jaccarino, R. C. Sherwood, and J. H. Wernick, J. Jpn. Phys. Soc. **44**, 842 (1978)

[71] S. G. Mishra, Mod. Phys. Lett **4**, 83 (1990).

[72] M. B. Hunt, M. A. Cherikov, E. Felder, H. R. Ott, Z. Fisk and P. Canfield, Phys. Rev. B **50**, 14933 (1994).

[73] J. H. Wernick, G. K. Wertheim and R. C. Sherwood, Mat. Res. Bull. **7**, 476 (1972).

[74] J. Beille, J. Voiron, F. Towfiq, M Roth and Z. Y. Zhang, J. Phys. F: Metal Phys. **11**, 2153 (1981).

[75] K. Ishimoto, M. Ohashi, H. Yamauchi and Y. Yamaguchi, J. Phys. Soc. Jap. **61**, 2503 (1992).

[76] C. Pfleiderer , M. Uhlarz, S. M. Hayden, R. Vollmer, H. v. Löhneysen, N. R. Bernhoeft, and G. G. Lonzarich, Nature **412**, 58 (2001).

[77] Y. Takahashi, J. Phys.: Condens. Matter **11**, 6439 (1999);

[78] J. E. Hirsch, Phys. Rev. B **44**, 675 (1991).

[79] F. J. Ohkawa, Phys. Rev. B **65**, 174424 (2003).

[80] A. Aguayo and D. J. Singh, Phys. Rev. B **66**, 020401 (2002).

[81] M. Huang, H. J. F. Jansen and A. J. Freeman, Phys. Rev. B **37**, 3489 (1988).

[82] O. Nakanishi, A. Yanase and A. Hasegawa, J. Mag. Mag. Mat. **15-18**, 879 (1980).

[83] S. N. Evangelou and D. M.Edwards, J. Phys. C.: Solid State Phys. **16**, 2121 (1982).

[84] Y. Takahashi, J. Phys.: Condens. Matter **9**, 2593 (1997).

[85] T. Jarlborg, Phys. Lett. A **236**, 143 (1997); Phys. Rev. B , 15002 (1999).

[86] L. Vočadlo, K. S. Knight, G. D. Price and I. G. Wood, Phys. Chem. Minerals **29**, 132 (2002).

[87] G. Aeppli and Z. Fisk, Comm. Cond. Mat. Phys. **16**, 155 (1992).

[88] Z. Schlesinger, Z. Fisk, H. T. Zhang, M. B. Maple, J. F. DiTusa and G. Aeppli, Phys. Rev. Lett. **71**, 1748 (1993).

[89] C. Fu and S. Doniach, Phys. Rev. B **51**, 17439 (1995). cond-mat/0002160.

[90] L. Degiorgi, Rev. Mod. Phys. **71**, 687 (1999).

[91] L. Degiorgi, M. B. Hunt, H. R. Ott, M. Dressel, B. J. Feenstra, G, Grüner, Z. Fisk, and P. Canfield, Europhys. Lett. **28**, 341 (1994).

[92] A.A. Menovsky, and J.J.M. Franse, J. Cryst. Growth 65, 286 (1983).

[93] A. Damascelli, K. Schulte, D. van der Marel, and A. A. Menovsky, Physical Review B **55**, R4863 (1997).

[94] G. Kozlov and A. Volkov, in *Millimeter and submillimeter wave spectroscopy of solids*, edited by G. Grüner (Springer, Berlin, 1998), p. 51.

[95] W. Kohn and L.J. Sham, Phys. Rev. **140**, A1133 (1965).

[96] O. Gunnarsson and B. Lundqvist, Phys. Rev. B **13**, 4274 (1976).

[97] S. Savrasov and D. Savrasov, Phys. Rev. B **46**, 12181 (1992).

[98] B. Borèn, Ark. Kemi Min. Geol. **11A**, 1 (1933).

[99] Yu. A. Uspenski, E. G. Maksimov, S. N. Rashkeev and I. I. Mazin, Z. Phys. B **53**, 263 (1983); I. I. Mazin, E.G. Maksimov, S. N. Rashkeev, S. Yu. Savrasov and Yu. A. Uspenskii, JETP Letters **47**, 113 (1988).

[100] K. Shimizu, H. Maruyama, H. Yamazaki and H. Watanabe, J. Phys. Soc. Jap. **59**, 305 (1990).

[101] M. A. Chernikov, L. Degiorgi, E. Felder, S. Paschen, A. D. Bianchi and H. R. Ott, Phys. Rev. B **56**, 1366 (1997).

[102] H. Otha, S. Kimura, E. Kulatov, S. V. Halilov, T. Nanba, M. Motokawa, M. Sato and K. Nagasaka , J. Phys. Soc. Jap. **63**, 4206 (1994); E. Kulatov, H. Otha, T. Arioka, S. V. Halilov and L. Vinokurova, J. Phys.: Condens. Matter **9**, 9043 (1997);

[103] M. Fäth, J. Aarts, A. A. Menovsky, G. J. Nieuwenhuys, and J. A. Mydosh, Phys. Rev. B **58**, 15483 (1998).

[104] C. Fu, M. C. P. M. Krijn and S. Doniach, Phys. Rev. B **49**, 2219 (1994).

[105] L. F. Mattheiss and D. R. Hamann, Phys. Rev. B **47**, 13114 (1993).

[106] T. Jarlborg, Physica B **293**, 224 (2001).

[107] P. Lerch and T. Jarlborg, J. Mag. Mag. Mat. **131**, 321 (1994).

[108] J. Guevara, J. L. Vildosola, J. Milano, and A. M. Llois, Physica B **320**, 388 (2002).

[109] K. Urasaki and T. Saso, Physica B **281-282**, 313 (2000).

[110] M. Dressel and G. Grüner, *Electrodynamics of solids: optical properties of electrons in matter*, (Cambridge University Press, Cambridge, UK, 2002).

[111] C. M. Varma, Phys. Rev. B **50**, 9952 (1994).

[112] K. Urasaki and T. Saso, Phys. Rev. B **58**, 15528 (1998)..

[113] Y. Okimo, T. Katsufuji, T. Ishikawa, T. Arima, and Y. Tokura, Phys. Rev. B **55**, 4206 (1997).

[114] D. van der Marel, A. Damascelli, K. Schulte, and A.A. Menovsky, Physica B **244**, 138 (1998).

[115] Molegraaf, H. J. A., Presura, C., van der Marel, D., Kes, P. H., and Li, M, Science **295**, 2239 (2002).

[116] C. Petrovic, R. Movshovich, M. Jaime, P. G. Pagliuso, M. F. Hundley, J. L. Sarrao, Z. Fisk, and J. D. Thomson, Europhys. Lett. **53**, 354 (2001).

[117] C. Petrovic, P. G. Pagliuso, M. F. Hundley, R. Movshovich, J. L. Sarrao, J. D. Thompson, Z Fisk and P. Monthoux, J. Phys.: Condens. Matter **13**, 337 (2001).

[118] H. Hegger, C. Petrovic, E. G. Moshopoulou, M. F. Hundley, J. L. Sarrao, Z. Fisk, and J. D. Thomson, Phys. Rev. Lett. **84**, 4986 (2000).

[119] A. Bianchi, R. Movshovich, I. Vekhter, P. G. Pagliuso, and J. L. Sarrao, Phys. Rev. Lett. **91**, 257001 (2003); J. Paglione, M. A. Tanatar, D. G. Hawthorn, E. Boaknin, R. W. Hill, F. Ronning, M. Sutherland, and L. Taillefer, *ib.* **91**, 246405 (2003).

[120] V. A. Sidorov, M. Nicklas, P. G. Pagliuso, J. L. Sarrao, Y. Bang, A. V. Balatsky, and J. D. Thompson, Phys. Rev. Lett. **89**, 157004 (2002).

[121] T. Mito, S. Kawasaki, Y. Kawasaki, G. Zheng, Y. Kitaoka, D. Aoki, Y . Haga, and Y. Onuki, Phys. Rev. Lett. **90**, 77004 (2003).

[122] P. G. Pagliuso, R. Movshovich, A. D. Bianchi, M. Nicklas, N. O. Moreno, J. D. Thompson, M. F. Hundley, J. L. Sarrao and Z. Fisk, Physica B **312-313**, 274 (2002).

[123] S. Burdin, A. Georges, and D. R. Grempel, Phys. Rev. Lett. **85**, 1048 (2000) and references therein.

[124] A. N. Tahvildar-Zadeh, M. Jarrell, and J. Freericks, Phys. Rev. B **55**, 3332 (1997).

[125] J. R. Iglesias, C. Lacroix, and B. Coqblin, Phys. Rev. B **56**, 11820 (1997).

[126] B. Coqblin, C. Lacroix, M. A. Gusmao, and J. R. Iglesias, Phys. Rev. B **67**, 64417 (2003).

[127] S. Nakatsuji, S. Yeo, L. Balicas, Z. Fisk, P. Schlottmann, P. G. Pagliuso, N. O. Moreno, J. L. Sarrao, and J. D. Thompson, Phys. Rev. Lett. **89**, 106402 (2002).

[128] S. Nakatsuji, D. Pines, and Z. Fisk, cond-mat/0304587.

[129] E. J. Singley, D. N. Basov, E. D. Bauer, and M. B. Maple, Phys. Rev. B **65**, 161101R (2002).

[130] S. V. Dordevic, D. N. Basov, N. R. Dilley, E. D. Bauer, and M. B. Maple, Phys. Rev. Lett. **86**, 684 (2001).

[131] A. J. Millis, M. Lavagna, and P. Lee, *ib.* **36**, 864R (1987).

[132] P. Coleman, Phys. Rev. Lett. **59**, 1026 (1987); M. Jarrel, Phys. Rev. B **51**, 7429 (1995).

[133] A. L. Cornelius, P. G. Pagliuso, M. F. Hundley, and J. L. Sarrao, Phys. Rev. B **64**, 144411 (2001).

[134] J. S. Kim, J. Alwood, D. Mixson, P. Watts, and G. R. Stewart Phys. Rev. B **66**, 134418 (2002).

[135] See for example: S. Fujimori, T. Okane, J. Okamoto, K. Mamiya, Yasuji Muramatsu, D. Aoki, S. Ikeda, H. Shishido, Y. Tokiwa, and Y. Ōnuki, Phys. Rev. B **67**, 144507 (2003) and references therin.

[136] A. M. Awasthi, L. Degiorgi, G. Grüner, Y. Dalichaouch and M. B. Maple, Phys. Rev. B **48**, 10692 (1993).

[137] A. D. Christianson, A. H. Lacerda, M. F. Hundley, P. G. Pagliuso, and J. L. Sarrao, Phys. Rev. B **66**, 54410 (2002).

[138] R. T. Macaluso, J. L. Sarrao, P. G. Pagliuso, N. O. Moreno, R. G. Goodrich, D. A. Browne, F. R. Fronczek, and J. Y. Chan, J. Sol. St. Chem. **166**, 245 (2002).

[139] U. Alver et al., Phys. Rev. B **64**, 180402R (2001).

[140] L. M. Rodriguez-Martinez and J. P. Attfield, Phys. Rev. B **54**, R15622 (1996).

[141] A. M. Balagurov, V. Yu. Pomjakushin, D. V. Sheptyakov, V. L. Aksenov, P. Fischer, L. Keller, O. Yu. Gorbenko, A. R. Kaul, and N. A. Babushkina, Phys. Rev. B **64**, 24420 (2001).

[142] N. A. Babushkina, L. M. Belova, A. N. Taldenkov, E. A. Chistotina, D. I. Khomskii, K. I. Kugelk, O. Yu. Gorbenko, and A. R. Kaul, J. Phys.: Condens. Matter **11**, 5865 (1999).

[143] N. A. Babushkina, L. M. Belova, O. Yu. Gorbenko, A. R. Kaul, A. A. Bosak, V. I. Ozhogin, and K. I. Kugel, Nature **391**, 159 (1998).

[144] A. M. Balagurov, V. Yu. Pomjakushin, D. V. Sheptyakov, V. L. Aksenov, N. A. Babushkina, L. M. Belova, A. N. Taldenkov, P. Fischer, M. Gutmann, L. Keller, O. Yu. Gorbenko and A. R. Kaul, Babushkina, Phys. Rev. B **60**, 383 (1999).

[145] N. A. Babushkina, L. M. Belova, E. A. Chistotina, O. Yu. Gorbenko, A. R. Kaul, B. Güttler, and K. I. Kugel, Eur. Phys. J. B **19**, 409 (2001).

[146] N. A. Babushkina, L. M. Belova, D. I. Khomskii, I. Kugel, O. Yu. Gorbenko, and A. R. Kaul, Phys. Rev. B **59**, 6994 (1999).

[147] J. H. Jung, K. H. Kim, H. J. Lee, J. S. Ahn, N. J. Hur, T. W. Noh, M. S. Kim, and J.-G. Park, Phys. Rev. B **59**, 3793 (1999).

[148] D. Emin, Phys. Rev. B **59**, 13691 (1993).

[149] A. S. Moskvin, E. V. Zenkov, Yu. D. Panov, N. N. Loshkareva, Yu. P. Sukhorukov, and E. V. Mostovshchikova, Phys. Sol. St. **44**, 1519 (2002).

[150] K. H. Kim, J. H. Jung, and T. W. Noh, Phys. Rev. Lett. **81**, 1517 (1998).

[151] K. H. Kim, J. H. Jung, D. J. Eom, T. W. Noh, J. Yu, and E. J. Choi, Phys. Rev. Lett. **81**, 4983 (1998).

[152] J. H. Jung, K. H. Kim, T. W. Noh, E. J. Choi, and Jaejun Yu, Phys. Rev. B **57**, 11043 (1998).

[153] K. Takenaka, K. Iida, Y. Sawaki, S. Sugai, Y. Moritomo, and A. Nakamura, J. Phys. Soc. Jpn **68**, 1828 (1999).

[154] M. Quijada, J. Černe, K. H. Ahn, A. J. Millis, R. Shreekala, R. Ramesh, M. Rajeswari, and T. Venkatesan, Phys. Rev. B **58**, 16093 (1998).

[155] Ch. Hartinger, F. Mayr, J. Deisenhofer, A. Loidl, and T. Kopp, Phys. Rev. B **69**, 100403 (2004).

[156] A. S. Moskvin, Physica B **252**, 186 (1998).

[157] A. S. Moskvin, E. V. Zenkov, Yu. P. Sukhorukov, E. V. Mostovshchikova, N. N. Loshkareva, A. R. Kaul, and O. Yu. Gorbenko, J. Phys.: Condens. Matter **15**, 2635 (2003).

[158] N. N. Loshkareva, Yu. P. Sukhorukov, E. A. Ganshina, E. V. Mostovshchikova, R. Yu. Kumaritova, A. S. Moskvin, Yu. D. Panov, O. Yu. Gorbenko, and A. R. Kaul, J. Exp. Th. Phys. **92**, 462 (2001).

[159] E. Palik, *Handbook of Optical Constants of Solids* Volume II, (Academic Press, Inc., New York, 1991).

[160] T. W. Noh, J. H. Jung, and K. H. Kim, in *Physics of Manganites*, edited by T. A. Kaplan and S. D. Mahanti (Kluwer Academic, New York, 1999).

[161] K. Takenaka, Y. Sawaki, R. Shiozaki, and S. Sugai, Phys. Rev. B **62**, 13864 (2000).

[162] K. Takenaka, R. Shiozaki, and S. Sugai, Phys. Rev. B **65**, 184436 (2002).

[163] A. J. Millis, R. Mueller, and Boris I. Shraiman, Phys. Rev. B **54**, 5405 (1996).

[164] Y. Chen, V. Perebeinos, and P. B. Allen, Phys. Rev. B **65**, 205207 (2002).

[165] Y. Okimoto, T. Katsufuji, T. Ishikawa, T. Arima, and Y. Tokura, Phys. Rev. B **55**, 4206 (1997).

[166] T. Saitoh, A. E. Bocquet, T. Mizokawa, H. Namatame, A. Fujimori, M. Abbate, Y. Takeda, M. Takano, Phys. Rev. B **51**, 13942 (1995).

[167] J.-H. Park, C. T. Chen, S-W. Cheong, W. Bao, G. Meigs, V. Chakarian, and Y. U. Idzerda, Phys. Rev. Lett. **76**, 4215 (1996).

[168] Y. Okimoto and Y. Tokura, J. of Supercond., **13**, 271 (2000).

[169] H. J. Lee, J. H. Jung, K. H. Kim, M. W. Kim, T. W. Noh, Y. Moritomo, Y. J. Wang, and X. Wei, Physica C **364-365**, 614 (2001).

[170] N. A. Babushkina, L. M. Belova, V. I. Ozhogin, O. Yu. Gorbenko, A. R. Kaul, A. A. Bosak, D. I. Khomskii, and K. I. Kugel, J. App. Phys. **83**, 7369 (1998).

Samenvatting

Dit proefschrift behandelt optische spectroscopie als hulpmiddel om inzicht te krijgen in de fysische eigenschappen van een aantal sterk gecorreleerde systemen. In het algemeen is optische spectroscopie een uitstekend hulpmiddel voor de studie van de elektronische structuur van een gegeven materiaal omdat de zo bepaalde complexe optische conductiviteit informatie geeft over hoe de elektronen zich door het materiaal bewegen in respons op een extern veld. Een van de processen die beschreven wordt door de optische conductiviteit is de beweging van de elektronen van een roosterpunt naar een ander roosterpunt. De invloed van dit proces wordt bepaald door de competitie tussen elektron-elektron correlaties (die de elektronen localiseren) en golffunctie hybridisatie (wat de elektronen delocaliseerd). Het is precies deze competitie die de essentie vormt van de fysica van sterke correlaties.

Itinerant magnetisme: Siliciden

Het eerste systeem dat in dit proefschrift beschreven wordt is opgebouwd uit een overgangs metaal en Silicium, de zogenaamde silliciden. Met name de silliciden die Mangaan, IJzer en Cobalt bevatten zijn bestudeerd. Alhoewel in deze overgangs metalen magnetisme zich in zijn meest elementaire vorm manifesteert, zijn de corresponderende silliciden verbazingwekkend genoeg niet magnetisch bij kamertemperatuur. Sterker nog, alleen MnSi ($T_C = 30$ K) vertoont magnetisme. Boven T_C volgt MnSi de Curie-Weiss wet met een magnetisatie die veel groter is dan de saturatie magnetisatie in de magnetische fase. Dit definieert MnSi als een zwakke ferromagneet. Zwak ferromagnetisch gedrag duikt ook op in een groot gebied van verhoudingen van mengsels tussen FeSi en CoSi, ondanks het feit dat elk op zich niet magnetisch is. Daarintegen blijkt ferromagnetisme al snel te verdwijnen in MnSi als men Mn gedeeltelijk vervangt door Fe. Een aantal magnetische oplossingen van $\mathrm{Fe}_{1-x}\mathrm{Co}_x\mathrm{Si}$ worden ook bestudeerd in dit proefschrift.

In deze silliciden zijn alle stochiometrische samenstellingen en mengels daarvan slechte metalen bij kamertemperatuur. Echter, het gedrag van verschillende mengels bij verlaging van de temperatuur is zeer divers. De weerstand van MnSi neemt sterk af en blijft metallisch tot de laagste temperaturen zonder supergeleiding te vertonen. Substitutie van Mn door Fe verlaagt alleen de snelheid waarmee de weerstand afneemt als functie van temperatuur en verlaagt T_C. Een verrassende observatie is dat in een dunne strook tussen FeSi en zowel CoSi als MnSi het systeem een insulerende grondtoestand heeft waarvan de oorsprong nog steeds onderwerp van discussie is. Als men meer naar CoSi toegaat voorbij deze dunne strook dan blijft het systeem metallisch met een kleine verlaging van de weerstand. Het gedrag van de weerstand in magnetische velden is ook verschillend voor de magnetische samenstellingen rondom MnSi en die in $\mathrm{Fe}_{1-x}\mathrm{Co}_x\mathrm{Si}$. Rondom MnSi laat het systeem een een negatieve magnetoweerstand zien zoals verwacht voor metalen bij niet te lage temperaturen. In de $\mathrm{Fe}_{1-x}\mathrm{Co}_x\mathrm{Si}$ samples vindt men het tegenovergestelde en het gedrag is zelfs analoog aan de quantum effecten zoals geïnduceerd door wanorde bij extreem lage temperaturen.

Zwak ferromagnetisme wordt normaal gesproken verklaard vanuit een itinerant elektron beeld, zoals kort beschreven in Hoofdstuk 1. Alhoewel het verschillende eigenschappen van zwakke ferromagneten verklaard, faalt deze beschrijving voor sommige andere eigenschappen. Ook verklaart dit beeld niet het verschil in eigenschappen van de groep zwakke ferromagneten rond MnSi en de $\mathrm{Fe}_{1-x}\mathrm{Co}_x\mathrm{Si}$. In dit proefschrift (Hoofdstuk 3) worden de afwijkingen van dit beeld besproken die betrekking hebben op de transport en optische eigenschappen van MnSi. We hebben laten zien dat de optische eigenschappen beschreven kunnen worden met een fenomenologische vergelijking die onder specifieke voorwaarden tot de Drude beschrijving leidt. De implicatie hiervan is dat de temperatuur en frequentie afhankelijkheid (verkregen uit, respectievelijk, de DC weerstand en de optische geleiding) van de botsingstijd verschillend zijn. Dit heeft grote implicaties omdat temperatuur en frequentie slechts verschillende manifestaties van energie zijn.

In Hoofdstuk 4 van dit proefschrift worden FeSi, CoSi en een aantal vaste oplossingen van deze twee bestudeerd. In dit hoofdstuk wordt ook beschreven dat de formatie van de isolerende toestand in FeSi niet conventioneel is in de zin dat deze niet volledig verklaard wordt door banden theorie. Twee observaties waren bepalend voor deze conclusie. Ten eerste, de bandgap van de isolerende toestand is gevuld bij veel lagere temperaturen dan toegestaan voor alleen thermische excitaties. Ten tweede is gedemonstreerd dat het optische spectrale gewicht bevat in de optische geleiding (i.e. de geintegreerde oppervlakte eronder) niet teruggevonden wordt in een energie gebied veel groter dan de bandgap. Dit gebrek duidt op de noodzaak om sterke correlaties te incorporeren in de beschrijving van de isolerende fase van FeSi. Een tweede voordeel is dat deze aanvulling ook de magnetotransport eigenschappen van $\mathrm{Fe}_{1-x}\mathrm{Co}_x\mathrm{Si}$ kan verklaren. Bij relatief hoge temperaturen is de beschrijving van deze eigenschappen dan gelijk aan de beschrijving van sterk wanordelijke metalen bij sub-kelvin temperaturen.

Lokale momenten en itinerante elektronen: Heavy Fermion Systemen

Een aantal systemen laten tekenen zien van meerdere *soorten* elektronen. Aan een kant zijn er itinerante elektronen, verantwoordelijk voor de transport eigenschappen. Aan de andere kant zijn er gelokaliseerde elektronen die bijdragen aan de magnetische eigenschappen. Interacties tussen deze twee soorten elektronen kan leiden tot zeer divers gedrag van dit soort systemen. Een bepaalde klasse van dit soort systemen worden de heavy fermion systemen genoemd. Deze naam vindt zijn oorsprong in het feit dat de eigenschappen van deze systemen gelijk zijn aan die van normale metalen maar met veel grotere proportionaliteits constanten. Aangezien in de standaard theorie van metalen deze constanten proportioneel zijn met de elektron massa, kunnen de versterkte eigenschappen van heavy fermion systemen geinterpreteerd worden als een gerenormaliseerde massa van de elektronen als gevolg van sterke interacties.

In Hoofdstuk 5 van dit proefschrift wordt een bepaalde familie van heavy fermion systemen bestudeerd: $\mathrm{CeMIn_5}$ (M = Co, Rh, Ir). Dit systeem heeft de laatste tijd veel aandacht getrokken vanwege de grote variëteit aanwezig in het fase diagram. Bij verlaging van temperatuur vindt men eerst de opkomst van heavy fermion gedrag gevolgd door antiferromagnetisme in $\mathrm{CeRhIn_5}$ (T_N =3.8 K) en onconventionele supergeleiding in $\mathrm{CeCoIn_5}$ (T_c = 2.4 K) en $\mathrm{CeIrIn_5}$ (T_c = 0.8 K). Het is gesuggereerd dat de supergeleiding in deze materialen overeenkomsten vertoont met die in de hoge T_c supergeleiders. Deze analogie begint al met de rooster structuur die voorgesteld kan worden als lagen van $\mathrm{CeIn_3}$ (een bekend heavy fermion systeem) gescheiden door lagen $\mathrm{MIn_2}$.

Het werk gepresenteerd in dit proefschrift heeft zich geconcentreerd op de optische eigenschappen van de heavy fermion toestand. Er is aangetond dat voor lage temperaturen de optische respons van $\mathrm{CeCoIn_5}$ en $\mathrm{CeIrIn_5}$ gekarakteriseerd kan worden door een smalle Drude piek die de oscillaties van coherente elektronen voorstelt. Deze piek wordt gevormd beneden een bepaalde karakteristieke energie die bekend staat als de hybridisatie gap. Aan de andere kant bestaat er een competitie tussen antiferromagnetisme en de formatie van deze coherente toestand. Dit is gedemostreerd in $\mathrm{CeRhIn_5}$ waar de smalle Drude piek niet volledig opkomt. Verder is aangetond dat uit de studie van de dielektrische functie blijkt dat de hybridisatie gap kleiner is dan in de twee andere materialen.

Lokale Momenten and Itinerante Elektronen: Manganides

Ten slotte zijn materialen uit de perovskide manganide familie bestudeerd. Deze staan bekend om hun fase diagram met diverse fasen. Een voorbeeld hiervan is het $\mathrm{La_{1-x}Ca_xMnO_3}$ systeem. Bij lage temperaturen is de fase gekanteld antiferromagnetisch voor $LaMnO_3$ en $CaMnO_3$ maar daar tussen in worden verschillende fasen gevonden: ferromagnetisch isolerend en metallisch, ladings geordend en antiferromagnetisch. In algemene termen is dit rijke gedrag een gevolg van de interactie tussen lokale momenten en itinerante elektronen op de Mangaan posities. In de ferromagnetisch metallische fase wordt dit goed beschreven door de dubbele exchange Hamiltoniaan. Desalniettemin zijn er andere ideeën en mechanismen nodig voor een complete beschrijving van de Manganiden. Een voorbeeld is de elektronfonon interactie die zich in verschillende vormen manifesteert zoals bijvoorbeeld in een groot isotoop effect. Een ander mechanisme dat in beschouwing moet worden genomen is de natuurlijke tendens van de dubbele exchange Hamiltoniaan naar de produktie van fase scheiding.

Het laatste Hoofdstuk van dit proefschrift beschrijft de optische respons van dunne films van $(La_{0.5}Pr_{0.5})_{0.7}Ca_{0.3}MnO_3$ gegroeid op $SrTiO_3$ substraten. Er zijn samples met verschillende zuurstof isotopen (^{16}O en ^{18}O) bestudeerd. Bij kamertemperatuur laten beide soorten films een identieke DC weerstand zien met geen lange drachts magnetische orde. Wanneer de temperatuur wordt verlaagd neemt de weerstand toe totdat een kritieke temperatuur (T_C) wordt bereikt waaronder de weerstand weer afneemt. Bij deze kritieke temperatuur vindt ook magnetische ordening plaats. Samples met verschillende zuurstof isotopen laten hetzelfde, hierboven beschreven, kwalitatieve gedrag zien. Echter, de samples die de ^{18}O isotoop bevatten hebben een lagere T_C en de weerstand ver beneden T_C is een orde van grootte groter dan zijn tegenhanger met ^{16}O. Een ander verschil wordt duidelijk als de temperatuur verhoogd wordt tot boven T_C. Samples met ^{18}O laten een grote hysterese zien terwijl in de ^{16}O deze hysterese klein is. Er wordt gezegd dat dit een teken van ladings separatie is.

Net als de DC weerstand is de optische respons van beide films identiek bij kamertemperatuur maar zeer verschillend bij lagere temperaturen, met name voor lage frequenties. Voor hogere frequenties (boven 2.5 eV) wordt de optische conductiviteit van beide films gedomineerd door overgangen die corresponderen met ladings overdracht excitaties die zwak temperatuur afhankelijk zijn. Voor lage frequenties, boven de corresponderende T_C's, wordt de optische conductiviteit gedomineerd door een sterke mid-infrarood piek rond 1.5 eV (piek 3). Deze piek wordt versterkt in de paramagnetische toestand omdat hij overeenkomt met de intersite overgang $e_g^1(\mathrm{Mn}^{+3}) \rightarrow e_g(\mathrm{Mn}^{+4})$ waarbij de verplaatste elektronen antiparallel uitkomen ten opzichte van de gelokaliseerde elektronen in het t_{2g} niveau. De intensiteit van piek 3 blijft min of meer constant boven T_C maar neemt daaronder snel af in sterkte. Toch verdwijnt hij niet volledig bij lage temperaturen, met name voor de films met de ^{18}O isotoop waar de piek vrij groot blijft. Een andere piek, aangeduid met nummer 2, kan geïdentificeerd worden voor nog lagere frequenties (0.75 eV). Deze piek is ook als een intersite overgang geïdentificeerd van dezelfde soort als piek 3 met het verschil dat de elektronen nu parallel eindigen ten opzichte van de t_{2g} kern. Om deze reden wordt hij versterkt in de ferromagnetische toestand. Piek 2 is nauwelijks zichtbaar bij hogere temperaturen maar neemt toe in intensiteit onder T_C en verzadigd voordat de laagste temperaturen zijn bereikt. Het is zelfs zo dat de temperatuur afhankelijkheid van piek 2 en 3 volledig symmetrisch is. Een ander punt dat opvalt is dat in het meer metallische sample (^{16}O), piek 2 samengaat met een smalle Drude piek die weinig spectraal gewicht heeft.

In Hoofdstuk 6 is beargumenteerd dat de temperatuur afhankelijkheid zoals hierboven beschreven, begrepen kan worden met een fase scheidings beeld. Onder T_C zijn zowel de ferromagnetische en antiferromagnetische fase aanwezig. Dit is de reden dat piek 3 niet volledig verdwijnt in de ferromagnetische toestand. Sterker nog, isotoop substitutie verandert het relatieve volume van de ene toestand ten opzichte van de andere. Dit verklaart ook het feit dat in de minder metallische toestand piek 3 intenser is bij lage temperaturen.

Spectraal Gewicht

Een centraal probleem in dit proefschrift is de bepaling van het gebied waarover het spectraal gewicht bevat in de optische conductiviteit wordt terug gewonnen. Het is gebleken dat het gebied waarover dit gebeurt afhangt van het karakter van de elektronen die betrokken zijn in laag frequente processen. In de siliciden en manganiden is dit gebied vrij groot omdat de betrokken elektronen een d karakter hebben. In de heavy fermion systemen die bestudeerd zijn, blijkt het gevonden gebied veel kleiner te zijn omdat de elektronen die de coherente toestand vormen een f karakter hebben.

Summary

In this thesis, optical spectroscopy has been used to get an insight in the physical properties of various strongly correlated systems. In general, optical spectroscopy is an excellent tool to study the electronic structure of a given material because its complex optical conductivity gives information about how the electrons move inside the material in response to an external field. A particular process described by the optical conductivity is the motion of the electrons from one site to the other. This process is determined by the competition between electron-electron correlations (which tends to localize the electrons) and wave function hybridization (which tends to delocalize them). It is precisely this competition which is the essence of strong correlations.

Itinerant magnetism: Silicides

The first system described in this thesis contains a transition metal and silicon. In particular the silicides containing manganese, iron and cobalt were studied. Although these transition metals present magnetism in its elemental form, the corresponding silicides, surprisingly, are not magnetic at room temperature. In fact, at low temperatures, the only one that is magnetic is MnSi (T_C = 30 K). Above T_C it follows a Curie-Weiss law with a magnetization much larger than the saturation magnetization in the magnetic phase. This define MnSi as a weak ferromagnet. Weak ferromagnetism also appears in a large region of the solid solutions between FeSi and CoSi despite the fact both of them are not magnetic. In contrast, starting from MnSi, replacing Mn by Fe destroys rapidly the weak ferromagnetism. Some of the magnetic solutions of $\mathrm{Fe}_{1-x}\mathrm{Co}_x\mathrm{Si}$ were also studied in this thesis.

In these silicides, all the stoichiometric compounds and their solutions are bad metals at room temperature. When the temperature is decreased, however, the behaviour is diverse. The resistivity of MnSi decreases strongly and remains metallic down to the lowest temperature without showing superconductivity. Replacing Mn by Fe, although decreases T_C, only decreases the rate at which the resistivity decreases with temperature. Surprisingly, in a thin sleeve around FeSi (towards both MnSi and CoSi), the system shows an insulating ground state the origin of which is still matter of debate. Towards CoSi and beyond this insulating sleeve, the system remains metallic with a small decrease of the resistivity. The behaviour of the resistivity in magnetic fields is also different between the magnetic samples around MnSi and those in $Fe_{1-x}Co_xSi$. Around MnSi, the system shows negative magnetoresistance as usually expected for a metal at not so low temperatures. In the $Fe_{1-x}Co_xSi$ samples the opposite has been found and the detailed behaviour is even analogous to the quantum effects induced by disorder at extremely low temperatures.

Weak ferromagnetism is usually explained in an itinerant picture which was briefly described in Chapter 1. Although it explains various properties of weak ferromagnets, it fails in others. Moreover, it does not provide an explanation of the different behaviours presented in the weak ferromagnets around MnSi and those in $Fe_{1-x}Co_xSi$. In this thesis (Chapter 3) we addressed several of these failures regarding the transport and optical properties of MnSi. We showed that the optical properties of MnSi at low temperatures can be described by a phenomenological formula that contains the Drude description as a particular case. The implication is that the temperature dependence of the scattering rate (extracted from the DC resistivity) and its frequency dependence (extracted from the optical conductivity) do not follow the same dependence. This has enormous implications since temperature and frequency are only different manifestations of energy.

In Chapter 4 of this thesis FeSi, CoSi and various of its solid solutions were studied. It was shown that the formation of the insulating state in FeSi is not conventional in the sense that it is not fully explained by band theory. Two observations were determinant for this conclusion. First, the gap of the insulating state is filled at temperatures much lower than would be permitted by thermal excitations only. Second, it was demonstrated that the optical spectral weight contained in the optical conductivity (i.e. the integrated area below it) is not recovered in an energy range much larger than the insulating gap. This lack of recovery points to the necessity of taking into account strong correlations to describe the insulating phase of FeSi. Moreover, strong correlations would explain the magnetotransport properties of $Fe_{1-x}Co_xSi$. At relatively high temperatures, these properties are similar to the ones shown by strongly disordered metals at sub-kelvin temperatures.

Local Moments and Itinerant Electrons: Heavy Fermion Systems

Several systems show clearly two *kinds* of electrons. On one hand there are itinerant electrons that are responsible for the transport properties. On the other hand there are electrons that are localized and are responsible of the magnetic properties. When these electrons interact it gives rise to a rich behaviour. One of such systems is composed by the so called heavy fermion materials. This name originate from the fact that their properties are similar to those of the normal metals, though with much larger proportional constants. Since in the usual theory of metals these constants are proportional to the electron mass, the enhanced properties of heavy fermion systems can be interpreted as a renormalized mass of the electrons due to strong interactions.

Chapter 5 of this thesis studies a particular family of heavy fermion systems: $CeMIn_5$ (M = Co, Rh, Ir). This system has recently attracted a considerable attention due to the variety shown in its phase diagram. As the temperature is decreased, heavy fermion behaviour appears and precedes states like antiferromagnetism in $CeRhIn_5$ (T_N =3.8 K) and unconventional superconductivity in $CeCoIn_5$ (T_c = 2.4 K) and $CeIrIn_5$ (T_c = 0.8 K). It has also been suggested that the superconductivity in these materials is similar to the high T_c superconductors. The analogy even starts in the crystal structure that can be seen as layers of $CeIn_3$ (a well known heavy fermion system) separated by MIn_2 layers.

The work presented in this thesis has concentrated on the optical properties of the heavy fermion state. It has been shown that, at low temperatures, the optical responses of $CeCoIn_5$ and $CeIrIn_5$ are characterized by a narrow Drude peak representing the oscillations of the coherent electrons. This peak is formed below a certain characteristic energy known as hybridization gap. On the other hand, antiferromagnetism competes against the formation of the coherent state. This is shown in $CeRhIn_5$ where the narrow Drude peak does not evolve completely. Moreover, from the study of its dielectric function it was shown that the hybridization gap is smaller than the other two compounds.

Local Moments and Itinerant Electrons: Manganites

Finally, materials corresponding to the family of perovskite manganites were studied. Perovskite manganites are well known for having a phase diagram with multifarious phases. An example of this is the $La_{1-x}Ca_xMnO_3$ system. At low temperatures the phase is canted antiferromagnetic in $LaMnO_3$ and $CaMnO_3$ but between them various phases are found: ferromagnetic insulating and metallic, charge ordering, and antiferromagnetism. In general terms, this rich behaviour is the result of the interaction between localized moments and itinerant electrons in the manganese site. At least in the ferromagnetic metallic, this is well described by the double exchange Hamiltonian. However, other ideas and mechanisms have to be considered for a complete description of the manganites. One of them is strong electron-phonon interactions as is revealed in several forms, for example, the large isotope effect. Another mechanism that has to be considered is the natural tendency of the double exchange Hamiltonian to produce phase separation.

The final Chapter of this thesis describes the optical response of thin films of $(La_{0.5}Pr_{0.5})_{0.7}Ca_{0.3}MnO_3$ grown in $SrTiO_3$ substrates. Samples containing different oxygen isotopes, ^{16}O and ^{18}O, were studied. At room temperature, both kind of films show identical DC resistivity with no long range magnetic order. When the temperature is lowered, the resistivity increases until a certain temperature, T_C, from which it decreases again. This critical temperature is also accompanied by magnetic ordering. Samples with both isotopes show the same qualitative behaviour just described. However, samples containing ^{18}O show a lower T_C and the resistivity well below T_C is one order of magnitude larger than its counterpart. Another difference is evident when the temperature is raised above T_C. Samples with ^{18}O show a large hysteresis while in samples with ^{16}O, it is small. It has been argued that this is a manifestation of phase separation.

As in the DC resistivity measurements, the optical responses of both films are identical at room temperature but greatly differ at low temperatures and especially at low frequencies. At high frequencies (above 2.5 eV), the optical conductivity of both films is dominated by transitions corresponding to charge transfer excitations that are weakly temperature dependent. At low frequencies, above their corresponding T_C's, the optical conductivity of both films is dominated by a strong mid-infrared peak at around 1.5 eV (peak 3). This peak is favored in the paramagnetic state as it corresponds to intersite transitions $e_g^1(\mathrm{Mn}^{+3}) \rightarrow e_g(\mathrm{Mn}^{+4})$ where the transferred electron ends up being antiparallel to the localized electrons in the t_{2g} level. The intensity of peak 3 remains more or less constant above T_C but decreases rapidly below it. However, it does not disappear completely at low temperatures, particularly in the film containing ^{18}O where remains rather large. Another peak, labeled 2, can be identified at even lower frequencies (0.75 eV). This peak was identified also as an intersite transition of the same types as peak 3 with the difference that the transferred electron is parallel to the t_{2g} core. In this way, it is enhanced in the ferromagnetic state. Peak 2 is barely visible at high temperatures but increases its intensity below T_C and saturates before the lowest temperatures are reached. In fact, the temperature dependencies of peaks 2 and 3 are completely symmetric. Another point that has been noticed is that in the more metallic sample at low temperatures (^{16}O), peak 2 is accompanied by a narrow Drude peak containing few spectral weight.

In Chapter 6, it was argued that the temperature dependence just described can be encompassed in the phase-separation picture. Below T_C both ferromagnetic and antiferromagnetic phases are present. This is the reason for which peak 3 does not completely disappear in the ferromagnetic state. Moreover, isotope substitution changes the relative volume of one phase in respect to the other. This also explains the fact that in the less metallic sample, peak 3 is more intense at low temperatures.

Spectral Weight

A central problem in this thesis was the determination of the region in which the spectral weight contained in the optical conductivity was recovered. It was found that the region where this happens depends on the character of the electrons involved in low frequency processes. In the silicides and manganites, this happens in a fairly large region as the electrons involved have d character. In the heavy fermion systems studied here, the region was found to be much smaller since the electrons involving the formation of the coherent state are of f character.

Resumen

Esta tesis describe la utilización de espectroscopía óptica para estudiar las propiedades físicas de varios sistemas de electrones fuertemente correlacionados. En general, la espectroscopía óptica es una herramienta excelente para estudiar la estructura electrónica de cualquier material debido a que la conductividad óptica da información acerca de como los electrones se mueven en el material en respuesta a un campo electromagnetico externo. En particular, la conductividad óptica describe el movimiento de los electrones de un sitio atomico a otro. Este movimiento es determinado por dos procesos que compiten entre si: correlación entre electrones (que tienden a localizarlos) e hibridizatión de la función de onda (que tiende a delocalizarlos). Esta competición es precisamente la escencia de las correlaciones fuertes entre electrones.

Magnetismo Itinerante: Silícidos

El primer sistema descrito en esta tesis contiene un metal de transición y silicio. Específicamente se han estudiado los silícidos que contienen manganeso, hierro y cobalto. Aunqe estos metales muestran magnetismo en su forma elemental, los correspeondientes silícidos no son magnético a temperatura ambiente. De hecho, a bajas temperaturas, el único que es magnético es MnSi ($T_C = 30$ K). A temperaturas mayores a T_C, MnSi sigue la ley de Curie-Weiss con una magnetización mucho mayor que la magnetización de saturación en la fase magnética. Esto define MnSi como un material ferromagnético débil. Ferromagnetismo débil también aparece en una region relativamente grande de las soluciones sólidas entre FeSi y CoSi a pesar de que ellos no son magnéticos. En contraste, empezando desde MnSi, si se reemplaza Mn con Fe, se destruye rápidamente el ferromagnetismo débil. Algunas de las soluciones magnéticas de la familia $Fe_{1-x}Co_xSi$ también se estudiaron en esta tesis.

En estos silícidos, todos los compuestos estoquiométricos y sus soluciones son malos metales a temperatura ambiente. Si la temperatura se baja, sin embargo, sus comportamientos son diversos. La resistividad en MnSi decrece fuertemente y permanece metálico hasta la temperatura maás baja sin mostrar superconductividad. Al reemplazar Mn con Fe, aunque el magnetismo desaparece rápidamente, el material continúa siendo metálico hasta muy cerca de FeSi. Sorprendentemente, en una region muy pequeña alrededor de FeSi (en ambas direcciones, hacia MnSi y CoSi), el sistema muestra un estado fundamental que es aislante. El origen de este estado aislante es todavía materia de debate. En la direccion de CoSi y mas allá de la región aislante, el sistema permanece metálico con poca variación con temperatura. El comportamiento de la resistencia en campos magneticos es también diferente entre las muestras magneticas alrededor de MnSi y aquellas en $Fe_{1-x}Co_xSi$. Alrededor de MnSi, el sistema muestra una magnetoresistencia negativa tal como se espera para metales a temperaturas no tan bajas. En las muestras de $Fe_{1-x}Co_xSi$ se ha encontrado lo opuesto y el comportamiento detallado (a temperaturas relativamente altas de alrededor de 100 K) es incluso análogo a los efectos cuánticos introducidos por desorden y que se ven solamente a temperaturas extremadamente bajas.

El ferromagnetismo débil es usualmente explicado en un modelo itinerante que fue brevemente bosquejado en el Capítulo 1. Aunque este modelo explica varias propiedades de los materiales ferromagnéticos débiles, falla en otros. Además, no provee una explicación de los diferentes comportamientos observados en los materiales magneticos débiles alrededor de MnSi y aquellos en $Fe_{1-x}Co_xSi$. En esta tesis, (Capítulo 3) hemos estudiado varias de estas fallas con respecto a las propiedades ópticas y de transporte. Hemos demostrado que las propiedades ópticas de MnSi, a bajas temperaturas, pueden ser descritas por una fórmula fenomenológica que contiene la conocida formulación de Drude como un caso particular. La implicación es que la dependencia con temperatura de la tasa de dispersión (extraída de la resistividad DC) y su dependencia con frequencia (extraída de la conductividad óptica) no siguen la misma dependencia. Esto tiene importantes consecuencias ya que temperatura y frequencia son solo diferentes manifestaciones de energía.

En el Capítulo 4 de esta tesis se estudiaron FeSi, CoSi, y varias soluciones entre ellos. Se demostró que la formación del estado aislante en FeSi es no convencional en el sentido de que no es completamente explicada por la teoría de bandas. Dos observaciones fueron determinantes para esta conclusión. Primero, la gap del estado aisalnte se llena a temperaturas mucho mas bajas que las permitidas por solo excitaciones termales. Segundo, se demostró que el peso espectral contenido en la conductividad óptica (es decir el área integrada debajo de ella) se recupera tan solo en un rango de energía mucho mayor que el la gap. Esta falta de recuperación indica la necesidad de tomar en cuenta las correlaciones fuertes entre electrones para describir la fase aislante de FeSi. De hecho, se ha propuesto que el efecto Kondo es el que determina la formación del estado aislante. En este efecto, los electrones de conducción forman una nube alrededor de los momentos magneticos *eliminando* el magnetismo en este material. Ademas si la compensacion entre electrones de conducción y momentos magnéticos es exacta, el material se vuelve aislante. Otro aspecto que las correlaciones fuertes podrían explicar son las propiedades de magnetotransporte vistas en $Fe_{1-x}Co_xSi$. A temperaturas relativamente altas, estos materiales tienen propiedades similares a las que muestran metales fuertemente desordenados a temperaturas de alrededor de 1 K o menores.

Momentos Magneticos Locales y Electrones Itinerantes: Sistemas de Fermiones Pesados

Varios sistemas muestran claramente dos *clases* de electrones. Por un lado están los electrones itinerantes que son responsables por las propiedades de transporte. Por el otro, están los electrones localizados que son responsables de las propiedades magnéticas. Cuando estos electrones interactúan originan un comportamiento rico y variado. Uno de tales sistemas esta compuesto por los así llamados compuestos de electrones pesados. Este nombre se origina en el hecho de que sus propiedades son similares son similares a aquellas de los metales normales, aunque con constantes de proporcionalidad mucho mayores. Ya que la usual teoría de los metales estas constantes son proporcionales a la masa del electrón, las propiedades de los sistemas de electrones pesados pueden ser interpretadas como una masa del electrón renormalizada originada de las interacciones fuertes.

El Capítulo 5 de esta tesis describe una familia de lectrones pesados específica: $\mathrm{CeMIn_5}$(M = Co, Rh, Ir). Esta familia recientemente ha atraído mucha atención debido a la variedad mostrada por su diagrama de fase. A medida de que la temperatura se disminuye, aparecen propiedades de fermiones pesados y preceden estados como antiferromagnetismo en $\mathrm{CeRhIn_5}$ (T_N =3.8 K) y superconductividad no-convencional en $\mathrm{CeCoIn_5}$ (T_c = 2.4 K) y $\mathrm{CeIrIn_5}$ (T_c = 0.8 K). Además se ha sugerido que la superconductividad en estos en estos materiales es similar a la mostrada por los superconductores de alta temperatura crítica. La analogía incluso empieza con la estructura cristalina que puede ser vista como capas de $\mathrm{CeIn_3}$ (un muy conocido sistema de electrones fuertemente correlacionados) separatedas por capas de $\mathrm{MIn_2}$.

El trabajo presentado en esta tesis se ha concentrado en las propiedades ópticas de la region que muestra propiedades de fermiones pesados. Se demostró que, a bajas temperaturas, las respuesta óptica de $\mathrm{CeCoIn_5}$ and $\mathrm{CeIrIn_5}$ están caracterizadas por un pico Drude muy angosto que representa las oscilaciones de los electrones coherentes. Este pico se forma por debajo de una cierta energía característica conocida como gap de hibridización. Por otro lado, el antiferromagnetismo compite en contra de la formación de un estado coherente. Esto se demostró en $\mathrm{CeRhIn_5}$ donde el angosto pico Drude no evoluciona completamente. Además, del estudio de su función dieléctrica, se demostró que la gap de hibridización es mas pequeña que los otros dos compuestos.

Momentos Magneticos Locales y Electrones Itinerantes: Manganitas

Finalmente se estudiaron materiales correspondientes a la familia de las manganitas perovskitas. Las manganitas perovskitas son muy conocidas por presentar un diagrama de fase con fases muy variadas. Un ejemplo es el el sistema $La_{1-x}Ca_xMnO_3$. A bajas temperaturas $LaMnO_3$ y $CaMnO_3$ muestran antiferromagnetismo donde los momentos están inclinados unos respecto al otro. Entre estos extremos se encuentran varias fases como ferromagnetismo metálico y aislante, ordenación de cargas y antiferromagnetismo usual. En términos generales, esta rica gama de propiedades es el resultado de la interacción entre los momentos localizados y los electrones itinerantes ubicados en el manganeso y que se describe por el Hamiltoniano de doble intercambio. Sin embargo, otras ideas y mecanismos tienen que ser considerados para una completa descripción de las manganitas. Uno de ellos es la fuerte interacción electrón-fonón como se revela en varias formas, por ejemplo, el gran efecto isotópico. Otro mecanismo que tiene que ser considerado es la tendencia natural del Hamiltoniano de doble intercambio a producir separación de fases.

El Capítulo final de esta tesis describe la respuesta óptica de laminas delgadas de $(La_{0.5}Pr_{0.5})_{0.7}Ca_{0.3}MnO_3$ depositadas en substratos de $SrTiO_3$. Se estudiaron muestras que contienen diferentes isótopos de oxígeno, ^{16}O y ^{18}O. A temperatura ambiente ambos tipos de láminas muestran idéntica resistividad DC sin ordenamiento magnético. Cuando la temperatura decrece la resistividad aumenta hasta cierta temperatura, T_C, a partir de la cual disminuye. Esta temperatura crítica también va acompañada de ordenamiento magnético. Las muestras con ambos isótopos muestran cualitativamente este mismo comportamiento. Sin embargo, las muestras que contienen ^{18}O muestran una menor T_C y la resistividad muy por debajo de T_C es un orden de magnitud mayor a su contraparte. Otra diferencia es evidente si la temperatura aumenta (empezando debajo de T_C). Muestras con ^{18}O muestras una histéresis pronunciada mientras en que aquellas con ^{16}O el efecto es pequeño. Se ha conjeturado que esta es una manifestación de separación de fases.

Tal como ocurre en las mediciones de resistividad DC, la respuesta óptica de ambas películas es idéntica a temperatura ambiente per difiere mucho a bajas temperaturas y especialmente a bajas frequencias. A frequencias altas (sobre los 2.5 eV), la conductividad óptica esta dominada por transitiones fuertes que corresponden a excitaciones de transferencia de carga y que dependen débilmente de la temperatura. A bajas frequencias, por encima de sus correspondientes T_C's, la conductividad óptica esta dominada por un fuerte pico a alrededor 1.5 eV (de aqui en adelante llamado pico 3). Este pico es favorecido en el estado paramagnético ya que corresponde a transiciones entre diferente sitios atomicos del tipo $e_g^1(\mathrm{Mn}^{+3}) \rightarrow e_g(\mathrm{Mn}^{+4})$ donde el electrón transferido termina siendo antiparalelo a los electrones localizados que se hallan en nivel t_{2g}. La intensidad del pico 3 permanece relativamente constante sobre T_C pero decrece rápidamente a temperaturas menores. Sin embargo, no desaparece completamente a bajas temperaturas, especialmente en el film que contiene ^{18}O. Otro pico, indicado con el número 2, puede reconocerse a frecuencias algo mas bajas (0.75 eV). Este pico fue identificado igualmente como una transición entre sitios con la diferencia de que el electrón transferido termina siendo paralelo al núcleo t_{2g}. De esta manera, es favorecido en el estado ferromagnético. El pico 2 es escasamente visible a altas temperaturas pero su intensidad aumenta debajo de T_C y se satura antes de alcanzar las temperaturas mas bajas. De hecho, los picos 2 y 3 sus dependencias con temperatura son completamente simétricas. Otro punto a notar es que en la muestra mas metálica a bajas temperaturas (^{16}O), el pico 2 esta acompañado de un pico Drude que contiene poco peso espectral.

En el Capítulo 6, se arguyó que la dependencia con temperatura que hemos descrito puede explicarse por medio de la separación de fases. Por debajo de T_C las fases ferromagnéticas y antiferromagnéticas están presentes. Esta es la razón por la cual el pico 3 no desaparece completamente en el estado ferromagnético. Además la substitución isotópica cambia el volumen relativo de una fase con respecto a la otra. Esto también explica el hecho de que en la muestra menos metálica, el pico 3 es mas intenso a bajas temperaturas.

Peso Spectral

Un problema central discutido en esta tesis fue la determinación de la región donde el peso espectral contenido en la conductividad óptica se recupera. Se encontró que la región donde esto pasa depende del carácter de los electrones involucrados en los procesos a bajas frecuencias. En los silícidos y manganitas, esto ocurre en una region relativamente amplia ya que los electrones involucrados tienen carácter d. En los sistemas de fermiones pesados estudiados aquí, la region es mucho menor ya que los electrones que forman el estado coherente son de carácter f.

Publications

Articles

- *Oxygen isotope effect in the optical conductivity of* $(La_{0.5}Pr_{0.5})_{0.7}Ca_{0.3}MnO_3$ *thin films.*
  F. P. Mena, A. B. Kuzmenko, A. Hadipour, D. van der Marel, and N. A. Babushkina. Submitted to Physical Review B.

- *Optical conductivity of* $CeMIn_5$ *(M = Co, Rh, Ir).*
  F. P. Mena, D. van der Marel, and J. L. Sarrao. Submitted to Physical Review Letters.

- *Ferromagnetism makes a doped semiconductor less shiny.*
  F. P. Mena, J. F. DiTusa, D. van der Marel, G. Aeppli, D. P. Young, C. Presura, A. Damascelli, and J. A. Mydosh. Submitted to Nature.

- *Optical Spectral Weight in Pure and Cobalt-Doped FeSi.*
  F. P. Mena, D. van der Marel, C. Presura, A. Damascelli, G. Aeppli, J. DiTusa, D. P. Young, A. Lichtenstein, A. Poteryaev, M. Dressel, A. A. Menovsky, and J. A. Mydosh. In preparation.

- *Structural, electronic, and magneto-optical properties of* YVO_3.
  A. A. Tsvetkov, F. P. Mena, P. H. M. van Loosdrecht, D. van der Marel, Y. Ren, A. A. Nugroho, A. A. Menovsky, I. S. Elfimov, and G. A. Sawatzky. Physical Review B **69**, 075110 (2004).

- *Heavy carriers and non-Drude optical conductivity in MnSi.*
  F. P. Mena, D. van der Marel, A. Damascelli, M. Fäth, A. A. Menovsky, and J. A. Mydosh. Physical Review B **67**, 241101R (2003).

- *Manifestation of multiband optical properties of* MgB_2.
  A. B. Kuzmenko, F. P. Mena, H. J. A. Molegraaf, D. van der Marel, B. Gorshunov, M. Dressel, I. I. Mazin, J. Kortus, O. V. Dolgov, T. Muranaka, and J. Akimitsu. Solid State Communications **121**, 479 (2002).

Conference Proceedings

- *Redistribution of the c-axis spectral weight and conductivity sum rules in LSCO as revealed by optical transmission.*
  A. B. Kuzmenko, N. Tombros, F. P. Mena, A. Hadipour, H. J. A. Molegraaf, D. van der Marel, M. Grüninger, and S. Uchida. Physica C: Superconductivity, In Press (2004).

- *Heavy carriers, non-drude optical conductivity and transfer of spectral weight in MnSi.*
  F. P. Mena, A. Damascelli, D. van der Marel, M. Fath, A. A. Menovsky, and J. A. Mydosh. Journal of Magnetism and Magnetic Materials **272-276**, E53 (2004).

- *Optical and magneto-optical study of orbital and spin ordering transitions in YVO_3.*
  A. A. Tsvetkov, F. P. Mena, Y. Ren, I. S. Elfimov, P. H. M. van Loosdrecht, D. van der Marel, A. A. Nugroho, A. A. Menovsky, and G. A. Sawatzky. Physica B: Condensed Matter **312-313**, 783 (2002).

Acknowledgements

Completing a doctorate requires, among other things, interaction with many different people. This interaction have originated good and bad experiences which, nevertheless, have been enriching in one way or the other. This is the reason for which, at this point of my thesis, I would like to thank all the people who I have met and have enriched my experience of working and living in the Netherlands. With this I could finish but there is a number of people who I want to expressly mention. The first one is, of course, Dirk. And I use *”of course”* not only because you were my promotor but because you have definitely been a really good mentor and friend. Well, everything started during my master studies and later when you gave me the opportunity to join your group. I really appreciate your efforts to overcome, as you put it in an email, the *”age hurdles”* imposed by FOM. As a mentor I will always remember our discussions about preparing experiments and the long ones discussing results trying to explain them. Sometimes we got it wrong, some times we got it fine but always concentrating in the basic principles. I really enjoyed this way of doing physics. As a friend it will be imposible to forget your sailing lessons in the Hornsemeer or the skiing ones in the Salève or your efforts to convince me of staying in the Academia.

Then, I also want to thank my second promotor, Paul. I appreciate that you *adopted* me in your newly formed group for about one year. Your comments, specially in preparing this thesis, have been really fruitful.

Although it has been wonderful to have two great promotors, the more daily and terrenal matters are spent with the other members of the group. It is just matter of available time. I would like, then to thank all of them, in special Alexey, Hajo, Christian, and Fabrizio since for quite a long time we were the only oficial scientific members of the group. I and Alexey started at around the same time, Alexey with his postdoc and I with the PhD. I really think this was a strike of luck, Alexey, since in this way we were able to work a lot together and in that process I learned a lot from you. And we shared even more, we married with our respective wives at around the same time, lived under the same roof (as we say in Ecuador) for a couple of months, looked for a house, and so many other things. I am also thankful for your hospitality during my visits to Switzerland, which reminds me to thank also Elena. You both were really nice hosts. Finally, Alexey, I only hope that, as we agreed in Ameland, you visit Ecuador one of this

years.

Hajo, you have also been a wonderful colleague and friend. One of the things I will never forget is your willingness to help. I think that it often was at expenses of your own time. No matter how busy you were, you were always helping someone. I wonder if that is one of the reasons for which you had to extent your contract... If so, sorry for that. Cristian, it was also great to work with you. Especially as you showed me almost everything I know of ellipsometry. As a friend I also enjoyed your company and talking to you, although you have to forgive me as, until now, I have not followed your advice of going to the U.S. and having a child. Fabrizio, you joined the group a bit latter. However, we have worked also with what has converted in our *"precious"* MnSi. It has been a nice experience to find the true *italian way.*

Since Dirk moved to Genève, the group grew considerably. Despite of my few visits I got to know a bit the other members of the group. Thanks Ricardo, Violetta, and Erik for your amiability. Especially Erik for helping me with the preparation of the Samenvatting. The last person from Dirk's group who I want to thank is Cor. The last but not the least as it is said. You know, in an experimental group, without technical help working becomes impossible. In fact, Cor, your help has been invaluable, especially with all those smart gadgets you have built during the years.

I also want to thank all the members of Paul's group, Katarizna, Artem, Silviu, Daniele, Dima, Sagar, Renate, and Arjen. In particular Arjen, thanks for your help in setting up the MOKE experiment. And, of course, the students that at some point or the other joined the group: Afshin, Puri, Cosmina. It has been a pleasure to meet all of you.

Outside my working environment I have also met a lot of people inside and outside the university. In the first place I want mention the *volleyball people.* It started almost two years ago when Alexey suggested playing volleyball. It is incredible but we have played almost non-stop every weekend since then. I only hope we can continue playing for a while. And there is also the Latin-American community (which, by the way also includes the *Yugoslavian* girls, Diana, Branislava and Sonja). It is always nice having people around speaking *almost* the same language. *¡Vamos muchachos, hasta la victoria siempre!* From this fairly large community (I mean, taking into account that we are in Holland and moreover in Groningen) I want to express my gratitude to one of the persons of whom it can really be said that is a citizen of the world, Andrés. You have not only become one more of Paul's group but also a good pal. I appreciate that you have showed me that there is a whole world beyond Grolsch and Heineken.

This is the point to go to a different *level.* My parents and siblings who I have not seen for already four years. You know, this is my thesis and since my English is not that good, I would prefer to turn the *Language knob* to Spanish... *Ya se lo que iban a decir, "¿a que hora este guambrito se cansa de escribir en inglés y pone algo en español?" Bueno, pues, este es el momento porque quiero enviarles un abrazo gigantesco desde aquí. Aunque no me han acompañado físicamente* *durante todo este tiempo, sé que lo han hecho de otras maneras. Los quiero a todos. Y bueno, papi y mami, este es el resultado de haberme ayudado con los estudios y haberme incentivado a seguir siempre adelante.*

The final paragraph is reserved for someone extremely especial. Someone who has been with me these four years. Someone who also left Ecuador for the *unknown.* Not knowing the Language and not having been abroad before, it was a big step. And, then, being here, waiting at home until I finish the experiments. Being always extremely patient. Being always with me. *Gracias corazón, gracias por estar conmigo.*